4D electrical resistivity monitoring of cyclic aquifer thermal energy storage

Auteur : Sanasi, Ludovico Ivan
Promoteur(s) : Nguyen, Frederic
Faculté : Faculté des Sciences appliquées
Diplôme : Master en ingénieur civil des mines et géologue, à finalité spécialisée en géologie de l'ingénieur et de l'environnement
Année académique : 2016-2017
URI/URL : http://hdl.handle.net/2268.2/3172

Université de Liège

Faculté des Sciences

Appliquées

Département ArGEnCo

4D electrical resistivity monitoring of cyclic aquifer thermal energy storage

SANASI Ludovico Ivan

Graduation Studies conducted for obtaining the Master's degree in

Ingénieur Civil des Mines et Géologue

Supervisor

NGUYEN Frédéric

Academic year 2016-2017

Acknowledgments

Above all, I would like to thank the jury for the time spent to read my elaborate and to evaluate my defence.

Then, I also would like who helped me by answering to my doubts and giving me suggestions on the interpretation of the results. I thank Nolwenn Lesparre, who helped me many times with information, data, and whatever. I hope that all my thanks will be enough to express my gratitude to you. I thank my supervisor, Prof. Nguyen who has been helpful and very patience to all my questions. I also thank Thomas Hermans who helped me to solve some unexpected problems.

I would like to thank also all the staff of AQUALE, the company who hosted me during my internship. In particular, I thank Tanguy Robert who gave me "private" applied geophysical lessons. I thank the Italian guys, Marco Riboni and Pietro Vizzotto, who treated me as if I was their colleague/little brother.

I would express also my gratitude to those persons that I met in this Belgian experience. I thank my Belgian engineering colleagues. I thank my friends who enjoyed with me many Belgian beers.

I would like to give a special "thank you!!!" to Laura. In this year in Liège we have been through so many contrasting emotions, that I do not even know where I should start.

I am also very grateful to the Alma Mater, the University of Bologna which gave me many opportunities to learn, grow and become. Moreover, I thank Prof. Gandolfi who always helped me and Laura to solve exactly all our difficulties and doubts. I thank of course all those friends and colleagues that I met in Bologna and along with I spent my best days with laughs and study.

Then, I would infinitely thank all those persons who always believed in me. Therefore, I thank my oldest friends from Erchie and those I met in High School, during my green years. I thank all my family, in particular my brother, my mother and my father who believed, helped and sustained me in every aspect. I would of course say thank you to my grandparents, especially to my grandfather, the one "who is good in math".

Last but not least, I want to thank my girlfriend, Eleonora. She believed in me, she waited for me, she loved me, she came, supported me and lived me. Now I can finally say "I am coming Lélé".

Abstract

The worldwide society needs more than ever to invest in new environmental friendly technologies to ensure the three E's (Environmental protection, Environmental growth and Energy security). To tackle this problem, a technology as the Aquifer Thermal Energy Storage (ATES) might be employed. Beside the design phase, ATES systems need to be monitored to ensure the efficiency of the ongoing thermal process. Therefore, in the present Master Thesis the 4D Electrical Resistivity Tomography (ERT) is studied to assess its monitoring ability in ATES systems. In order to achieve this aim, a cyclic heat storage experiment has been performed and monitored by an ERT grid of 6 parallel profiles 60 m long, spaced each other by 3 m. The cyclic experiment was conducted in a site located in Hermalle-sous-Argenteau, in Belgium. It consisted in alternating 4 phases (one per day) of injections and withdrawals. During these phases, the water was injected (at 40°C) or pumped for 5 h with a flow rate of 3 m^3/h. The obtained 2D time-lapse inverted models have been also converted in temperature values to better appreciate the thermal variations. Globally, the interpretation of both resistivity and temperature 2D time-lapse models led to successfully monitor the plume across the time and the space. Such results have been also compared with direct measurements made in 5 piezometers in the vicinity of the well, obtaining good agreement. Although 3D time-lapse inversions did not show perfect results, they contributed partially to monitor the plume. Finally, asymmetric results from 3D and 2D time-lapse models contributed to spot heterogeneities in the studied site. To conclude, this elaborated has demonstrated the potentials of the 4D ERT as monitoring tool in ATES systems, broadening the future perspectives of this topic.

Keywords: 4D ERT; ATES; Temperature monitoring; Time-Lapse; Electrical Resistivity Tomography; Shallow geothermal system; Heat storage; Alluvial aquifer

Contents

List of Figures

List of Figures in Annex

1 Introduction

Aquifer thermal energy storage (ATES) is nowadays a common technique used to tackle and reduce the energy consumption. Apart from the design itself, such systems need to be monitored and in recent studies, Electrical Resistivity Tomography (ERT) has started to gain importance for its flexibility and simplicity.

The present Master Thesis is an elaborated which mainly aims to demonstrate and study the ability of the ERT to monitor aquifer thermal energy storage systems. To do so, a cyclic heat storage experiment has been performed, simulating a cycle of an aquifer thermal energy storage system. In particular, the experiment has been carried out using a heterogeneous site located in an alluvial aquifer in the vicinity of Hermalle-sous-Argenteau (Liège province, Belgium). The site has been chosen mainly since it fits the typical hydrogeological characteristics needed for an ATES system. Instead, the experiment consisted in performing two injections of hot water and two withdrawals alternatively in four days, i.e. one phase per day. During the cycle experiment, six ERT profiles monitored the whole process along with eight CTD (Conductivity Temperature Depth) probes placed in five piezometers.

Besides the main objective, three specific goals have been fixed in this Thesis. First, the ability of ERT to spot temperature variations. In other words, the goodness of an almost long-term monitoring ERT survey. This will be mainly verified comparing ERT results with direct measurements taken with CTD probes.

Then, focusing on the ERT monitoring results, the second objective is to understand how the injections and withdrawals are going to influence the temperature distribution of the subsurface across the time and the space. The 4D ERT has to monitor accurately the stressed subsurface and be able to define the heat water plume in all the phases.

Finally, the third objective is specifically related to the characteristic of the site. As a matter of fact, it questions how the heterogeneities are going to influence the aquifer heat storage.

In order to answer to these objectives, the present Thesis has been accurately structured. The first Chapter will give an overview on the ATES systems and then it will describe the potential of ERT to monitor such systems. Chapter 2 has been written with the aim to give a brief and essential theoretical introduction on the geophysical relations behind the ERT, the ERT survey itself and finally the ERT inverse problem.

Once described some introductive aspects, Chapter 3 focuses on the core of the Thesis. Indeed, the cycle experiment and the site itself will be fully described. Then some paragraphs will show the materials and methods used for answering to the imposed objectives.

Instead, Chapter 4 will treat the results obtained from the methods, showing and discussing them. In particular, the results will be divided in CTD results, 2D time-lapse resistivity models, 2D time-lapse temperature models and 3D resistivity time-lapse model.

Finally, the last Chapter will sum up the discussions previously done and give some future perspectives related to the studied topic.

1.1 Thermal Energy Storage

Nowadays, it is well-known that the most important environmental problem is the global warming. Many are the countries which are committed to tackle such issue. In addition to the global warming problem, there are other environmental problems which oblige to invest on alternative and renewable resources. Some of these problems are the non-renewable resources' depletion, environmental pollution and the ozone depletion. Therefore, the worldwide society needs more than ever to develop new environmental friendly technologies to ensure the three main objectives: Environmental protection, Environmental growth and Energy security (known as three E's) (Evliya 2007). An example of strategy which aim to tackle the mentioned environmental problems is the "Europe 2020" led by the European Commission ('Climate Action' 2015). The European strategy, indeed, to tackle the global warming, has implemented policies focused on climate-related topics such as energy efficiency, greenhouse gases, transport emissions, ozone layer, low carbon technologies, etc. ('Climate Action' 2015). Among such environmental problems, energy consumption is a major cause of the environmental degradation (Evliya 2007). Therefore, there is a need to reduce the energy consumption, hence the environmental damage and to move towards a more sustainable future. With this aim, technologies such as Thermal Energy Storage (TES) will play a key role in reducing the energy consumption.

Generally, Thermal Energy Storage can be classified in terms of storage duration in short-term (daily) storage and long-term (seasonal) storage (Xu, Wang, and Li 2014). Studies have already shown that generally seasonal storage systems are more advantageous than the daily ones, capable to satisfy the 50-70% of the annual heat demand rather than 10-20% of the daily heat demand (Fisch, Guigas, and Dalenbäck 1998). In particular, seasonal heat storage is useful not

only to for district heating network (Schmidt, Mangold, and Müller-Steinhagen, 2003), but also for greenhouses (Solar Thermal Energy Storage) (Alkilani et al. 2011).

The mechanisms implied in the thermal energy storage can be divided in three main groups (Xu, Wang, and Li 2014):

- Latent heat storage
- Chemical reaction and thermochemical heat storage
- Sensible heat storage

The Latent heat storage has higher energy density than sensible heat storage, and this characteristic is mainly due to the phase change material (PCM) which is normally used in such storage system. As a matter of fact, its duty is to absorb and release heat in the form of latent heat of fusion (Xu, Wang, and Li 2014).

The Chemical reaction and thermochemical storage systems have the highest energy density capacity, allowing just few heat losses. Indeed, a volume of 1 m^3 (70°C as temperature increase) stored with chemical reaction storage is equivalent to 34 m^3 stored in water (Hadorn 2008). Chemical reaction systems involve two chemical substances stored separately during the storage period, which are exploited to form reversible chemical reaction (Xu, Wang, and Li 2014). The thermochemical (sorption) process involve instead absorption and adsorption processes to store the heat (Xu, Wang, and Li 2014). Both chemical reaction and thermochemical heat storage methods are suitable for storing high grade heat, hence high operating temperatures (higher than 300°C and 50-70°C, respectively) (Xu, Wang, and Li 2014).

On the other hand, the Sensible heat storage method converts the available heat into sensible heat stored in selected materials. Once needed, the heat is then recovered from the storage medium (Xu, Wang, and Li 2014). The sensible storage method involves the use of storage mediums such as water tank storage and underground mediums (underground thermal energy storage, UTES) as aquifer and underground soil (Xu, Wang, and Li 2014). The main advantages of the sensible storage method are the low-cost investments, the simplicity and its relative high diffusion (Xu, Wang, and Li 2014).

1.1.1 UTES

As mentioned before, Underground Thermal Energy Storage (UTES) method involves the storage of heat by means a medium sited in the underground and can be exploited for both heating (during the winter season) and cooling (during the summer season). Such system can be classified in two main techniques: Borehole Thermal Energy Storage (BTES) and the Aquifer Thermal Energy Storage (ATES) (Andersson 2007).

The BTES is a system which consists of a series of borehole heat exchangers (vertical or horizontal) at a depth ranging between 50 m and 200 m (Andersson 2007). Such technology works in a closed system, where a fluid circulates and exchange heat within the heat exchangers (Thomas Hermans et al. 2014).

Instead, ATES systems involve groundwater as thermal carrier by means of an open system of water wells. In particular, the energy is therefore stored partly in the water itself and partly in the grains of the aquifer formation. Therefore, the constant injection of colder or warmer water will lead to form a temperature radial front around the well (Andersson 2007).

1.1.1.1 ATES

ATES systems work in a low temperature conditions, normally below 30°C. There are two general types of configuration for ATES systems. The first uses groundwater for preheating the air during the winter season and for precooling it during the summer (potential energy savings are between 90-95%, with a payback period of 0-2 years) (Andersson 2007). The second, instead, has the same function as the fist configuration, but it has also heat pumps to support the process, leading to have better results in terms of temperature increase than the previous configuration (potential energy savings are between 80-87%, with a payback period of 1-3 years) (Andersson 2007).

As mentioned before, ATES is a well settled technology and during the last years has confirmed its diffusion with many applications. In literature, it is quite easy to find articles on ATES applications. Many of them are related to European projects in countries such as Germany, Sweden, the Netherlands and Belgium (Xu, Wang, and Li 2014; Vanhoudt et al. 2011; Andersson 2007; Schmidt and Müller-Steinhagen, 2004). In Sweden there are many operating ATES systems (more than 30) (Andersson 2007). On the other hand, in the Netherlands ATES systems are even more diffused (200 plants in 2004), mostly in industrial applications (Andersson 2007).

In Rostrock, Germany, the first solar heating plant with seasonal storage has been designed and built. They have coupled the solar heating panel with ATES system of a 30 m deep aquifer (operating temperatures range between 10-50°C) (Schmidt and Müller-Steinhagen, 2004).

In Antwerp, Belgium, ATES system has been applied on a hospital heating and cooling system (Vanhoudt et al. 2011). The system consists of two water wells distant 100 m between each other. After few years of activity, the Belgian system reached outstanding results, such as 81% of the cooling energy needed and 22% of the heating energy needed came from the use of the groundwater. In addition to that, the energy savings reached a value around 71% (if compared to a standard cooling and heating system based on a gas-fired boiler and compression cooling machines) (Vanhoudt et al. 2011).

The design phase of ATES technologies is strongly dependant on the characteristics of the aquifer formation. As a matter of fact, the hydrogeological properties have a high influence on the efficiency of the ATES system. The most important hydrogeological parameters are: the hydraulic conductivity, effective porosity, specific storage and hydraulic gradient. These properties are responsible of the groundwater flow as well as the quantity of water that could be injected or withdrawn (Lee 2013). Concerning the thermal properties of the aquifer, there are two main physical mechanisms that impose the efficiency of the system, such as the convection and the conduction (Lee 2013). The conduction depends on two main thermal parameter of the aquifer formation. They are the heat capacity, which is the amount of temperature change linked to an absorption or loss of energy by the aquifer media, and the thermal conductivity, which is simply the ability of the aquifer media to transmit heat (Lee 2013). On the other hand, convection has two different governing mechanisms, thermal advection and thermal dispersion. The advection is due to the average linear flow of the groundwater through the aquifer media, while the thermal dispersion is the spreading mechanism of the thermal energy across the three spatial dimensions. Moreover, there is a further thermal mechanism, which is the free convection and is governed by the density variations caused by a temperature gradient. Despite that, in ATES systems the low operating temperatures limit such mechanism (Lee 2013). In addition to the previous mentioned thermal mechanisms, in aquifers there could be a further thermal mechanism due to the regional groundwater flow. As a matter of fact, high regional groundwater flows could lead to a down-gradient advection of stored energy, which obviously means a bad storage efficiency. Such effect might be also tackled considering a formation with a lower hydraulic conductivity (Lee 2013). The last characteristic of the aquifer formation is its chemistry. In this case, chemistry could easily lead to problems such as corrosion of the well, clogging of both aquifer and well,

and biofouling of the well zone. Although these problems can be mitigated with water treatment technologies or even avoided if considered before the design, the geochemistry of the formation still plays an important role in the ATES systems (Lee 2013).

Resuming, an aquifer suitable for an ATES system should have: good effective porosity and good hydraulic conductivity and specific storage to allow a good injection or pumping rate; relatively high porosity to minimise conductive energy losses and to increase the thermal store efficiency (since water has lower thermal conductivity than rock but higher heat capacity); and low hydraulic gradient to minimise the convective energy losses. Consequently, in order to obtain such parameters for the design phase, many investigations are needed. Classic hydrogeological in situ tests (e.g. pumping test, slug test) are normally carried out for obtaining hydraulic parameters, while different thermal-hydrogeological in situ tests (e.g. thermal tracer test, Thermal Response Test (Raymond et al. 2011)) are performed to obtain the previously described thermal storage parameters. Unfortunately, such tests give punctual information, without representing properly the eventual heterogeneities of the subsurface.

Beside the design phase which normally takes into account the aquifer properties previously described, there are other necessities for the correct functioning of the ATES system, namely the possible environmental impacts and the efficiency of the system. The former is mainly linked to the possible consequences that different temperatures of the aquifer might cause, the latter is related to the temperature plume and its development. As far as the environmental impacts, different temperatures might lead to have changes in the groundwater chemistry and microbiology. It has been studied that normally cooling temperatures (from 10-12°C to 6-8°C) provoke minor effects to the groundwater environment (Arning et al. 2006). On the other hand, heating temperatures above 25°C have shown that can impair the quality of the groundwater by possibly releasing heavy metals from the sediments (Jesußek, Grandel, and Dahmke 2013). With regard to the microbial effects, although higher temperatures might affect the aquifer microbial community enhancing their activity (Brielmann et al. 2011), no dangerous changes have been found in both the ecosystem and the drinking water quality (Brielmann et al. 2009).

Along with design phase, both performances and environmental impact problems of ATES systems need therefore to be monitored and controlled. Normally, to better understand and forecast the behaviour of the aquifer and to identify the possible temperature plumes, it is common practice to design a hydrogeological and numerical model. Although such practice can obtain good results, it is not a proper monitoring and is also based on punctual

information (i.e. boreholes, head level of piezometers network, results of thermal or hydrogeological tests) which may not take into account possible heterogeneities. Apart from the hydrogeological monitoring methods, there are some promising geophysical methods useful for the monitoring of ATES systems. As a matter of fact, Hermans et al. (2014) have described and reviewed three emerging geophysical monitoring methods: the Electrical Resistivity (ERT) method, the Self Potential (SP) method and the in situ fibre optic Distributed Temperature Sensor (DTS) method. In this Thesis, instead, the ERT method will be described and used in an in situ experiment for monitoring an ATES system.

1.2 ERT as a tool for monitoring

Electrical Resistivity Tomography (ERT) is an electrical geophysical method able to acquire bulk resistivity or conductivity measures in 2D, 3D or even 4D and map the subsurface distribution of such resistivity values. Furthermore, bulk resistivity (or conductivity) is affected by many subsurface variables, leading to make ERT flexible for many purposes. Indeed, bulk resistivity depends on hydrogeological parameters such as porosity, water content, salinity of the groundwater and temperature.

ERT is a diffuse electrical geophysical method which has been employed in many fields, going from the monitoring and the investigation of landslides (Perrone, Lapenna, and Piscitelli 2014), to the mineral exploration (Loke et al. 2013), to hydrogeological investigations, to the temperature variations. With regard to the temperature variations, in recent years ERT monitoring applications are clearly increasing although such technique is not widely used. Indeed, instead of representing punctual information as direct measurements normally do, ERT gives a spatial representation of the subsurface, making it a good hydrogeological monitoring tool. Some shallow geothermal related studies found in literature are therefore mentioned.

Hermans et al. (2015) studied an heat tracing experiment in a shallow aquifer with cross-borehole time-lapse ERT. The results have been converted in temperature values and compared with direct measurements, showing a good agreement. Therefore, the study suggests the use of ERT as a tool for monitoring heat tracing experiments as well as shallow geothermal systems.

Hermans et al. (2012) monitored temperature variations with a surface ERT acquisition of a heat water injection in a shallow sandy aquifer. In particular, the ERT results have been

converted into temperature values and compared with the thermo-hydrogeological model results. The comparison confirmed a good accordance between the two results and the whole study demonstrated how ERT is a powerful and efficient tool to monitor heat water injection in shallow aquifers.

Arato et al. (2015) monitored the thermal performances of a BTES system using 2D and 3D ERT acquisition. Good results confirmed how both 2D and 3D ERT surveys could be a useful tool to monitoring subsurface changes.

Giordano, Comina, and Mandrone (2016) used time-lapse ERT to monitor the thermal affected zone by means of a lab-scale experiment. The obtained results are then compared with direct measures results and heat propagation numerical simulation results, reaching an acceptable agreement between the three different results.

Giordano et al. (2017) monitored the thermal affected zone of a BTES system with time-lapse ERT. In particular, once inverted the ERT profiles, an estimation of subsurface temperatures has been performed, although such results were not perfectly in agreement with the direct measures. Finally, this study also suggests the use of the pseudo-sections alone for a rough monitoring, since the inversions performed did not significantly improve the qualitative and quantitative information of the results.

So far, as described before, some experiments have been carried out using ERT as monitoring tool of heat injections. Despite that, the experiments found in literature not only are quite recent, but they are simple and numerically scarce. Therefore, this Thesis tries to put a step ahead the recent developments by performing a 4D ERT monitoring, able to detect resistivity changes across a larger area caused by a series of injections and withdrawals.

In this Thesis, ERT will be used to monitor 2 cycles of a heat injection and pumping experiment in time-lapse mode. Both 2D and 3D results will show how ERT might be employed in monitoring shallow geothermal systems (i.e. ATES systems), confirming and enlarging its capabilities in such context.

2 Theory of Electrical Resistivity Tomography

In this chapter some theoretical topics will be shown and described. The aim is to give to the reader a brief introduction of the geophysical aspects that will be treated in this Thesis. Therefore, in order to introduce the ERT, there will be described first the basic petrophysical relations, then the ERT acquisition method and finally the inversion problem.

2.1 Introduction

Geophysical electrical methods are mainly used to obtain the resistivity (measured in Ohm·m) distribution of the subsurface by means of surface non-invasive measurements of electric potentials (some mV). Such measurements are normally carried out using electrodes on the surface (or along boreholes) and a controlled current injection (some mA). As mentioned before, the obtained resistivity values are used and linked for many kind of studies. This section will mainly focus on the relations between bulk electrical resistivity and some interesting geological parameters.

First of all, the fundamental physical relation which governs the current flow in a medium is the Ohm's Law:

$$\vec{J} = \sigma \vec{E} \tag{2.1}$$

Where **E** is the electric field intensity [V/m], $\boldsymbol{\sigma}$ is the electric conductivity [S/m] (the conductivity is also the reciprocal of the resistivity ρ [Ohm·m]) and **J** is the current density [A/m^2]. Then, the electric field is defined as the inverse gradient of the electric potential (ϕ):

$$\vec{E} = -\nabla \phi \tag{2.2}$$

After few passages and simplifications, the electrical Poisson equation is derived:

$$\nabla \cdot \vec{J} = -\nabla \cdot (\sigma \nabla \phi) \tag{2.3}$$

Such equation (2.3) is indeed the equation that shows the potential distribution in a medium due to a punctual current source. In a homogeneous medium with a single current source, the solution of equation (2.3) is straightforward and could be solved analytically. Therefore, the potential $\boldsymbol{\phi}$ [V] could be expressed as follows:

$$\phi = \frac{\rho I}{2\pi r} \tag{2.4}$$

Where r is the radius [m] from the current source to a point, while I is the injected current [A]. However, in practical cases all electrical surveys need 4 electrodes (actually from 2 to 4, depending on the electric array) for a single measurement. Two electrodes, one positive and the other negative, are used for injecting the current I into the ground, while the other two electrodes are used to measure the resulting voltage difference. In particular, since all surveys measure the electric potential difference, such potential difference can be expressed as:

$$\Delta\phi = \frac{\rho I}{2\pi}\left(\frac{1}{r_{C1P1}} - \frac{1}{r_{C2P1}} - \frac{1}{r_{C1P2}} + \frac{1}{r_{C2P2}}\right) \tag{2.5}$$

Where $\mathbf{r_{C1P1}}$ along with the others, are the absolute distance of the electrodes shown in Figure 1.

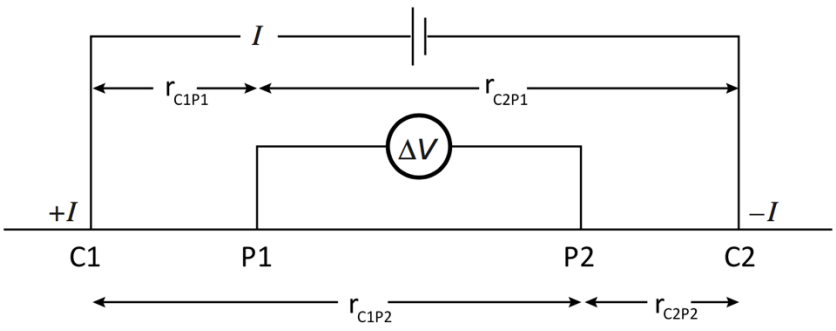

Figure 1. Standard electrodes configuration used in electrical resistivity surveys (modified from Kearey, Brooks, and Hill (2002))

Actually, in electrical resistivity surveys the medium is always not homogeneous and the measured parameter is the resistance **R** [Ohm]:

$$R = \frac{\Delta\phi}{I} \tag{2.6}$$

While the apparent resistivity $\boldsymbol{\rho_a}$ [Ohm·m] is computed according to the following equation:

$$\rho_a = k\frac{\Delta\phi}{I} \tag{2.7}$$

Where **k** is the geometric factor [m] depending on the electrodes configuration:

$$k = \frac{2\pi}{\left(\frac{1}{r_{C1P1}} - \frac{1}{r_{C2P1}} - \frac{1}{r_{C1P2}} + \frac{1}{r_{C2P2}} \right)} \tag{2.8}$$

Hence, once the resistance is measured, the computation of the apparent resistivity is straightforward. Indeed, combining the equations (2.6) and (2.7), the apparent resistivity is given by:

$$\rho_a = k \cdot R \tag{2.9}$$

The expression "apparent" related to the computed resistivity from the measured resistance, has been addressed since such value does not represent the proper "true" resistivity of the subsurface medium. As a matter of fact, the apparent resistivity is a value which corresponds to a resistivity value of a homogeneous ground with the same resistance and the same electrode configuration (Loke 2016a). Instead, the computation of the "true" resistivity is not straightforward and cannot be solved analytically. Therefore, an "inversion" procedure is used to compute the true resistivity value of the subsurface. The inversion problem and methods will be discussed in the last paragraph of this Chapter.

Beneath the surface, the electrical current can flow in three ways, namely: electronic conduction, electrolytic conduction and surface conductivity. In the first, the flow is carried by the free electrons and is typical in materials as metals. In electrolytic conduction, the flow is carried by the groundwater ions and it occurs in most environmental problems. On the other hand, surface conductivity is an intrinsic property of clay minerals and occurs at the interface between the groundwater fluid and clay grains.

As a result, the bulk resistivity of the subsurface media depends on mainly the groundwater conductivity and consequently on the porosity and saturation. Of course it is evident that exist a certain relationship between the fluid and the bulk resistivity. Such relation has been discovered by Archie (1942), and the equation is the following:

$$\sigma_b = \frac{\sigma_f}{F} \tag{2.10}$$

Where $\boldsymbol{\sigma_b}$ is the bulk conductivity [S/m], $\boldsymbol{\sigma_f}$ is the fluid conductivity and $\mathbf{F}$ is the formation factor [-] which is a function of porosity $\boldsymbol{\varphi}$ [-] (Cassiani, Binley, and Ferré 2006):

$$F = \frac{a}{\varphi^m} \tag{2.11}$$

Where **a** and **m** are empirical constants. However, such relation could be expressed in a different way, depending on other parameters. In case of clay sediments, the surface conductivity (σ_s) might not be negligible, and the general equation (2.10) becomes:

$$\sigma_b = \frac{\sigma_f}{F} + \sigma_s \tag{2.12}$$

Instead, in case of unsaturated rock the equation (2.10) can be generalised as follows:

$$\sigma_b = \frac{\sigma_f}{F} S_f^n \tag{2.13}$$

Where S_f is the fluid saturation [-] and **n** is another empirical constant [-].

Looking at the equations stated, it is obvious that a change of bulk conductivity can be due to a change of saturation, porosity or fluid conductivity. In particular, the last one also depends on salinity and temperature. In order to link the fluid conductivity and the temperature, there are two possible models to represent this relationship (Hayley et al. 2007). The exponential one is given by:

$$\frac{\sigma_{fT}}{\sigma_{f25}} = \exp\left[-\frac{A}{R}\left(\frac{1}{T} - \frac{1}{298}\right)\right] \tag{2.14}$$

Where σ_{fT} and σ_{f25} are the fluid conductivities at a temperature T and 25°C, respectively, **A** is the activation energy of conduction [J·mol^{-1}], **T** is the absolute temperature [K], **R** is the universal gas constant [J·mol^{-1}·K^{-1}]. On the other hand, the linear relation between conductivity and temperature is given by (Hayley et al. 2007):

$$\frac{\sigma_{fT}}{\sigma_{f25}} = m\left(T - 25\right) + 1 \tag{2.15}$$

Where again σ_{fT} and σ_{f25} are the fluid conductivities at a temperature T and 25°C, respectively, **m** is the fractional change of electric conductivity [-], while **T** is the relative temperature [°C].

Obviously there are further important petrophysical relationships in the literature. However, the aim of this Chapter is to give a theoretical introduction of the topics that will be used and discussed afterwards, therefore further and complex relations will not be discussed.

2.2 ERT arrays

So far, in electrical geophysical applications many electrodes arrays have been implemented and used. Their role does affect the field acquisition and therefore the resulting ERT profiles. As a matter of fact, the main differences between electrodes configurations depend on specific factors: sensitivity to the target of interest, signal-to-noise ratio, depth of investigation, lateral data coverage and the possibility on using in multichannel systems (Loke et al. 2013).

The most common electrodes configurations are shown in Figure 2. As a demonstration, three of those common configurations will be briefly described, namely Wenner (WN), dipole-dipole (DD) and multiple gradient (GN).

Wenner array is one of the simplest configurations. It has a good depth of investigation and good signal-to-noise ratio but poor spatial resolution and high anomaly effect, leading to do not always produce the best-resolved images (Dahlin and Zhou 2004).

Dipole-dipole is one of the most used arrays and will be used also in this thesis. It has generally good imaging resolution and is useful to detect vertical and dipping resistivity discontinuities. Despite that, it has but low signal-to-noise ratio and low penetration depth. However, dipole-dipole, along with multiple gradient configuration, is considered one of the best by Dahlin and Zhou (2004).

Instead, gradient configuration gives well-resolved images like dipole-dipole, it has good resolution but a signal-to-noise ratio comparable to the dipole-dipole one.

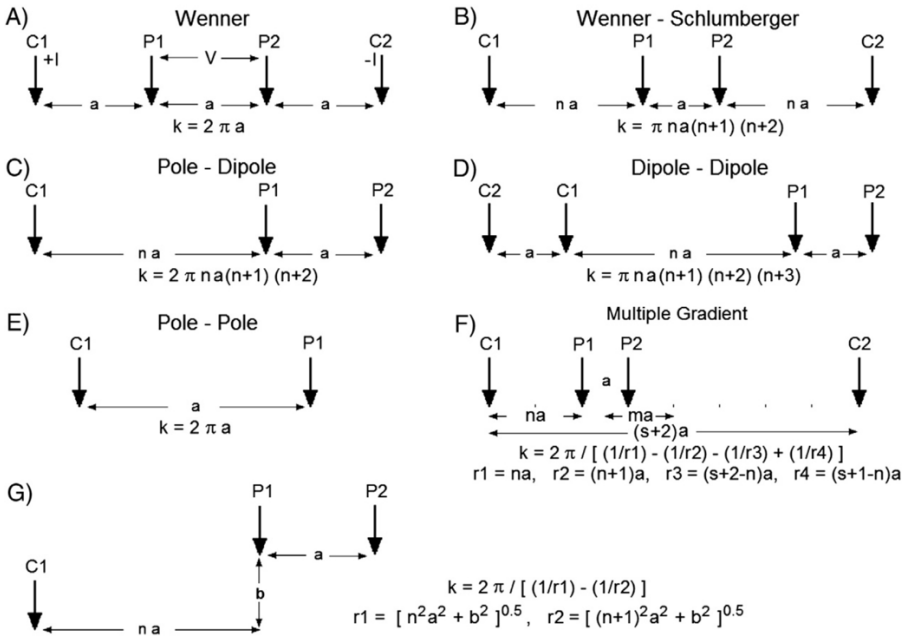

Figure 2. Common electrodes configurations (Loke et al. 2013).

As far as the characteristics of the arrays, 2D sensitivity of the resistivity and depth of investigation are two main properties of type of configuration, and they both depends on the sensitivity function. Theoretically, the sensitivity function shows how the resistivity of a subsurface region can influence the measurement. Therefore, considering a simple pole-pole configuration (i.e. just one current electrode and one potential electrode with electrode spacing equal to **a**), the 3D Fréchet derivative or sensitivity function is given by (McGillivray and Oldenburg 1990; Loke 2016a):

$$F_{3D}(x,y,z)=\frac{1}{4\pi^2}\cdot\frac{x\left(x-a\right)+y^2+z^2}{\left[x^2+y^2+z^2\right]^{1.5}\left[\left(x-a\right)^2+y^2+z^2\right]^{1.5}} \tag{2.16}$$

From the integration of the sensitivity function in **x** and **y** direction, the 1D sensitivity function is obtained. As a result, the analytical solution of the 1D sensitivity function is given by (Roy and Apparao 1971; Loke 2016a):

$$F_{1D}(z)=\frac{2}{\pi}\cdot\frac{z}{\left(a^2+4z^2\right)^{1.5}} \tag{2.17}$$

Such solution is also known as depth of investigation function and depends from array to array. As a matter of fact, this function might estimate the depth of investigation property of an

array. Although it is difficult to determine at which depth a measurement corresponds, some authors have tried to define a common value for the investigation depth. Some studies have used the maximum value of the function (i.e. the depth at which the sensitivity reaches the highest value) to define the depth value, but more interesting studies have shown another way. Indeed, Edwards (1977) has defined the "median depth of investigation" as the depth at with the sensitivity value is the median. In other words, this is the effective depth at which a specific array makes its measurement, defining the ability of an array to go deep. However, this is a rough estimation of the effective depth, and in cases where there are large resistivity values close to the surface, the effective depth might result different than the median one (Loke 2016a).

Integrating the sensitivity function (equation 2.16) in **y**, the 2D sensitivity property can be defined. The analytic solution has been given by Loke and Barker (1995) and, as mentioned before, it shows how much a resistivity change would influence the potential measured by the array. Therefore, the higher the sensitivity value, the bigger is the influence of the region on the measurement (Loke 2016a).

Nowadays, electric acquisitions are performed with multi-electrodes systems connected to a multi-core resistivity meter (Figure 3). Once the survey parameters (i.e. sequence of measurements, type of array, etc.) are transferred to the resistivity meter, the automatic acquisition starts. Considering the example shown in Figure 3 of a Wenner array with 20 electrodes, the acquisition phase starts by getting all the possible measurements with an electrodes spacing of **1a** (where **a** is the spacing between two adjacent electrodes Figure 3). Therefore, the first measurement uses electrodes in position 1, 2, 3 and 4; the second one uses electrodes 2,3,4 and 5; the procedure is repeated until the last **1a** spacing measurement is done. Once the **1a** spacing sequence is completed, the **2a** spacing sequence is carried out in the same way, followed by **3a**, **4a**, **5a** and **6a** spacing sequences (Loke 2016a).

For another kind of electric arrays (i.e. dipole-dipole, Wenner-Schlumberger, pole-dipole), the acquisition procedure is different. In particular, in dipole-dipole acquisition the first measurement is carried out with a **1a** spacing between both C1-C2 and P1-P2 electrodes. The first sequence of measurements is carried out with 1 as **n** factor (Figure 3), the second with **n**=2, and so on, until reaching normally **n**=6. Of course, increasing the dipole spacing to **2a** or more, would lead to increase the depth of investigation.

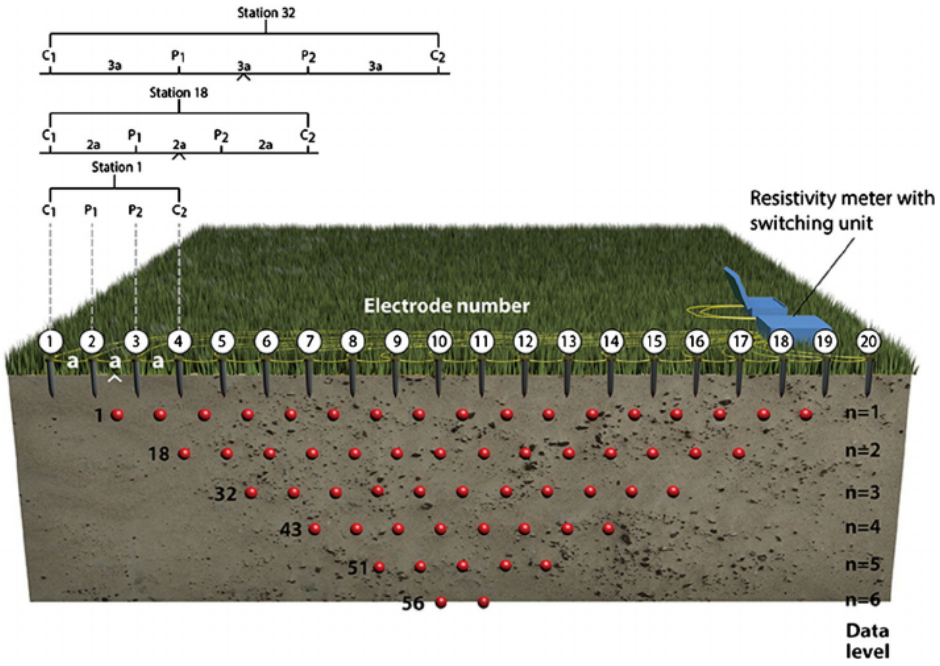

Figure 3. Schematic representation of a multi-electrodes acquisition system with a sequence of measurements (Wenner configuration) for a 2D model (Loke et al. 2013).

Generally, 3D acquisition intervenes and might be used when the limitations of 2D become important. The major assumption of 2D survey is to assume the subsurface not depending on the y-direction, i.e. to consider the subsurface as 2.5D. Although it might be suitable in some conditions, it is not the case in very heterogeneous sites (Van Hoorde et al. 2017).

In applications of 3D ERT, the acquisition phase has always been important, due to time-consuming problems. Therefore, the choice of the type of electrodes configurations in 3D acquisition should be properly defined. The 3D arrays used so far in literature include 2D arrays readapted to a 3D grid (i.e. pole-pole, pole-dipole and dipole-dipole mostly) and also specific configurations for 3D acquisition. Examples of specific 3D arrays are the "Maximum Yield Grid" array (Fiandaca and Cosentino 2008) and the "Cross-diagonal Survey" (Loke and Barker 1996). For the sake of simplicity, in this paragraph will be shown just one 3D configuration array, which has been also employed in the experiment related to this Thesis.

Besides the readapted array configurations from 2D ERT, studies have shown new powerful 3D acquisitions. For example, Cho and Yeom (2007) have proposed a new 3D acquisition called cross-line. This type of measurements is a 3D array configuration which allow to carry out potential measurements across two parallel lines. It might be used for performing both a full 3D measurements acquisition and a coupled acquisition between a classic 2D

configuration and the cross-line. The last case has been used by Van Hoorde et al. (2017) to study a karstic site with a 3D ERT survey coupling classic 2D inline dipole-dipole measurements with cross-line dipole-dipole measurements.

Cross-line measurements can be carried out in different array configurations. They can be added to the inline measurements to reduce the resistivity anomalies and to increase the uniqueness of the inverted model (Cho and Yeom 2007). However, cross-line arrays are generally derived from the classic configurations and the only difference is the y-position of the four electrodes. An illustrative example is shown in the figure below (Figure 4).

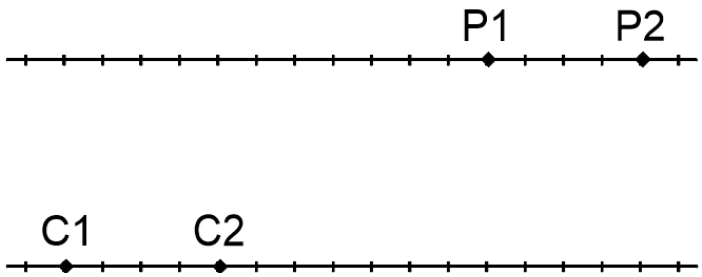

Figure 4. Illustrative example of cross-line dipole-dipole measurement (C are injection current electrodes and P are potential electrodes).

As far as the properties of the 3D arrays, they are quite simple, since they are the in most cases extensions of the 2D arrays. For the sake of simplicity, they will not be described again.

2.3 Inversion theory

As mentioned before, the ERT inversion process aims to find a model which is able to represent the measured data acquired in the acquisition phase. On the contrary, the forward problem gives the data values from a specific model parameter. Practically, the inverse problem aims to find a model (i.e. the model parameters are the resistivity values of the model cells) able to fit and represent the resistivity distribution from the measured apparent resistivity values, while the forward problem finds the potential distribution from a model (e.g. equation 3), function of the apparent resistivity.

In general, the inversion problems are characterised of three main problems which need to be faced, namely the existence of the solution, the uniqueness of the solution and the instability. Even though the existence is often verified, the presence of noise and the mathematical relation itself may lead to have do not find a model. If the existence is verified, the solutions might not be unique. This is actually the case of ERT acquisition. Finally, the inverse process might also be instable, leading to produce huge changes in the solution from a small change in the data

(e.g. due to noise). This particular last condition leads to have ill-posed or ill-conditioned inverse problems. Hence, it is common practice to adopt a Regularisation process which uses additional constrains to bias the solution towards a better model (Aster, Borchers, and Thurber 2013b).

Since ERT inversion problems are non-linear, let us assume that our inverse problem is represented by the following non-linear system:

$$\mathbf{G}(\mathbf{m}) = \mathbf{d} \tag{2.18}$$

Where **G** is the non linear operator of the model, **m** is the model of length *n* and **d** is the data vector of length *m*. Since in general there will not be an exact solution (i.e. $n<m$), useful solutions might find the best approximate solution to an inconsistent system of equations. As a matter of fact, a very common approach is to find a model which minimise the misfit values, also called residuals. In particular, the residual vector (**r**) is defined as the difference between the observed values (i.e. **d** data vector) and the predicted ones (i.e. **G**(**m**)):

$$\mathbf{r} = \mathbf{d} - \mathbf{G}(\mathbf{m}) \tag{2.19}$$

One common strategy to minimise the residual is to use L2-norm (i.e. the norm is the mean of the distribution). Such equation corresponds to the least-squares solution where the errors assume a normal distribution:

$$\left\|\mathbf{r}\right\|_2 = \sqrt{\sum_{i=1}^{m}\left(G_i(\mathbf{m}) - d_i\right)^2} \tag{2.20}$$

Alternatively, the L1-norm (also called robust norm) could be used to minimise the residual vector. In this case the norm assumes a Laplace distribution (i.e. the norm us the median of the distribution) and it relation is given by:

$$\left\|\mathbf{r}\right\|_1 = \sum_{i=1}^{m}\left|G_i(\mathbf{m}) - d_i\right| \tag{2.21}$$

While the root-mean-square (RMS) error is used to measure the error of the estimated model and is given by:

$$RMS(\mathbf{m}) = \sqrt{\frac{1}{m} \cdot \sum_{i=1}^{m} \left(\frac{G(\mathbf{m})_i - d_i}{\boldsymbol{\sigma}_i} \right)^2} \tag{2.22}$$

Where σ is the standard deviation of the data values.

In addition to the residual vector minimisation, a second constraint can be used, namely the norm of the model vector **m**. As a consequence, the inversion procedure would lead to minimise an objective function **Ψ** of the form:

$$\boldsymbol{\psi}(\mathbf{m}) = \left\| \mathbf{G}(\mathbf{m}) - \mathbf{d} \right\| + \boldsymbol{\lambda} \left\| \mathbf{m} \right\| \tag{2.23}$$

Where λ is the regularisation parameter or damping factor which balances the data misfit and the model constrain.

The inversion algorithm used in non-linear systems which is used as base in ERT inversion problems is known as Gauss-Newton algorithm (Aster, Borchers, and Thurber 2013a). In order to explain such algorithm, let us consider an objective function f(**m**) which aims to minimise just the weighted residual norm:

$$f(\mathbf{m}) = \sum_{i=1}^{m} \left(\frac{G(\mathbf{m})_i - d_i}{\boldsymbol{\sigma}_i} \right)^2 \Rightarrow f(\mathbf{m}) = \sum_{i=1}^{m} f_i(\mathbf{m})^2 \tag{2.24}$$

As stated before, the system is non-linear and this implies that an iterative process needs to be used. Therefore, the starting model $\mathbf{m_0}$ will be updated at each iteration by the model parameter change vector $\Delta\mathbf{m}$ in order to find the final solution **m** (Aster, Borchers, and Thurber 2013a). Let us decompose the objective function f(m) with Taylor series (Nguyen 2016):

$$\begin{aligned} & f(\mathbf{m}) = f(\mathbf{m}_0 + \Delta\mathbf{m}) \\ & f(\mathbf{m}_0 + \Delta\mathbf{m}) \approx f(\mathbf{m}_0) + \nabla f(\mathbf{m}_0)^t \Delta\mathbf{m} + \frac{1}{2} \Delta\mathbf{m}^t \nabla^2 f(\mathbf{m}_0) \Delta\mathbf{m} \end{aligned} \tag{2.25}$$

Then, in order to find the minimum of the previous equation, the derivative of the objective function has to be equal to zero:

$$\frac{\partial f(\mathbf{m}_0 + \Delta\mathbf{m})}{\partial \Delta\mathbf{m}} \approx 0 + \nabla f(\mathbf{m}_0) + \frac{1}{2} \nabla^2 f(\mathbf{m}_0) \Delta\mathbf{m} = 0 \tag{2.26}$$

Which leads to

$$\nabla f(\mathbf{m}_0) = -\frac{1}{2}\nabla^2 f(\mathbf{m}_0)\Delta\mathbf{m} \tag{2.27}$$

Successively, the gradient can be expressed as

$$\nabla f(\mathbf{m}_0) = 2\mathbf{J}(\mathbf{m}_0)^t \mathbf{F}(\mathbf{m}_0) \tag{2.28}$$

Where $\mathbf{F}(\mathbf{m}_0)$ is the vector valued function and $\mathbf{J}(\mathbf{m}_0)$ is the Jacobian matrix:

$$\mathbf{F}(\mathbf{m}_0) = \begin{bmatrix} f_1(\mathbf{m}_0) \\ \vdots \\ f_m(\mathbf{m}_0) \end{bmatrix}; \mathbf{J}(\mathbf{m}_0) = \begin{bmatrix} \frac{\partial f_1(\mathbf{m}_0)}{\partial m_1} & \cdots & \frac{\partial f_1(\mathbf{m}_0)}{\partial m_n} \\ \vdots & \ddots & \vdots \\ \frac{\partial f_m(\mathbf{m}_0)}{\partial m_1} & \cdots & \frac{\partial f_m(\mathbf{m}_0)}{\partial m_n} \end{bmatrix} \tag{2.29}$$

On the other hand, the approximated Hessian matrix obtained by dropping the higher order term (it is also called Gauss-Newton approximation) is given by:

$$\mathbf{H}(f(\mathbf{m}_0)) = \nabla^2 f(\mathbf{m}_0) \approx 2\mathbf{J}(\mathbf{m}_0)^t \mathbf{J}(\mathbf{m}_0) \tag{2.30}$$

Where the Hessian matrix is:

$$\mathbf{H}(f(\mathbf{m}_0)) = \sum_{i=1}^{m} \mathbf{H}(f_i(\mathbf{m}_0)^2) = \sum_{i=1}^{m} \mathbf{H}^i(\mathbf{m}_0)$$

$$\mathbf{H}^i(\mathbf{m}_0) = \begin{bmatrix} \frac{\partial^2 f_i(\mathbf{m}_0)}{\partial^2 m_1} & \cdots & \frac{\partial^2 f_i(\mathbf{m}_0)}{\partial m_1 \partial m_n} \\ \vdots & \ddots & \vdots \\ \frac{\partial^2 f_i(\mathbf{m}_0)}{\partial m_1} & \cdots & \frac{\partial^2 f_i(\mathbf{m}_0)}{\partial^2 m_n} \end{bmatrix} \tag{2.31}$$

Finally, the Gauss-Newton relation for the *k-th* iteration can be expressed as follow:

$$\mathbf{J}(\mathbf{m}^k)^t\mathbf{J}(\mathbf{m}^k)\Delta\mathbf{m}^k = -\mathbf{J}(\mathbf{m}^k)^t\mathbf{F}(\mathbf{m}^k) \tag{2.32}$$

Therefore, the iteration algorithm has the following steps (Nguyen 2016):

1. Choose $\mathbf{m}_0$ (just for the first time);
2. Solve the Equation 32;
3. Let $\mathbf{m}^{k+1}=\mathbf{m}^k+\Delta\mathbf{m}^k$;
4. Let k=k+1;
5. Check the convergence

Gauss-Newton method is considered the basic algorithm for ERT inversion, therefore many "updates" of such algorithm exist. As a matter of fact, it happens that the product $\mathbf{J}(\mathbf{m}^k)^t\mathbf{J}(\mathbf{m}^k)$ might suffer of singularity problems and a solution to this problem is the Levenberg-Marquardt method (also knows as "damped least-squares method") (Loke 2016a):

$$(\mathbf{J}(\mathbf{m}^k)^t\mathbf{J}(\mathbf{m}^k)+\lambda\mathbf{I})\Delta\mathbf{m}^k = -\mathbf{J}(\mathbf{m}^k)^t\mathbf{F}(\mathbf{m}^k) \tag{2.33}$$

Where $\mathbf{I}$ is the identity matrix and λ is the damping factor which aims to stabilise the solution.

However, even this method might be further improved with other constrains. Therefore, the equation 33 becomes (dropping the $(\mathbf{m}^k)$ notation) (Loke 2016a; Loke, Dahlin, and Rucker 2014):

$$(\mathbf{J}_k{}^t\mathbf{R}_d\mathbf{J}_k+\lambda_k\mathbf{W}^t\mathbf{R}_m\mathbf{W})\Delta\mathbf{m}_k = -\mathbf{J}_k{}^t\mathbf{R}_d\mathbf{F}_k-\lambda_k\mathbf{W}^t\mathbf{R}_m\mathbf{W}\mathbf{m}_{k-1} \tag{2.34}$$

Where $\mathbf{m}_{k-1}$ is the model resistivity vector of the previous iteration (however, it might be also changed with another model constraint); $\mathbf{W}$ is the matrix spatial roughness filter of the three dimensions; $\mathbf{R}_d$ and $\mathbf{R}_m$ are the two weighting matrices which allow to use either L1-norm or L2-norm (for the data vector and the model vector respectively) by means the iteratively reweighted least-square method (Farquharson and Oldenburg 1998); the remaining matrices and coefficients have been already described previously (Loke 2016a; Loke, Dahlin, and Rucker 2014).

Apart from the standard inversion techniques, in the recent years there was an increasing need to express the variations of subsurface resistivity in both space and time in general for monitoring purposes. Therefore, some authors have been able to develop new time-lapse inversion techniques to satisfy such needs (Loke et al. 2013). Three of the main time-lapse inversion techniques are the independent inversion, the time-constrained inversion and the

difference inversion. The last one uses the background model to constrain the successive models (LaBrecque and Yang 2001; Loke 2001). Instead, the time-constrained inversion technique tries to minimise the temporal changes between all models by using a temporal damping factor (Loke, Dahlin, and Rucker 2014). Finally, the independent inversion technique does not use temporal constrains of any type, leading to have simple independently inverted models (Loke 2001). In RES2DINV and RES3DINV, which are the software used in this Thesis to perform the ERT inversions, the independent and the time-constrained inversions are implemented. For this reason, just these techniques will be mentioned in this paragraph.

The time-constrain inversion technique can be considered as a further update of the Equation 2.33. As a matter of fact, at the Equation 2.34 a temporal damping term is added as it has been done to the spatial term. Consequently, the Equation 2.34 (or 2.33) becomes:

$$[\mathbf{J}_k{}^t\mathbf{R}_d\mathbf{J}_k+(\lambda_k\mathbf{W}^t\mathbf{R}_m\mathbf{W}+\alpha_k\mathbf{M}^t\mathbf{R}_t\mathbf{M})]\Delta\mathbf{m}_k=-\mathbf{J}_k{}^t\mathbf{R}_d\mathbf{F}_k-(\lambda_k\mathbf{W}^t\mathbf{R}_m\mathbf{W}+\alpha_k\mathbf{M}^t\mathbf{R}_t\mathbf{M})\mathbf{m}_{k-1} \quad (2.35)$$

Where the added parameters are: the weighting matrix $\mathbf{R}_t$ (similar to $\mathbf{R}_d$ and $\mathbf{R}_m$) which aims to choose the either the L1- or L2-norm for the temporal constraint; the sub triangular difference matrix **M** (its elements are either equal to 1 or -1) applied between the different time models; and the temporal damping factor α that attempts to minimise the temporal changes of the model. Obviously, higher values of the temporal damping factor lead to have similar models at the expense of a higher data misfit (Loke, Dahlin, and Rucker 2014; Loke 2016a).

Finally, the independent inversion technique used in RES2DINV and RES3DINV has normally the same form as the Equation 2.35, except for the time constrained term. In other words, the independent inversion can be obtained by just letting the temporal damping factor equal to 0 (Loke 2016b).

What has been discussed so far is valid in general for both 2D and 3D ERT inversion problems. As a matter of fact, 3D inversion is usually carried out in a similar way to the 2D inversion, where the main difference is that the algorithm does not force the resistivity values to vary across just x and z directions as in 2D inversions, but they vary across all directions. Even in this case, the 3D inversion algorithms will not be shown.

3 Heat storage experiment at Hermalle

In this chapter the materials and method of the experiment are generally described. With the aim to study the 2D&3D ERT time-lapse as a tool to monitor an aquifer thermal storage system, the 2-cycle heat storage experiment is described. A brief introduction of the site will be followed by the survey description and by the supporting technique (CTD monitoring). At the end, two paragraphs will describe the two inversion phases as well as the temperature conversion from the inverted results.

3.1 Previous studies on Hermalle site

The filed site used for the studied thermal monitoring experiment is sited in Hermalle-sous-Argenteau (13 km far from Liège), close to the Wallonia-Dutch, in Belgium (Figure 5). It is located on an alluvial aquifer of the Meuse river, 300 m far from it. Owned by the Wallonia Region, it has been used for several years by the hydrogeology and geophysics department of the University of Liège. As consequence, this location has been deeply studied and many hydrogeological, geophysical and geological information are available.

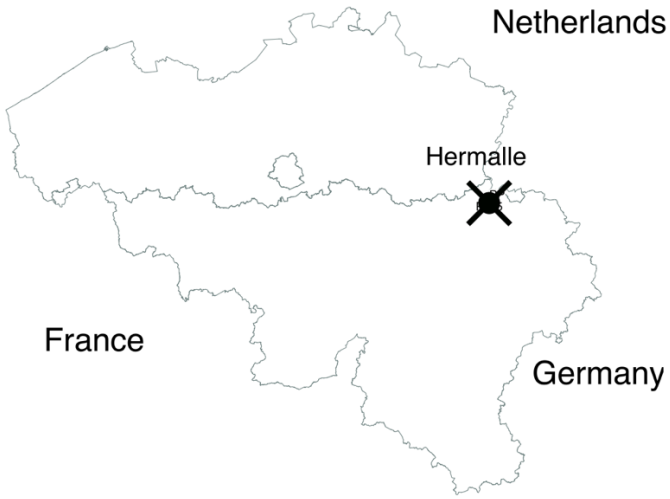

Figure 5. Hermalle-sous-Argenteau location in Belgium.

Brouyère (2001) in his PhD Thesis performed tracer tests in Hermalle site to obtain hydrodispersive parameters and to model both the tracer injection and the well-aquifer interactions.

Also Hermans (2014) in his PhD Thesis used Hermalle as field to perform practical case studies. In one field test he applied prior information to solve ERT inverse problems, while in

the second study he performed a cross-borehole time-lapse ERT to monitor a heat tracer experiment (Hermans et al. 2015).

Wildemeersch et al. (2014) have carried out a coupled tracer test in Hermalle using both hot water and naphtionate. With this study, they successfully obtained thermal and hydrogeological parameters such as effective porosity, heat capacity and retardation factor. Indeed, such parameters might result useful in calibration processes of thermal hydrogeological model or to estimate specific heat transfer parameters distribution by inverse modelling.

Klepikova et al. (2016) continued the study performed by Wildemeersch et al. (2014). In fact, with the temperature breakthrough curves they obtained the hydraulic conductivity distribution by inverse modelling. The study results have successfully demonstrated how this approach can characterise the hydraulic conductivity distribution or can be applied in thermal energy storage (ATES) projects.

3.2 Heat cyclic injection and pumping experiment

The heat injection experiment took place in Hermalle site and lasted almost 4 days, from the 21st to the 24th February 2017 (Figure 6). The experiment consisted in 4 phases by alternating each day injections of hot water and withdraws of groundwater. The piezometer used for injecting and pumping water is the "Pz15", located almost in the middle of an ERT grid. During the injections, groundwater was pumped from the piezometer "PP", heated with a ΔT of 30°C (the fuel boiler "Swingtec Aquamobile DH6" allowed to reach a maximum temperature between 40°C and 45°C) and then at the same time injected in piezometer "Pz15". Instead, pumping operations consisted in pumping water from "Pz15" and pouring it on an area outside the ERT grid. Both injection and pumping phases were carried out with a flow rate equal to 3 m^3/h (which corresponds to the maximum flow rate of the fuel boiler) for 5h with a surface pump.

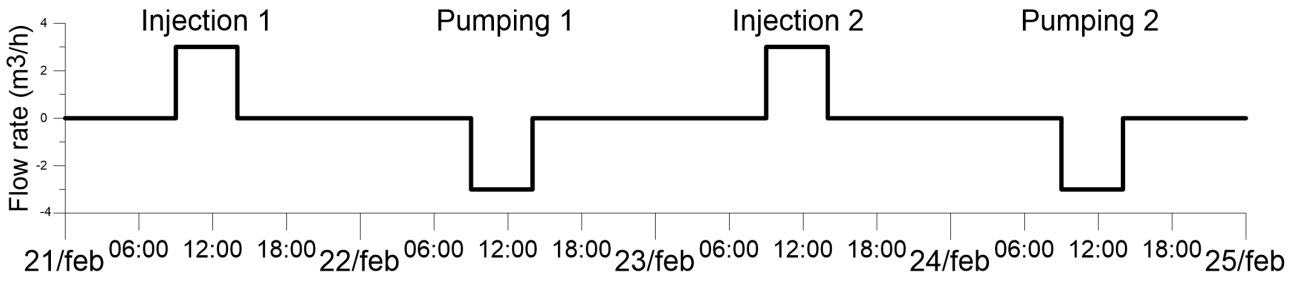

Figure 6. Time bar of the aquifer thermal energy storage cyclic experiment.

3.3 Geological and hydrogeological context

As mentioned before, the studied site is located on the alluvial plain of the Meuse river. The geology of Hermalle-sous-Argenteau area has a shaly bedrock which is composed of Visean and Houiller formations (Paleozoic). Such eroded bedrock is covered by the Quaternary alluvial formation of the Meuse Valley. The alluvial deposit has a thickness ranging between 5 and 15 m and has two kind of deposits. The fluvial loam at the top (thickness between 2 and 5 m) covers a gravel layer in a variable loamy, sandy or clayey matrix (thickness between 3 and 10 m) (Brouyère 2001).

The site is located on a flat area between the Albert Canal and the Meuse river (500 m far and 300 m far respectively) (Figures 7 and 8). Such position allows a constant head and a flow from the non-perfectly impervious Albert Canal around 0.2-0.3 m^3/s per meter of length. Therefore, the groundwater is fed by the canal and the rainfall, whilst discharge its flux just into the Meuse river since the bedrock is practically impervious (with a hydraulic conductivity between 10^{-8} and 10^{-6} m/s). The site is quite heterogeneous, in some area there are confining conditions in some unconfining, depending mostly on the loam layer. Furthermore, there are also some coarse gravel lens made by former Meuse channels (Brouyère 2001).

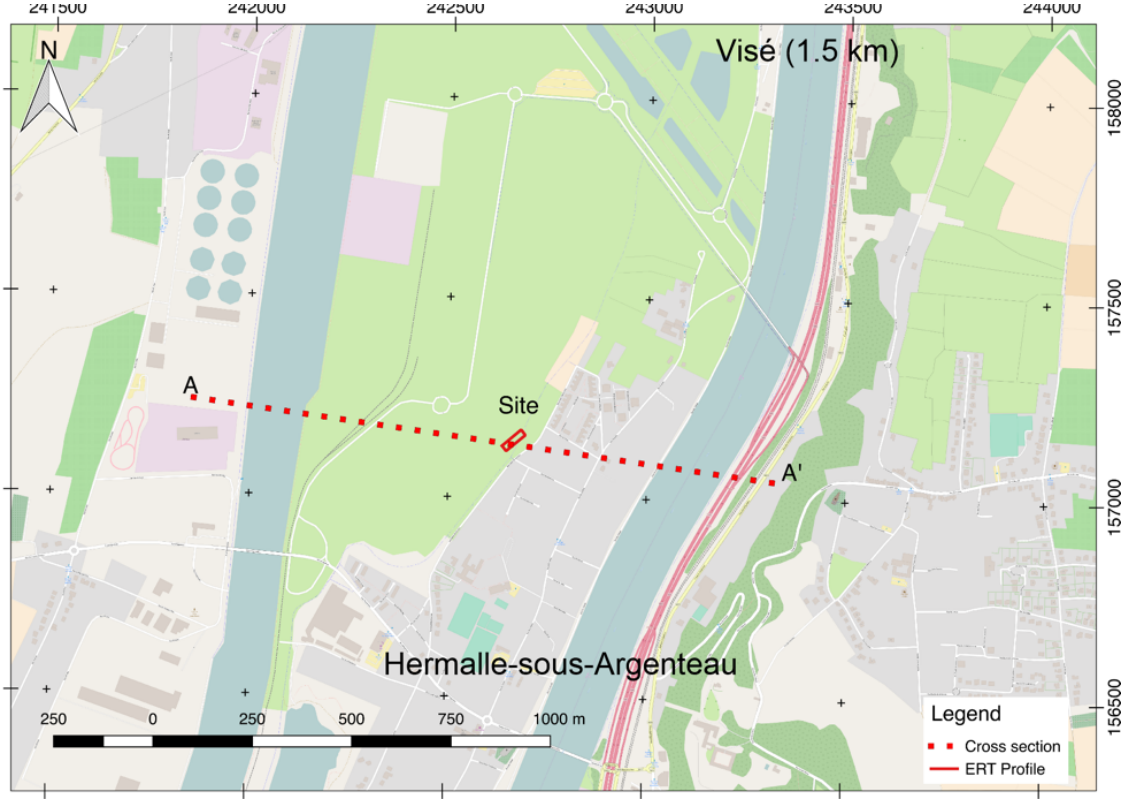

Figure 7. Hermalle site and cross section localisation (with Belgian Lambert cartographic coordinates).

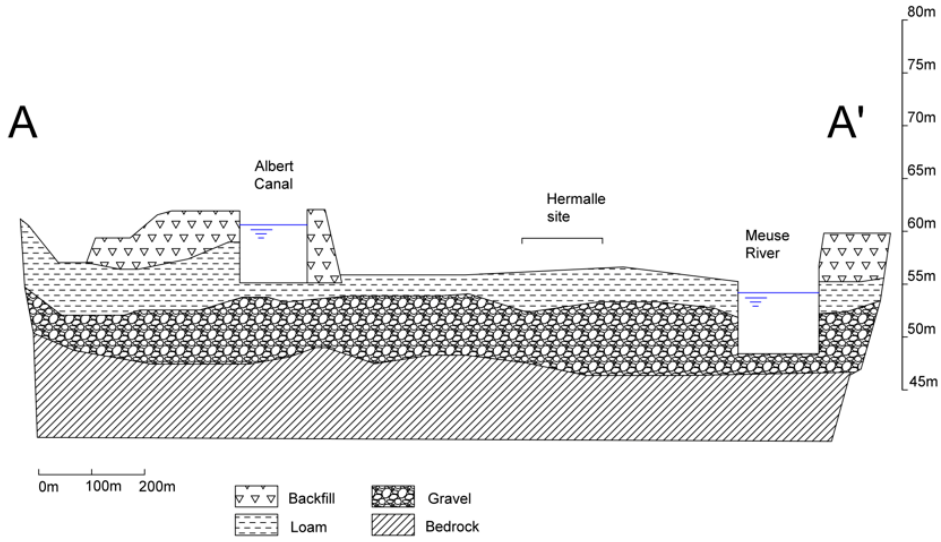

Figure 8. Cross section of Hermalle site area (Figure 7) (modified from Brouyère (2001).

From the former boreholes logs (Table 1), the subsurface can be divided in four main layers, two in the unsaturated zone and the other in the saturated one. The upper layer is mainly made of loam and clay deposit with a thickness of 1-1.5 m. The second layer consist of sandy loam with gravel which can reach a depth of 2-3.2 m. In the saturated zone, the third layer contains initially gravel in a sandy matrix deposit which increase its size until the bottom of the

layer, where big clean pebbles are present. The bedrock is the last layer which starts to appear at a depth of 9.7-10.1 m (Brouyère 2001; Wildemeersch et al. 2014; Hermans et al. 2015).

Borehole	Loam	Sandy loam (or loamy gravel)	Gravel	Bedrock	
Pz 13	0	1.4	3.2	10	From
	1.4	3.2	10	-	To
Pz 14	0	1.5	2.6	10	From
	1.5	2.6	10	-	To
Pz 15	0	1.5	2.2	9.9	From
	1.5	2.2	9.9	-	To
Pz 16	0	1.4	2.4	9.8	From
	1.4	2.4	9.8	-	To
Pz 17	0	1.4	2.4	9.8	From
	1.4	2.4	9.8	-	To

Table 1. Boreholes' logs in Hermalle site (modified from Hermans (2014)).

Finally, previous pumping and tracer tests performed on the site have allowed to obtain some hydrogeological parameters and information. First of all, the water table is normally at 3.2 m depth, but it has annual fluctuations of 0.5 m. The groundwater flows normally towards the North-Eastern (NE) direction. As far as the parameters, the hydraulic conductivity ranges between $2 \cdot 10^{-2}$ m/s and $7 \cdot 10^{-2}$ m/s, the longitudinal dispersivity between 0.5 m and 5 m and the effective porosity from 3.7% to 5.5% (Brouyère 2001). Instead, in the coupled tracer test of Wildemeersch et al. (2014), the effective porosity obtained was about 4% while the longitudinal dispersivity obtained was 3 m.

3.4 CTD monitoring

During the cycle experiment some supporting activities have been used. As a matter of fact, 5 of the 19 piezometers used for the already mentioned past experiments have been equipped with CTD probes (Figure 9). In particular, "Pz14", "Pz15" and "Pz16" are dual screen wells which have been equipped with 2 CTD probes, one at 5 m of depth and the other at 9 m of depth. On the other hand, "Pz13" and "Pz17" have been equipped with just one CTD at 5 m depth. The aim of the series of CTD probes was in general to monitor the variations of temperature, conductivity and hydraulic head during the cycle experiment but also to monitor the lateral diffusion of the thermal plume. Of course, just some piezometers have been used since farther piezometers would not have been affected. Finally, a ninth CTD probe has been used to work as a barometer for providing atmosphere pressure variations.

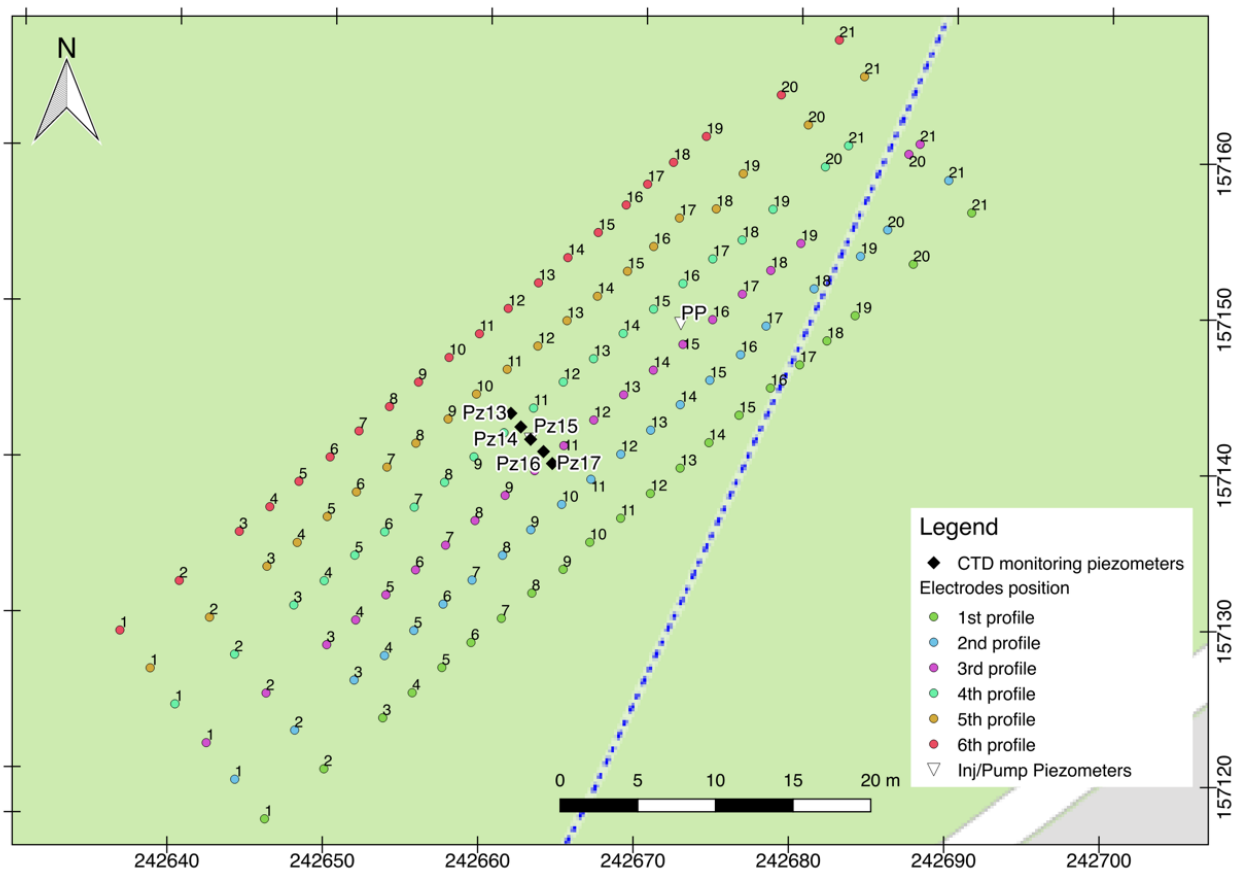

Figure 9. Hermalle site with monitoring piezometers, wells and ERT grid (with Belgian Lambert cartographic coordinates).

3.5 ERT acquisition (2D & 3D)

As mentioned before, the ongoing cycle experiment has been monitored by means of a permanent ERT electrodes grid in order to perform a 2D&3D time-lapse ERT acquisition (Figure 9). The grid has 6 parallel profiles with 21 electrodes per profile. Each single profile has a spacing of 3 m from the adjacent profile (y-spacing), while in each profile the electrodes are spaced by 2.5 m (except for the first and last electrodes of each profile which are spaced by 5 m) (x-spacing). Of course, the 6 profiles combined allowed to perform 3D acquisitions, each profile instead allowed one 2D acquisition.

The instrument "ABEM Terrameter LS" has been used to acquire the 2D&3D time-lapse data during the cycle experiment. The measurements have been acquired each 2 hours alternating normal and reciprocal measurements for a total amount of 37 acquisitions. Unfortunately, since in most time steps strong resistivity changes occurred, only in 5 time steps the reciprocal error analysis has been carried out.

During the 2D acquisition, a combined dipole-dipole and gradient array configuration has been used. As mentioned before, these two configurations give normally better results if compared with other common configurations. Dipole-dipole is able to detect vertical resistivity discontinuities (i.e. the hot water plume) but its depth of resolution is not very good. Since gradient and dipole-dipole arrays are complementary, they can be coupled to create a hybrid dipole-dipole gradient configuration. Besides the other characteristics of the gradient, in our case it can compensate the poor depth of penetration of the dipole-dipole array, improving the survey with better resolved resistivity acquisitions.

On the other hand, the 3D acquisition has been carried out using a dipole-dipole inline array, adding dipole-dipole cross-line measurements to obtain further 3D information. The data measured with dipole-dipole inline array are basically 2D data. Despite that, the dipole-dipole configuration is usually more sensitive to structure off array axis than other common arrays. Therefore, the elongated sensitivity pattern of the dipole-dipole array provides still 3D information although the inline measurements (Loke 2016a). Instead, the cross-line measurements acquired are taken still with dipole-dipole configuration, using different electrodes positions (i.e. with electrodes occupying 2 or more profiles). To conclude, the 3D dataset is not a full 3D dataset, with measurements taken from all the possible directions. It is instead a partial 3D dataset, which is somehow the compromise between accuracy of the model and time acquisition of the survey.

3.6 2D & 3D Inversion

First of all, before the inversion process a data filtering phase has been performed. As mentioned before, the reciprocal error analysis was not possible for the whole dataset. Therefore, it has been filtered taking into account the repetition measurements provided by the ABEM instrument. Furthermore, normally the standard deviation can measure twice the same wrong resistance value, while reciprocal measurements can detect just wrong electrode coupling. Having the standard deviation of each resistance value, it was possible to filter those values with a standard deviation higher than 5%. This filtering phase has been adopted for both the 2D and 3D dataset.

The 2D inversion process has been performed according to specific choices, mostly based on the experiment faced. First of all, the software used for carrying out the inversions is "RES2DINV", which is one of the most common used software for inverting 2D-resistivity surveys (Loke 2016b). Not all the 37 time steps have been inverted, but just 27 of them.

Indeed, for each phase (i.e. either injection or pumping) there have been selected the acquisition just before the action and the acquisitions between the end of the action and the beginning of the successive one. This means that for each profile, 4 inversions have been carried out, one per phase.

The inversion settings are the same for all the 2D inversions. To better understand the choices made, let us show the time-lapse inversion expression (i.e. the equation of the *k-th* iteration of the inversion algorithm) already mentioned in the Chapter 2 and present in RES2DINV algorithm (Equation 2.35) (Loke, Dahlin, and Rucker 2014):

$$[\mathbf{J}_k{}^t\mathbf{R}_d\mathbf{J}_k+(\lambda_k\mathbf{W}^t\mathbf{R}_m\mathbf{W}+\alpha_k\mathbf{M}^t\mathbf{R}_t\mathbf{M})]\Delta\mathbf{m}_k=-\mathbf{J}_k{}^t\mathbf{R}_d\mathbf{F}_k-(\lambda_k\mathbf{W}^t\mathbf{R}_m\mathbf{W}+\alpha_k\mathbf{M}^t\mathbf{R}_t\mathbf{M})\mathbf{m}_{k-1}$$

Where $\mathbf{R_d}$, $\mathbf{R_m}$ and $\mathbf{R_t}$ are the data, the model and the temporal weighting matrix, respectively, which allow to use either L1- or L2-norm optimisation in the iteratively reweighted least-squares method; the **J** is the Jacobian matrix at the *k-th* iteration; λ is the spatial damping factor at the *k-th* iteration; **W** is the spatial roughness filter matrix; α is the temporal damping factor at the *k-th* iteration; **M** is the temporal difference matrix; **Δm** is the model parameter change vector at the k-th iteration; **F** is the data misfit vector at the *k-th* iteration; and **m** is the model parameter vector at the *(k-1)-th* iteration.

First, a robust (L1-norm) data constrain for all the inversions has been chosen. Indeed, the robust inversion should avoid the remaining outliers, producing more reliable models at the expense of higher data misfit. On the other hand, the robust constraint was not suitable for the model parameters since it would have produced models with sharp resistivity variations. Thus, a smoothness-constrained least-squares regularisation (L2-norm) has been chosen for the model parameters. Indeed, the idea was to allow smooth resistivity variations in each model, as it is expected from the heat storage experiment. Furthermore, the L2-norm optimisation has been applied not only to the model change vector, but also to the model parameter vector (modify smoothness-constrained optimisation method). In this case, the aim was to ensure smooth variations and to avoid the noise. Finally, the last constraint chosen was the temporal one. Even in this case, the L2-norm has been used to constrain the resistivity changes between successive models since it is expected to have smooth changes from a time step to another during the ongoing experiment.

Concerning the spatial damping factor, it has been chosen manually with an initial value of 0.15 and a minimum value of 0.02. Furthermore, it has been increased with depth using an increasing factor of 1.05. On the other hand, the temporal damping factor has been chosen to

be fixed at each iteration and equal to 2.5 (normally it ranges between 0.5 and 5.0). This choice has been made because a value higher than 1.0 will result in obtain models more similar to each other, leading to avoid possible noise.

As far as the convergence limit, an RMS error up to 3.5% has been used to stop the inversion. As a matter of fact, using a robust data constraint implies higher misfit values, hence a high convergence limit has been chosen to avoid the inversion of noise and the consequent creation of artefacts.

The initial idea was to perform a 3D inversion using "RES3DINV" (Loke 2017) still with time-constrained technique to better compare the 2D and the 3D results together. Unfortunately, it was not possible to perform time-constrained due to technical problems with the inversion software. Therefore, an independent inversion has been used instead.

Differently from the 2D inversion, in this case just the time step belonging to the injection 1 have been inverted. Indeed, the 3D inversion has been carried out after the 2D results, and for some reasons due to the results that will be described in the Chapter 4, it has been decided to take into account just the first phase. Furthermore, the use of the independent inversion would have inverted more noise, especially in the later time-steps. Of course, the time steps have been selected in the same way as 2D inversion: one time step before the injection 1, plus all the other time steps after the injection 1 but before the pumping 1.

In general, in the 3D inversion settings, it has been tried to maintain the same choices made in the 2D inversion. Despite that, some adjustments have been made to compensate the use of the independent method. The data constraint was the L1-norm method, since is less sensible to noise. Even in the model constraint it was chosen the robust inversion method. The reason was to better spot possible heterogeneities in the subsurface.

As far as the spatial damping factor, it has been chosen again manually. However, there have been preferred higher values (initial value of 0.3 and minimum value of 0.01), to better overcome the different performances of the independent inversion. Finally, the RMS convergence limit has been fixed to 5%.

3.7 Temperature conversion

In the temperature conversion process, it has been mainly taken advantage of the linear petrophysical relation previously described between the fluid conductivity and the temperature (Equation 2.15). It can be rewrite as follows (Hayley et al. 2007):

$$\frac{\sigma_{f1}}{\sigma_{fR}} = m_f(T_1 - T_R) + 1 \tag{3.1}$$

Where σ_{f1} and σ_{fR} are the fluid conductivity at reference temperature (T_R) and temperature of state 1 (T_1).

Instead, the relation between the fluid conductivity and the bulk one can be expressed from Archie's Law (Equation 2.10), where considering the formation factor constant and two different states, it becomes:

$$\frac{\sigma_{b2}}{\sigma_{b1}} = \frac{\sigma_{f2}}{\sigma_{f1}} \tag{3.2}$$

Where σ_{b1} and σ_{b2} are the bulk conductivity at state 1 and 2, while σ_{f1} and σ_{f2} are the fluid conductivity at state 1 and 2. Considering these states correspondent to two different time steps, from the inversion models the two bulk conductivity values are obtained. Then, once one fluid conductivity is known, the other is easily obtained. Therefore, combining the Equations (3.1) and (3.2), the temperature at state 2 (T_2) is obtained by:

$$T_2 = \frac{1}{m_f}\left[\frac{\sigma_{b2}}{\sigma_{b1}} \cdot \frac{\sigma_{f1}}{\sigma_{fR}} - 1\right] + T_R \tag{3.3}$$

Hermans et al. (2015) in their study have analysed the empirical relation between the formation water conductivity and the temperature (with values ranging from 10 to 40°C) with a groundwater sample taken from Hermalle site. For simplicity, in our case there have been used the same empirical results to estimate the constant coefficient m_f for the Equation (3.3). As a matter of fact, the fractional change in conductivity per Celsius degree (m_f), obtained by the fitting curve of the experimental points, was 0.0194. The reference temperature has been considered equal to 25°C. Instead, the temperature at state 1, has been assumed equal to the average temperature of the aquifer half hour before performing the injection 1 (i.e. 12.6°C 8:30 am, 21/02/2017). In particular, such assumption has been carried out taking into account the temperature values of all CTD probes at 5 m of depth (i.e. 5 CTDs out of 8). Successively, the formation water conductivity ratio (σ_{f1}/σ_{fR}, Equation 3.1) can be easily computed.

To solve the Equation (3.3), the missing parameter is the bulk conductivity ratio (σ_{b2}/σ_{b1}). Since the inversion results are expressed in terms of percentage change of resistivity, we might

express the Equation (3.3) in these terms instead of conductivity. After some passages, the Equation (3.3) becomes:

$$\frac{\sigma_{b2}}{\sigma_{b1}} = \frac{\frac{1}{\rho_{b2}}}{\frac{1}{\rho_{b1}}} = \frac{\rho_{b1}}{\rho_{b2}} = \left(\frac{\rho_{b2}}{\rho_{b1}}\right)^{-1} = \left(\frac{\rho_{b2}+\rho_{b1}-\rho_{b1}}{\rho_{b1}}\right)^{-1} = \left(\frac{\rho_{b2}-\rho_{b1}}{\rho_{b1}}+1\right)^{-1} \Rightarrow$$

$$T_2 = \frac{1}{m_f}\left[\left(\frac{\rho_{b2}-\rho_{b1}}{\rho_{b1}}+1\right)^{-1} \cdot \frac{\sigma_{f1}}{\sigma_{fR}} - 1\right] + T_R \qquad (3.4)$$

Where ρ_{b1} and ρ_{b2}, are the bulk resistivity values obtained from the inversion at state 1 and 2 respectively, and the ratio $(\rho_{b2} - \rho_{b1})/ \rho_{b1}$ is the percentage change of resistivity between the time step 1 and 2.

Therefore, each cell of the inverted model has a temperature value given by the Equation (3.4). However, this conversion can be used just for the first phase, the Injection 1. As a matter of fact, the second phase depends somehow on the results of the first phase, the third depends on the second phase and so on. This is due to the inversions, which have been performed separately, one per phase. Consequently, the previous temperature conversion computation needs to be adapted for the three remaining phases.

Let us consider the second phase, namely the Pumping 1. In this case, the background time step of Pumping 1 is also the last time step of Injection 1. This means that for the background time step of Pumping 1, each cell has a temperature value already computed. Hence, the formation water conductivity can be easily computed for each cell using the Equation (3.1) between the reference temperature and the computed temperature. Once the formation water ratio has been computed for each cell, the temperature values can be easily obtained by using the Equation (3.4), as it has been done before.

For the following phases, the conversion computation can be easily performed in the same way.

In conclusion, the assumptions made can be sum up as follows:

- Resistivity changes produce only temperature changes;

- The initial temperature of the aquifer (and therefore also the formation water conductivity ratio) is the same for all profiles and set to half hour before the Injection 1;
- The coefficient m_f has been assumed to be constant in all profiles and derived from just one groundwater sample taken few years ago by Hermans et al. (2015). However, the value is acceptable since it is in the same range as previously studies like Hermans et al. (2012) and Hayley et al. (2007).

4 Results and interpretation

In this Chapter the results of methods previously described in Chapter 3 will be shown and discussed. In particular, direct measurements results will be first shown and discussed. They are used indeed as basis to compare the following inverted resistivity models. Once done, the inversions results will be introduced. Next, the resistivity changes models are shown and discussed. The aim is to show the goodness of these results to monitor the performed heat cycle experiment. Successively, these models are elaborated to represent resistivity changes in terms of temperature values. The temperature models obtained will be shown and discussed, with the aim to understand whether they facilitate the interpretation of resistivity changes or not. Finally, also the 3D models are shown and discussed, with a focus on the first injection performed. Therefore, 3D resistivity models are used to better characterise the heterogeneity of the site and confirm the 2D results previously obtained.

Finally, during the discussion of the results, it has been tried to show and highlight successful and unsuccessful aspects, criticising impartially the results.

4.1 CTD monitoring

In this section the monitoring support results are shown and discussed. In particular, the temperature and conductivity variations are analysed and discussed with a particular attention to the first one. As mentioned before, the groundwater level was not monitored since the barometer probe was lost during the experiment.

These results will then be useful to characterise the goodness of the temperature conversion results. In addition to that, from these direct measurements first considerations can be formulated.

4.1.1 Results and interpretation

As previously shown, the 5 equipped piezometers are located almost in the middle of the ERT grid, where their axis crosses profile 3 and 4 (Figure 9). All the CTD probes have been analysed, with the aim to compare the temperature and conductivity variations along with the injection and pumping phases.

4.1.1.1 Piezometer "Pz13"

The piezometer "Pz13" is a single screen monitoring well which is located between the 4th and the 5th profile of the ERT grid (Figure 9). The following graph (Figure 10) shows the temperature trend of the CTD probe at 5 m depth during the heat storage cycle experiment compared with the injection and pumping phases performed.

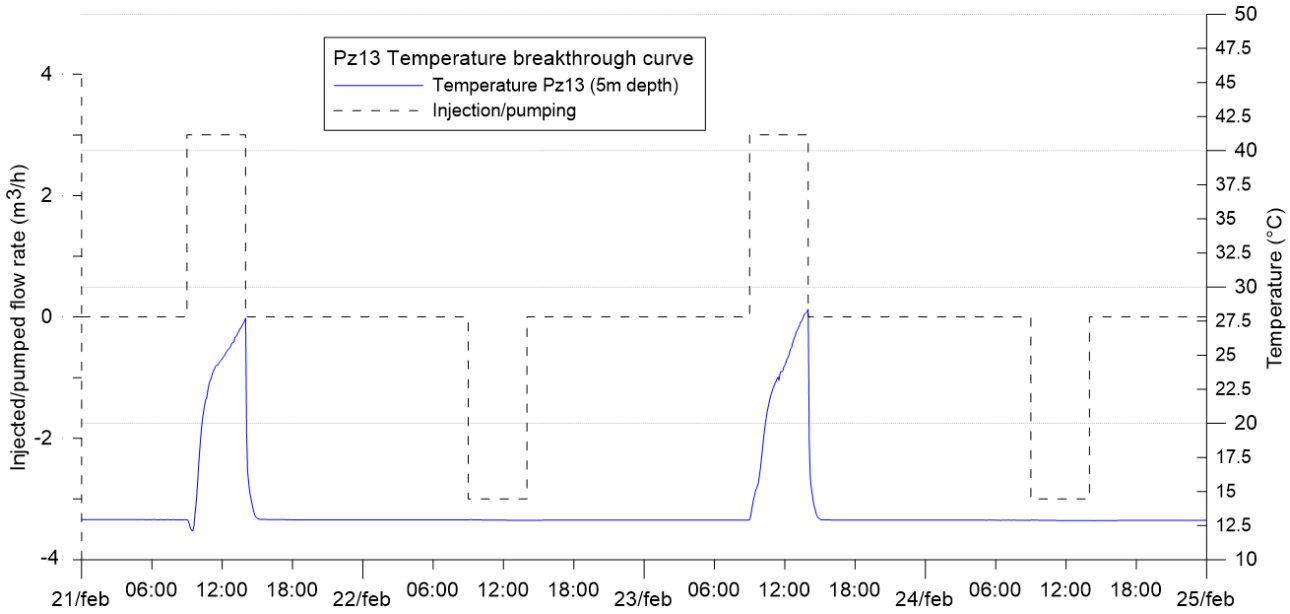

Figure 10. Temperature breakthrough curve of "Pz13" probe.

The first change happened just after the Injection 1. Since it is a light negative change (lower than 1°C) lasted in the first injection instants, it is not relevant and considered in the analysis. After 45 min of the injection, the temperature increased by almost 1°C. Since then, the temperature values kept increasing until reaching the peak at the end of the injection (i.e. 2:00 pm, 21st February), which corresponds to 27.72°C. Successively, there was a sharp decrease where the temperature reached the initial temperature in almost 1 h and 20 min.

The second and last sharp temperature change occurred just after the Injection 2. In this case, the temperature increased by 1°C in almost 15 min. Of course, they kept increasing until the end of the injection, where they reached the peak at 28.37°C. As in the Injection 1, a sharp decrease followed the end of the injection in 1 h, reaching the initial temperature.

Despite the two large temperature changes registered, the two pumping phases have not influenced the temperature values of "Pz13" probe.

As far as the conductivity variations, they were not acquired in this piezometer since the probe used in "Pz13" is a Mini-Diver probe with only two acquisition channels (i.e. temperature and pressure).

4.1.1.2 Piezometer "Pz14"

The piezometer in question is a dual screen monitoring well equipped with two probes, one CTD-Diver and the other Mini-Diver at 5 m and 9 m depth respectively. The following graph (Figure 11) shows the temperature variations of the two probes during the experiment, still compared with the injection and pumping phases.

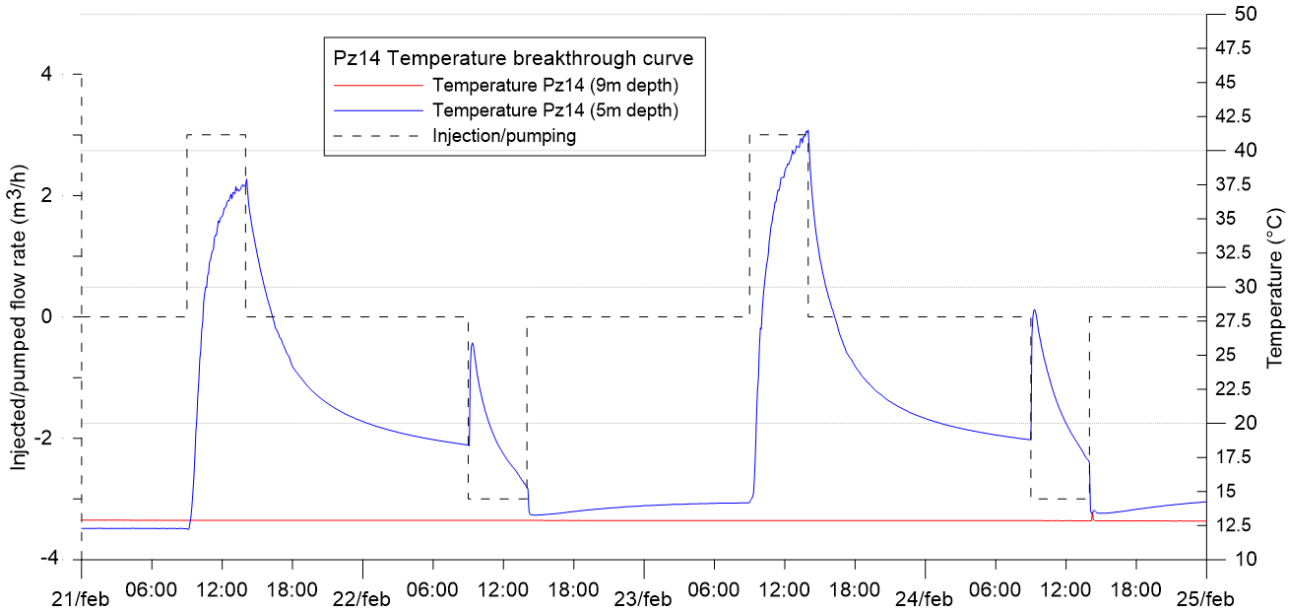

Figure 11.Temperature breakthrough curve of "Pz14" probes.

As expected, the first sharp increase in the 5 m deep probe occurred just after the beginning of Injection 1. In particular, after almost 20 min the temperature grew of 1°C, until its peak of 37.92°C, 5 min after the end of the injection. A following exponential decreasing phase occurred, where temperature values reached a minimum of 18.41°C at the beginning of the pumping phase.

Right after the beginning of the Pumping 1, the temperature underwent a sharp increase up to 25.91°C just 20 min after the beginning of the phase. After this peak, values decreased exponentially until 5 min after the end of the pumping phase, reaching 15.21°C. This phenomena, is probably due to the previously injected warm water close to the well which has been "re-called" by the pumping phase.

Then, 25 min after the end of the phase, temperature fell again reaching a minimum value of 13.29°C (i.e. 1°C higher than the initial temperature). Since then, a slow increasing phase took place, where temperatures reached 14.2°C at the beginning of the Injection 2. This slow increase can be addressed to the heat stored by the rock matrix, which was able to warm up the groundwater even after the injection.

Next, from the beginning of the Injection 2, temperatures started to increase logarithmically as usual. They reached the peak of 41.52°C at the end of the injection phase. Again, an exponential decrease took place until the temperatures reached the minimum value of 18.81°C at the beginning of Pimping 2.

As in the Pumping 1 phase, 20 min after the beginning of Pumping 2 a sharp increase of temperatures occurred (reaching 28.34°C). After the peak, temperatures decreased until the end of the pumping phase (reaching 17.13°C). Even in this case, the cause is attributed to the warm water in the vicinity of the well.

After 15 min the end of the last pumping phase, the temperature values fell sharply to 13.37°C. A slow increasing phase followed the end of the pumping phase, where temperature increased from 13.4°C to 14.7°C. The peak started 1 day and 4.5 h after the end of the pumping and lasted 10 h. After that, a slow decreasing phase started. As before, this behaviour might be addressed to the heat stored in the rock matrix which apparently exhausted the heat after almost 1 day and 14 h.

On the other hand, the temperature trend at 9 m depth is flat and no slight influences are detected.

The conductivity variations are shown in Figure A1 in Annex. The conductivity trend is coincident to the temperature one. However, the variations are not sharp and the extreme conductivity values are 0.763 and 0.802 mS/cm. Finally, the same considerations done in the temperature breakthrough curve can be applied.

4.1.1.3 Piezometer "Pz15"

The piezometer "Pz15" is located between the Profile 3 and 4, and it has been also used as injection and pumping well during the experiment. Since it is a dual screen monitoring well, it has been equipped by two CTD-Diver, one at 5 m depth and the other at 9 m depth. As done before for the other piezometers, the following graph shows the temperature variations at 5 and 9 m depth (Figure 12) along with the injection and pumping phases.

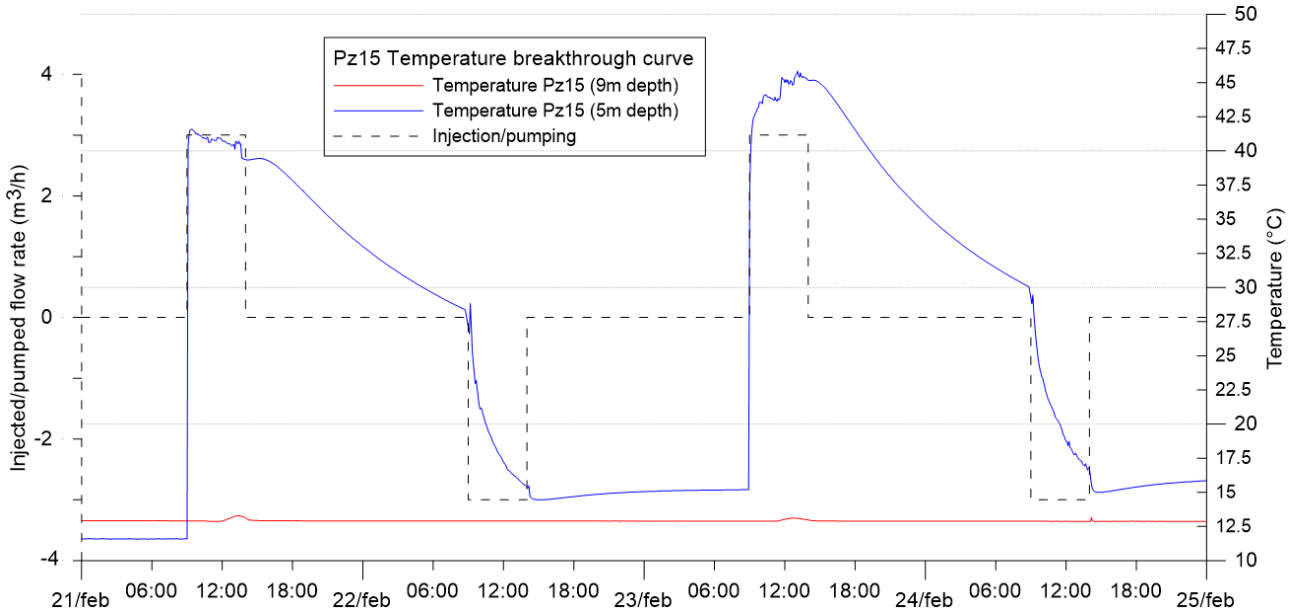

Figure 12.Temperature breakthrough curve of “Pz15" probes.

Right after the beginning of Injection 1, temperature increased sharply in 10 min reaching the peak of 41°C. During the injection, temperature values were almost stable, oscillating between 41°C and 39.4°C. This light unstable behaviour is probably due to the fuel boiler which is not able to maintain a perfectly fixed temperature value. Furthermore, it occurred just in this borehole because is the one used for the injections, which means that is in direct contact (precisely just half meter below the injection point) with the warm water.

Once the injection phase is ended, temperature started to decrease exponentially until they reached a value of 28.36°C. Successively, when the Pumping 1 started, a steeper exponential decrease has occurred. At the end of the pumping phase, the values reached 15.31°C.

Completed the Pumping 1, the temperatures assessed to 14.45°C. Then, 50 min after the end of the pumping phase they started a slow growth until reaching 15.19°C. After that, Injection 2 started and temperatures grew suddenly, oscillating between 39.8°C and 45.73°C during the injection phase. The instability of temperature values is due to the same reason as Injection 1.

After the end of the third phase, temperatures decreased exponentially from 45.17°C to 30°C. As before, a steeper exponential decreasing phase followed the beginning of Pumping 2, where temperatures fell from 29.5°C to 16.75°C.

Then, an assessing phase followed the end of the last pumping phase where temperatures dropped from 16.75°C to 15°C in 40 min. Next, temperature grew slowly from 15°C to 16.05°C in almost 22 h. After that, they start to decrease slowly, loosing 1°C in 67 h.

Regarding the temperature variations at 9 m depth, their trend is almost flat whit values ranging between 12.86°C and 13.28°C (i.e. variations are lower than 0.5°C). Despite that, in the graph (Figure 12) are still visible two bell-shaped variations corresponding to the two injection phases. Instead, pumping phases did not affect the temperature variations significantly. The only slight variation in pumping phases is observed 10 min after the Pumping 2. As a matter of fact, temperature increased and decreased suddenly in 5-10 min from 12.87°C to 13.16°C for assessing again at a temperature close to 12.87°C. This is probably an assessing phase due to the sudden stop of the pumping phase.

As far as the conductivity breakthrough curve, it has generally the same trend as the temperature variations (Figure A2 in Annex). Similarly, to the other CTD probes, it is highly variable during the injections and less in the pumping phases. However, the conductivity breakthrough curve of "Pz15" has a higher range of values, ranging between 0.55 and 1.1 mS/cm. Even in this case, the same considerations done for the temperature curve are applied to the conductivity variations.

4.1.1.4 Piezometer "Pz16"

Piezometer "Pz16" is the symmetric borehole of "Pz14", with "Pz15" as the symmetric axis. As "Pz14", "Pz16" is a dual screen well with a Mini-Diver and a CTD-Diver probes at 9 m and 5 m depth respectively. The following graph shows the temperature monitoring results of both probes (Figure 13)

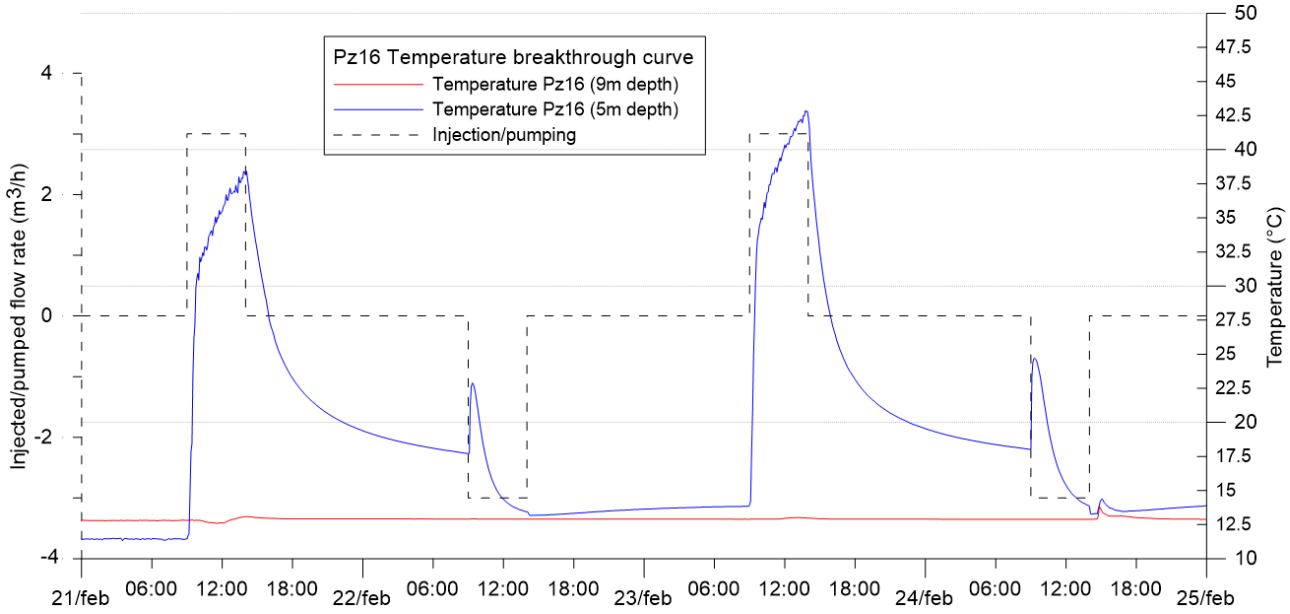

Figure 13. Temperature breakthrough curve of "Pz16" probes.

The temperature variations of “Pz16” at 5 m depth are practically identical to “Pz14” ones. Therefore, for the sake of simplicity the common variations along with the considerations will not be described, whilst the main differences will be highlighted.

To better appreciate the differences between “Pz14” and “Pz16” temperature variations at 5 m depth, the two breakthrough curves have been compared and shown in Figure A4 in Annex. Looking at the comparing curve, it is pretty evident that both curves are very similar and they differ between each other alternatively. As a matter of fact, “Pz16” curve overcomes the other curve just in the two injection phases with a difference that can exceeds 1°C. On the other hand, “Pz14” has often higher temperatures than “Pz16” ones. In pumping phases, the difference can be even higher than 4°C, while between injection and pumping phases the difference reach values up to 0.8°C.

As far as the temperature variations at 9 m depth, although the curve is almost flat, they are not similar to “Pz14” ones. Instead, similarly to “Pz15” curve at 9 m depth, “Pz16” curve has two bell-shaped variation matching the two injection phases. The first injection has a sinusoidal oscillation going from 12.81°C, decreasing to 12.6°C, re-increasing up to 13.09°C and stabilising at 12.91°C. The second slight variation occurred during the second injection and went from 12.9°C to 13°C, for stabilising again at 12.91°C. Finally, a little sharp alteration similar to the one seen in “Pz15” occurred right after the end of Pumping 2. Even in this case, the cause is probably due to the assessing phase after the stop of the withdrawal.

The differences previously described between “Pz14” and “Pz16” lead to assume some evidences. Indeed, the two piezometers probes should obtain very similar results since they are symmetric. Thus, the slight differences found might somehow confirm that the subsurface is heterogeneous, despite the short distance. Indeed, the higher temperatures reached in injections at “Pz16” location might indicate that the zone has higher porosity than “Pz14” one and more sensible to hot water injection and withdrawal.

Finally, the considerations made on the temperature variations can be extended to the conductivity breakthrough curve. As seen in the other probes, also temperature and conductivity curves of “Pz16” (Figure A3 in Annex) are very similar to each other. Instead, the conductivity values in this case range between 0.74 and 0.79 mS/cm.

4.1.1.5 Piezometer "Pz17"

The last piezometer used is "Pz17". As "Pz13", it is a single screen well equipped with just one Mini-Diver probe. As usual, the following graph represents the temperature breakthrough curve of the probe at 5 m depth (Figure 14).

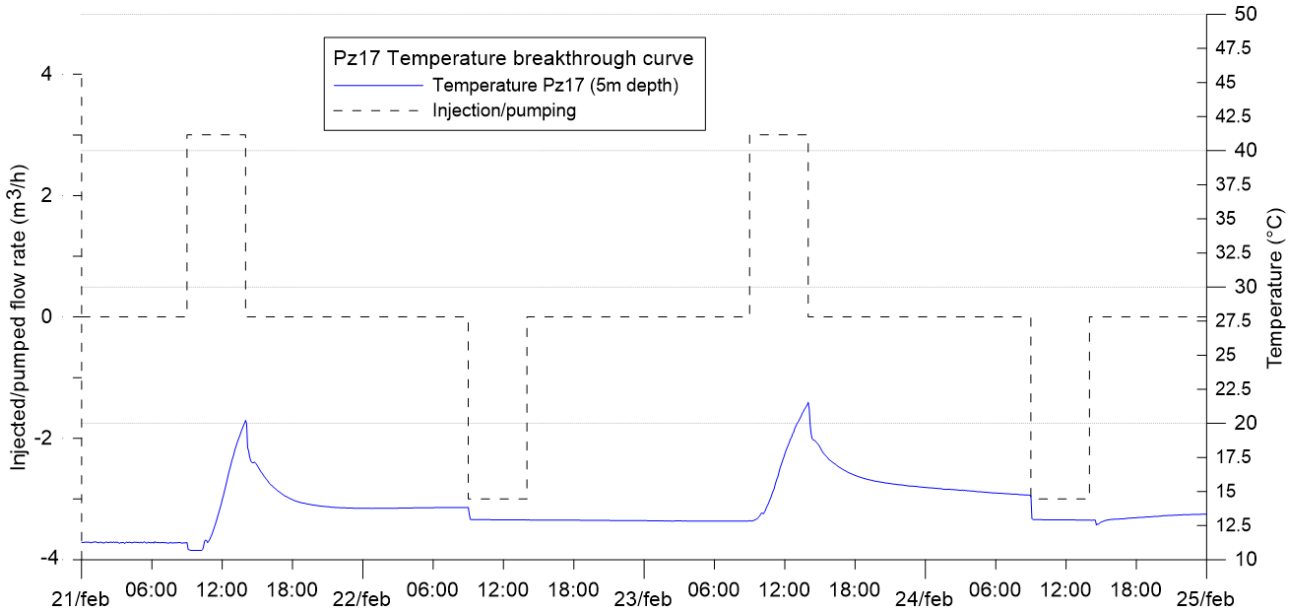

Figure 14. Temperature breakthrough curve of "Pz17" probe.

Even though the trend of "Pz17" curve is similar to the other breakthrough curves, there are differences in terms of temperature magnitude. As done for "Pz14" and "Pz16", the Figure A5 in Annex shows and compares the two breakthrough curves of the symmetric piezometers "Pz13" and "Pz17". The main differences are mostly located in the injection phases and in the assessing phase right after the injections. Indeed, in "Pz17" breakthrough curve, temperatures struggle to grow in injection phases, reaching peak values of 20.22°C and 21.55°C (rather than 27.72°C and 28.37°C in "Pz13") in Injection 1 and 2 respectively.

On the other hand, in the recovery phase after the injections, temperatures dropped slowly than "Pz13" ones. In particular, they diminished up to 13.83°C and 14.7°C right before Pumping 1 and 2 respectively. Finally, in "Pz17" the initial temperature (11.24°C) grew after the injections and withdrawals, reaching a minimum value of almost 12.88°C. This means that the heat storage capacity of "Pz17" area is better than the "Pz13" one. As confirmation, computing the area between the curves and their initial temperatures, it comes out that the area of "Pz13" is 4.09 while the "Pz17" area is 10.47.

Moreover, from these considerations the same heterogeneity conclusion made from the comparison of "Pz14" and "Pz16" can be done. As a matter of fact, the area of "Pz17" seems

to have a lower porosity than “Pz13” one. Indeed, in “Pz13” temperature curve sharp changes with higher peaks occurred, at the expenses of worse heat storage capacity. However, this is still an evidence coming from some direct measurements that represent just punctually hydrogeological behaviour of the site. Therefore, further evidences need to be found.

4.2 2D time-lapse inversion

In this paragraph, the results of the 2D time-lapse inversions will be shown and discussed. Before showing the results, a brief introduction on the inverted models will be followed by a description of the image quality assessment results. The idea is to have a first glimpse of the models quality before showing them. Thus, the discussion of the results will be linear and easy to understand.

Successively, the background images will be described and interpreted. To give a basis for the representation of the 2D models, a common background error is estimated for all profiles.

Finally, the 2D resistivity models will be discussed and shown in terms of resistivity percentage changes. Injection and pumping operations should lead to produce a heat water plume towards the groundwater flux direction (NE). As mentioned before, in these results we expect to monitor such plume and see mostly negative changes, but also some positive ones. Negative resistivity changes are related to higher temperature caused by both injection and pumping operations, while positive changes might be related to cold water recalled by pumping operations.

4.2.1 Results and discussion

From the 2D ERT inversions carried out, there have been obtained a total amount of 162 resistivity models. The RMS errors of all models are shown in Table A1 in Annex. The models are divided in 6 profiles, 27 time steps and 4 phases (Table 2).

Time step	Time instant from the beginning of (phase)	Phase
3	-14h (Injection 1)	Background
5	-10h (Injection 1)	
10	+6h (Injection 1)	Injection 1
11	+8h (Injection 1)	
12	+10h (Injection 1)	
13	+12h (Injection 1)	
14	+14h (Injection 1)	
15	+16h (Injection 1)	
17	+0h (Pumping 1)	Pumping 1
18	+2h (Pumping 1)	
19	+4h (Pumping 1)	
20	+6h (Pumping 1)	
21	+8h (Pumping 1)	
22	+10h (Pumping 1)	
24	+0h (Injection 2)	Injection 2
25	+2h (Injection 2)	
26	+4h (Injection 2)	
27	+6h (Injection 2)	
28	+8h (Injection 2)	
29	+10h (Injection 2)	
30	+12h (Injection 2)	
31	+14h (Injection 2)	
33	-2h (Pumping 2)	Pumping 2
34	+0h (Pumping 2)	
35	+2h (Pumping 2)	
36	+4h (Pumping 2)	
37	+6h (Pumping 2)	

Table 2. Models' subdivision in phases and time steps.

Where the highlighted time steps are those used also as background for the successive phase. The following paragraphs will show and discuss the results obtained from the 2D ERT acquisitions. Firstly, the background models will be interpreted and shown. Then, the background error will be estimated and then the percentage change models will be described and discussed.

4.2.1.1 Image quality assessment (DOI and Sensitivity results)

Before showing the results, the accuracy of them has to be discussed and verified. For the 2D inverted models the Depth Of Investigation (DOI) method (Oldenburg and Li 1999) has been

used. Briefly, this method consists in performing two inversions with two difference reference models. They are respectively one tenth and ten times the average resistivity values of the model. Therefore, for each cell located at position (x,z), the DOI index is computed according to the following equation:

$$DOI(x,z) = \frac{m_1(x,z) - m_2(x,z)}{m_{REF1} - m_{REF2}} \quad (4.1)$$

Where m_1 and m_2 are the resistivity values of the cell located in (x,z) position of the subsurface section of the inverted model 1 and 2 respectively, m_{REF1} and m_{REF2} are the resistivity of the reference model 1 and 2 respectively (i.e. one tenth and ten times the average resistivity values, respectively). Finally, the DOI index will be low and close to 0 in those areas where the resistivity values are well constrained by the data. On the contrary, in those areas where the index is close to 1, the resistivity values have been solved by the model reference value since there were no data information in their vicinity.

In this study, there have been evaluated the DOI models for the inverted 2D models. For the sake of simplicity, just some of them are shown in Figure A6 in Annex. The depth of these models is almost 2 times the maximum median depth of investigation of the inverted models. To better appreciate results, the edge of the pseudo-section (dashed grey line) has been also represented and, as suggested by Oldenburg and Li (1999), the cut-off line at 0.1 (solid red line).

In general, DOI results have not shown particular anomalies. Considering the area which fall within the pseudo-section, all the DOI models have normally values below the cut-off value. There is also a common area where DOI values are above the cut-off value and should not be considered reliable. As expected, such area is the deepest part of the pseudo-section and is usually located at a depth below 8 m. Furthermore, there are sometimes present some spots where the DOI index can exceed the cut-off value of 0.1. However, they are not considered relevant since they are caused by local high resistivity regions (Loke 2016a).

Another method used for ensuring the quality of the results obtained is the cumulative absolute sensitivity matrix. It is simply obtained by the product between the transposed Jacobian matrix and the Jacobian matrix itself. The cumulative sensitivity value is defined as the amount of information of the resistivity of a model block contained in the measured dataset (Loke 2016a). In other words, the sensitivity value shows how a model cell is “covered” by the data (Caterina et al. 2013). Therefore, high sensitivity values mean that a variation of the parameter will

influence strongly the data, i.e. the model resistivity value is more reliable. Even though is a rough estimation of the resolution of the model, it is still a simple and good alternative to other methods as DOI index.

For the sake of simplicity, it is shown just one set of sensitivity results in this Thesis (Figure A7 in Annex). Globally the sensitivity results confirm the expectations, and no particular results are a matter of discussion. Note that in zones where negative changes occur, the sensitivity pattern is no longer "stratified", but it tends to have higher sensitivity values.

4.2.1.2 Background models interpretation

The first inverted models to analyse are the background ones of all profiles. Figure 15 shows the background resistivity models, one per profile. Such results correspond to the time step 5 (i.e. 5 h before the beginning of Injection 1), and they have been interpreted and compared with the available borehole logs. In particular, only profiles 3 and 4 have been compared with logs of "Pz17" and "Pz13" respectively, since they are the only profiles close to the available borehole logs.

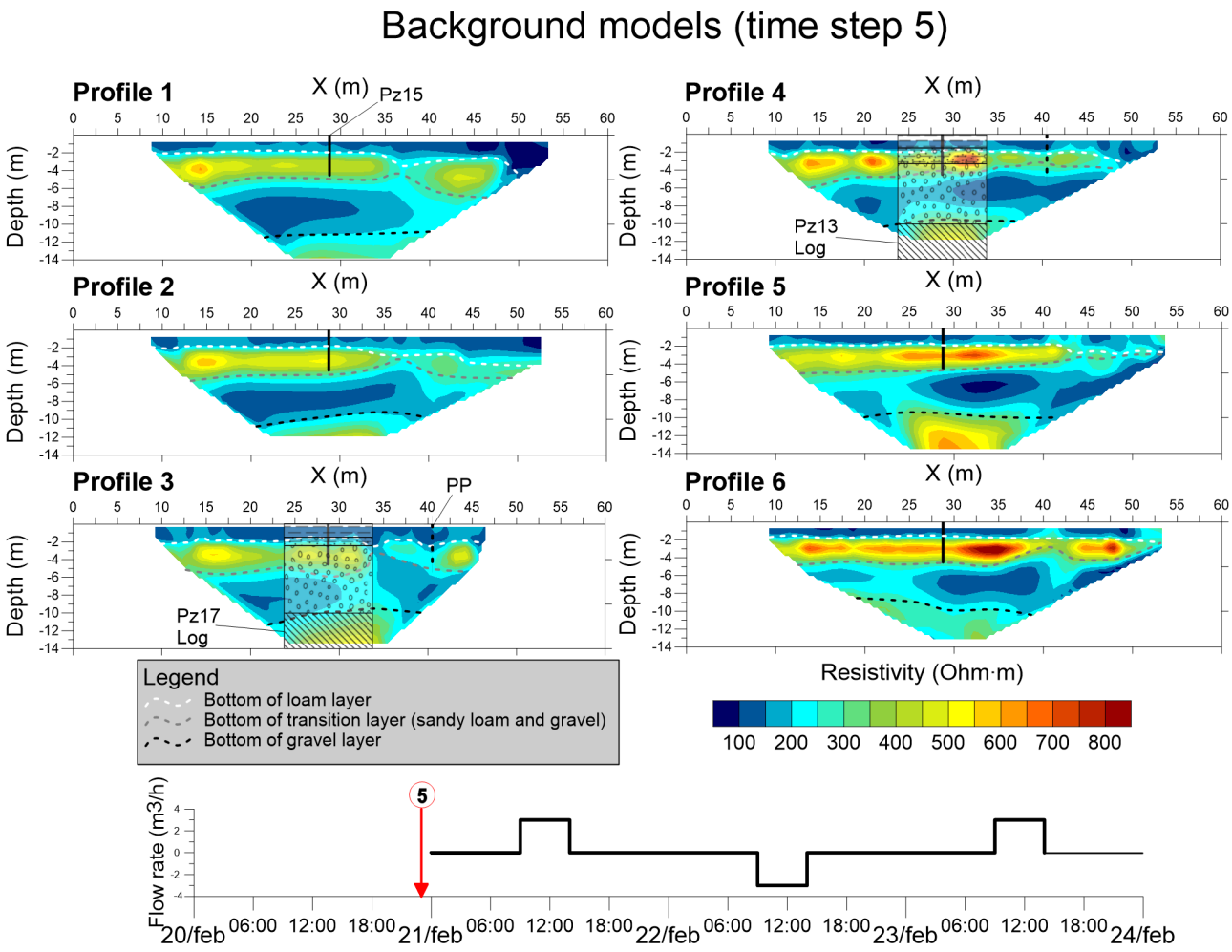

Figure 15. Interpreted background 2D resistivity models (at time step 5).

In the Figure 15, the black vertical line present in the resistivity models represent the piezometers' axis. The bottom of this line corresponds to the depth of injection and withdrawal (i.e. 4.5 m depth). Therefore, overlapping the borehole logs of "Pz17" and "Pz13" in the middle of the piezometers' axis, a direct comparison between the resistivity models of profiles 3 and 4 with the logs results is possible. Once the interpretation of profiles 3 and 4 is done, the remaining profiles can be interpreted similarly. The three dashed lines (white, grey and black) show the interpreted interfaces between different subsurface formations. Of course, since they are based on the resistivity values and logs, they are not accurate but they just give an approximate idea of these limits.

From the interpretation of background models, it is evident that all the four layers are generally in agreement with the resistivity values. Despite that, the interface between the sandy loam (or loamy gravel) and the gravel layer has resulted difficult to define. As a matter of fact, differently to the bottom, the top of the gravel layer is normally not coarse and tends to be sandy and similar to the loamy sand. Therefore, the second layer identified in the background

models is an actually transition layer of the sandy loam and the top of the gravel layer, rather than the only sandy loam layer.

The first layer seems to be low resistive with values up to 150 Ohm·m. The second layer (i.e. the transition layer between sandy loam and the top of gravel layer) is quite resistive with values ranging between 400 Ohm·m and 850 Ohm·m. Instead, the gravel layer has low resistivity values ranging from 100 Ohm·m to 250 Ohm·m, due to the presence of coarser grains at the bottom of the stratum. Finally, the bedrock has high values ranging from 450 Ohm·m to 650 Ohm·m with uncertain limits due to the lower resolution and sensitivity.

As far as the similarities, the six profiles do not seem very similar, although they cover an area 15 m wide. In particular, the transition layer assumes different ranges of resistivity. As a matter of fact, such layer is less resistive in profiles 1, 2 and 3 while is highly resistive in the other three profiles. Also, still the three first profiles have some interruptions in the transition layer, as if it disappears in some zones. This anomaly might be confirmed by the borehole logs of "Pz16" and "Pz17" which have a second layer thinner than the logs close to Profile 4.

Finally, as mentioned in Chapter 3 the aquifer present in the site is usually unconfined, but it can have some semi-confining zones depending on the loam layer. Thus, it might be concluded that the area covered by profiles 4, 5 and 6 is more confined than the area covered by profiles 1, 2, 3.

4.2.1.3 Estimation of the background error

Before analysing the percentage change in all the time steps, a background error analysis is needed. Consequently, the two background acquisitions before Injection 1 (i.e. time steps 3 and 5) have been inverted together using the time-lapse mode implemented in RES2DINV. Successively, from the two models a resistivity percentage change model has been obtained for each profile. Then, such models have been used to estimate the background error, that should be taken into account in the analysis and representation of the other time-lapse models involving actual resistivity changes in the subsurface.

The Figure A8 in Annex shows the six models obtained for the estimation of the background error. Obviously, between the two acquisitions there should not be high resistivity changes, or at least in theory. Despite that, in the obtained models there are few resistivity changes. Such changes range generally from -2% to 2%, with most values ranging between -0.5% and 0.5%. Only Profile 3 has a little spot (corresponding to an area of 0.5 m^2) where the resistivity change

has values between 2% and 2.5%. To be conservative, such spot has been taken into account in the background error analysis. Finally, from the considerations made it has been decided to consider a background error between -2% and 3% for the next results.

4.2.1.4 2D Resistivity results of Injection 1

Once the background error has been determined, the remaining resistivity models can be treated. The inverted models are divided according the four phases carried out during the cycle experiment. All models are represented in terms of resistivity percentage changes, where the values have been computed according to:

$$\Delta\rho_i = \frac{\rho_i - \rho_1}{\rho_1} \tag{4.2}$$

Where $\Delta\rho_i$ is the resistivity percentage change of the *i-th* time step; ρ_i is the resistivity value of the *i-th* time step; and ρ_1 is the resistivity value of the first time step (i.e. the background time step). Therefore, for each inverted block and for each time-lapse model, the resistivity percentage change values are computed as mentioned.

The percentage scale used to represent the subsurface section is fixed for all the models of all the phases. The idea was indeed to better compare the resistivity changes between all the different models. Particular attention has been paid to the background error previously described. Indeed, as the results shown (Figures 16 and 17), a dotted pattern and a grey line have been used to highlight those percentage values between -2% and +3%.

Finally, in all models it is represented the well "Pz15" (its depth has been limited to the injection/pumping depth), that in Profile 1, 2, 5 and 6 it might be considered the monitoring boreholes' axis. Moreover, the well "PP" is represented just in those Profile 3 and 4 models of the injection phases to avoid possible misunderstanding of the results.

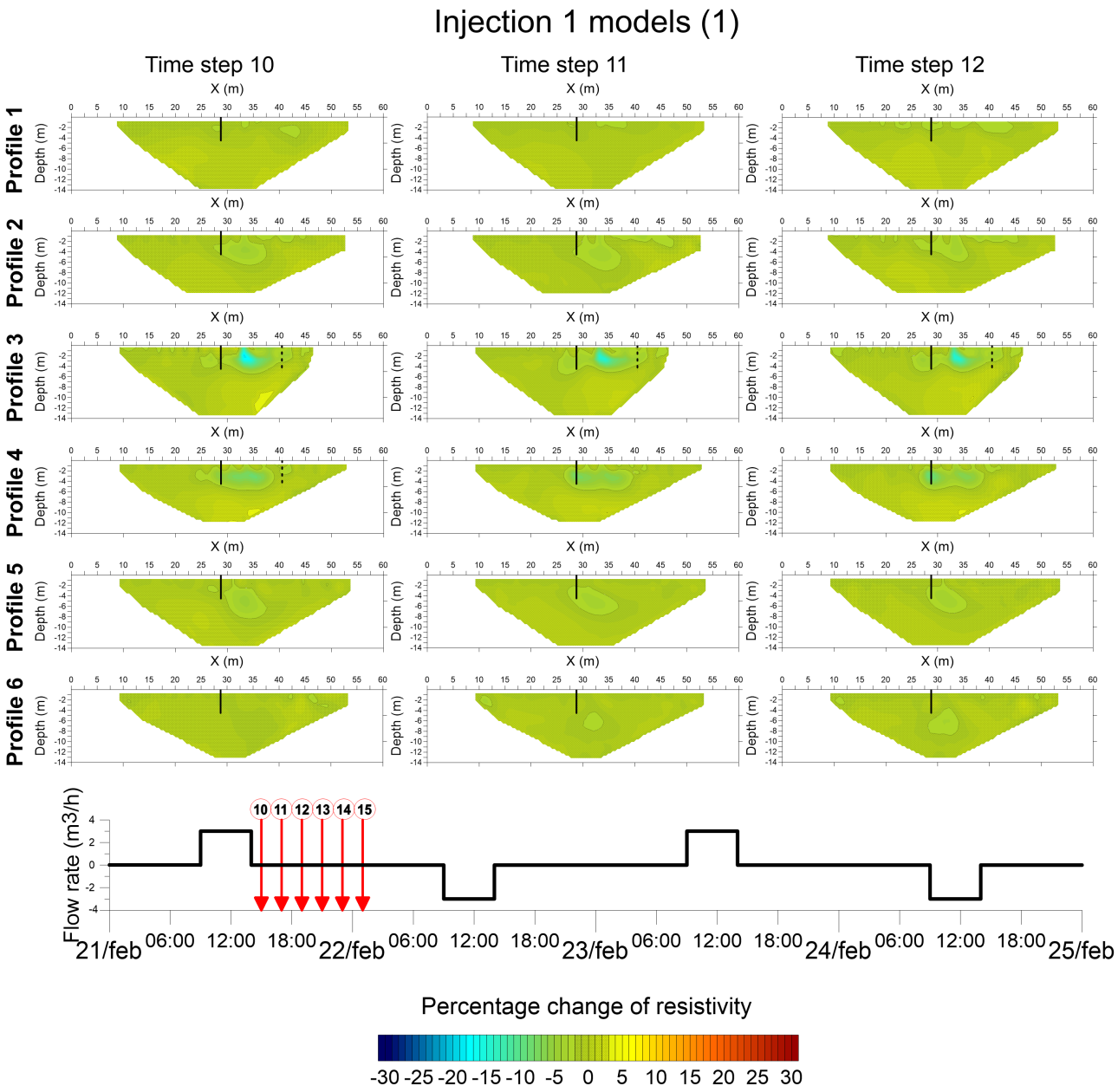

Figure 16. 2D Time-lapse resistivity models of Injection 1 (part 1).

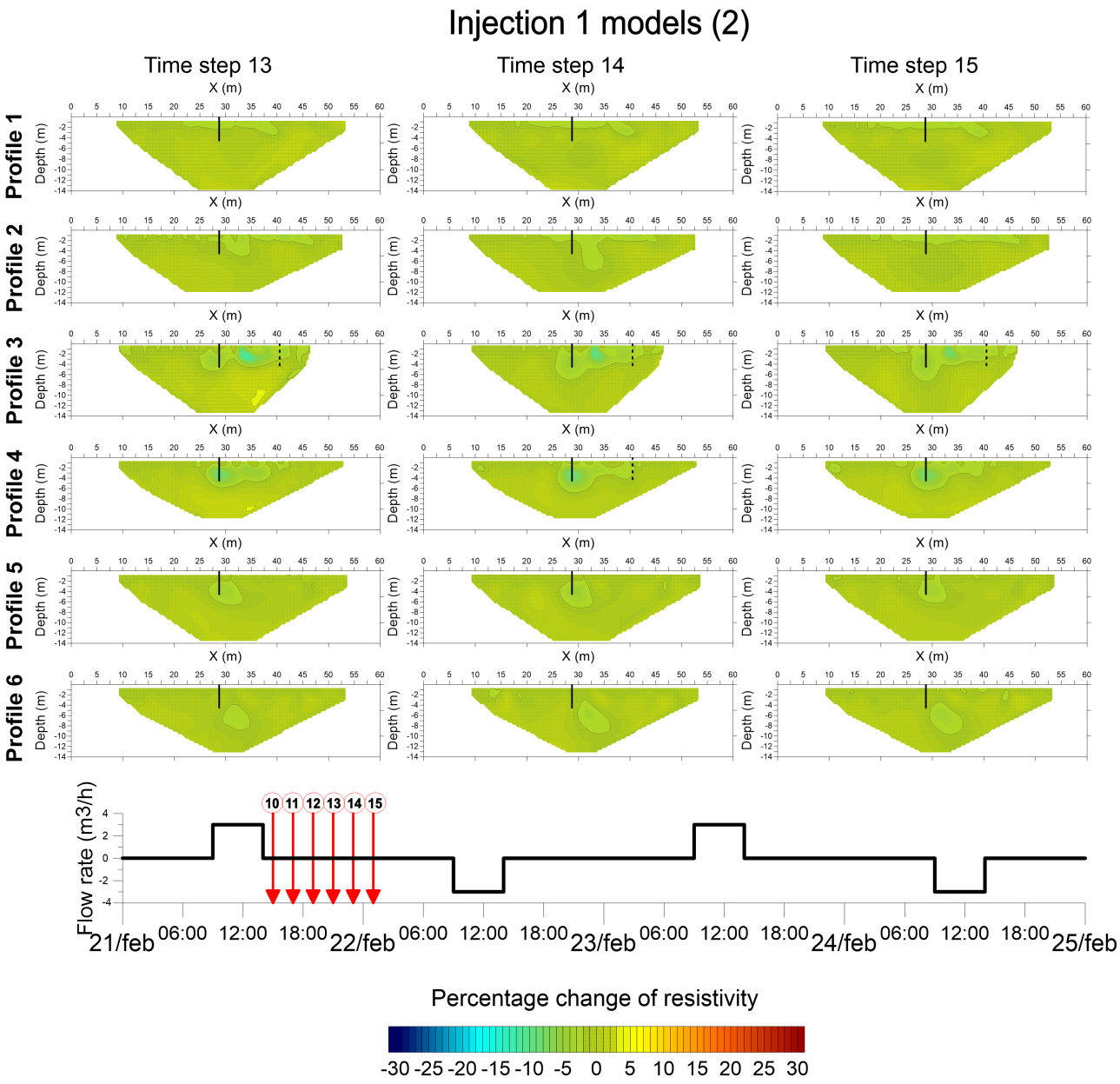

Figure 17. 2D Time-lapse resistivity models of Injection 1 (part 2).

The resulting resistivity time-lapse models of the Injection 1 phase are shown in Figure 16 and 17. As expected, the higher negative resistivity changes (i.e. up to -20%) are present in the two closest profiles, namely Profile 3 and 4. On the other hand, the other profiles have lower changes with values that can reach a minimum of -5%.

Profile 1 results show very poor changes. Indeed, it is also quite expected since it is the farthest profile along with Profile 6. The only changes present can rarely go lower than -3% and do not seem to be related to the hot water injection.

In Profile 6, instead, few resistivity changes can be appreciated, although delayed respect the other profiles. The minimum value is right greater than -3.5% and is located in the last time

step, which confirms again the delayed peak in this profile. Thus, such changes are definitely related to Injection 1, because of both the delay and the plume-shaped negative resistivity spot.

Going towards the inner zone of the grid, Profile 2 and 5 have obtained similar results. In both profiles the plume has been detected with values up to -5%. However, the main difference is the prolonged presence of the plume during the monitored phase. As a matter of fact, the plume of Profile 2 tends to disappear in the three last time steps. On the other hand, in Profile 5 it tends to be constant for all the time steps.

Note that this confirms somehow what mentioned in the CTD analysis. Along the direction of "Pz13", hence the zone covered by Profiles 1 and 2, the porosity is probably higher than the opposite area (i.e. the area of "Pz17", Profile 5 and 6). This leads to have high peak of temperatures during the injection but lower heat retaining capacity.

Finally, the two inner profiles have quite different results. Profile 3 reaches lower values (up to 20%) than Profile 4, with the lower peak at the first time step. Then, the plume seems to be irregular and shifted 7 m from the injection well and towards NE. However, in both case the plume is located exactly between the two wells "Pz15" and "PP". Therefore, the hot water plume might be influenced by the pumping performed in "PP" that somehow flattens and attracts the hot water volume towards NE.

Even in this case, although the plume in Profile 3 reached better peak values, it is not as much constant as the one in Profile 4. In the case of Profile 4, indeed, the plume has higher values (up to 8.5%) but tends to be constant during the time. It is also large and a bit dislocated towards NE as in Profile 3 case. However, in time steps from 13 to 15, it tends to be repositioned around the injection point.

4.2.1.5 2D Resistivity results of Pumping 1

The resistivity models of Pumping 1 phase are shown in Figure 18 and 19. Comparing the previous phase with this, the resistivity changes seem to be less marked.

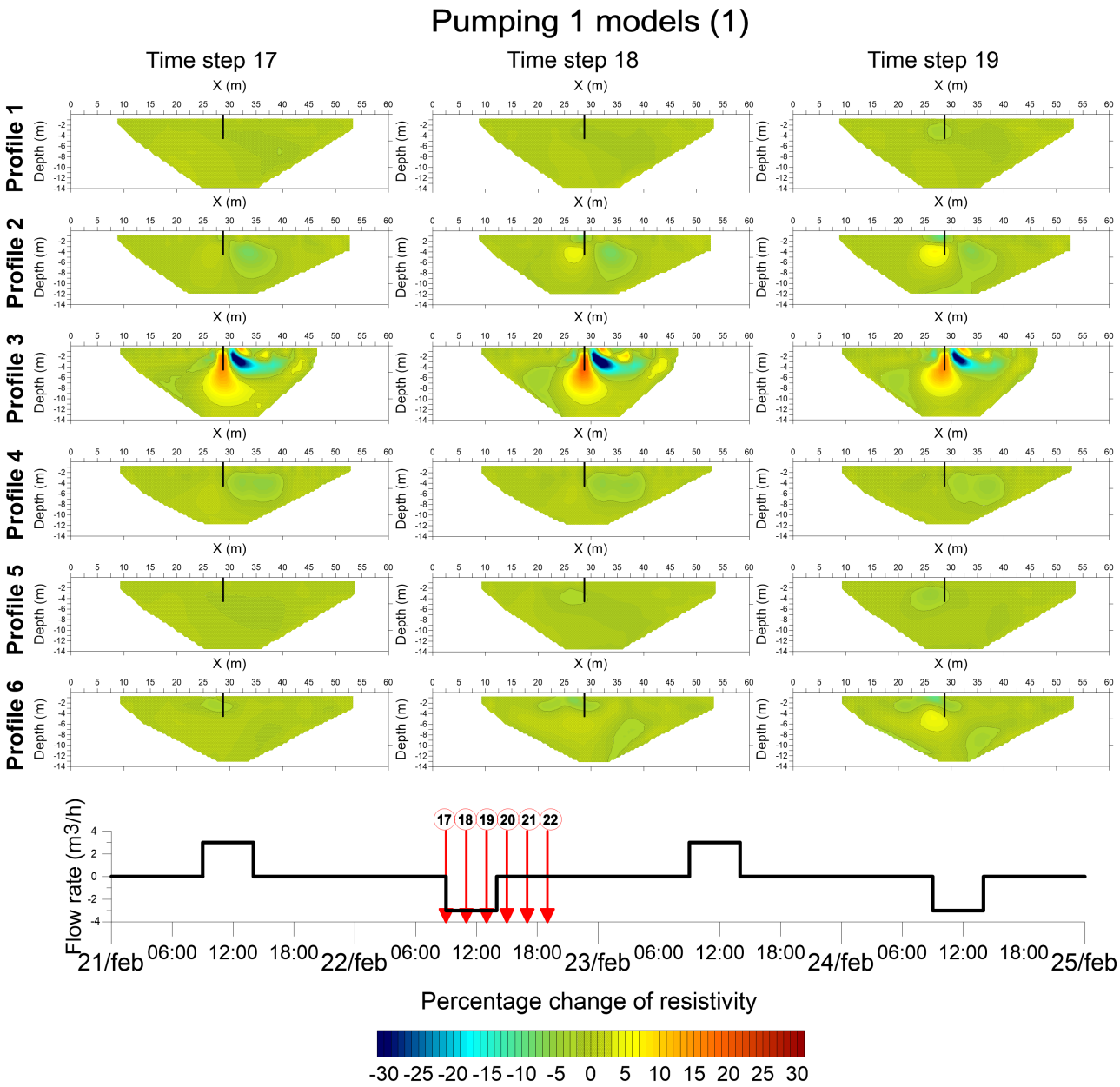

Figure 18. 2D Time-lapse resistivity models of Pumping 1 (part 1)

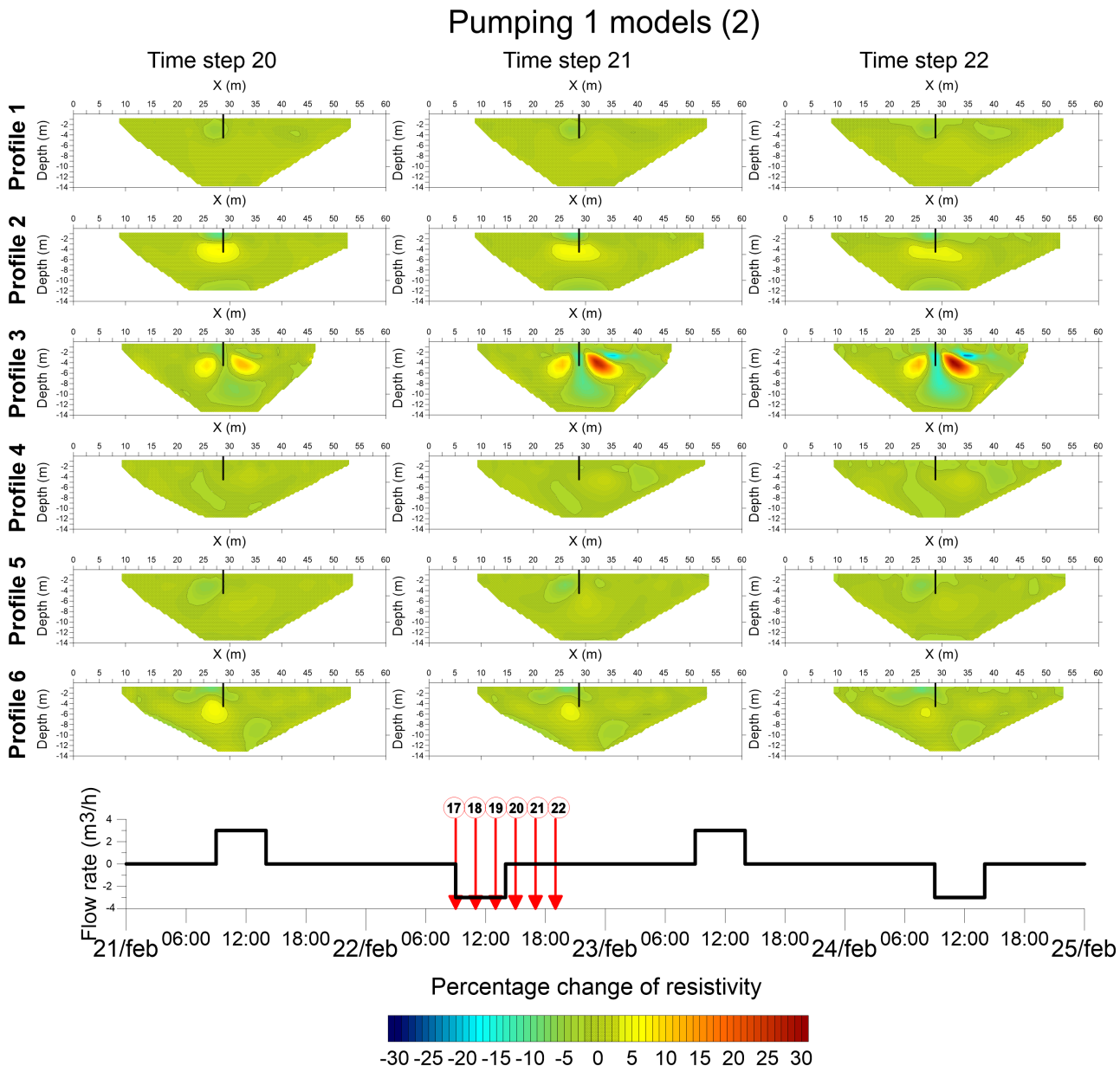

Figure 19. 2D Time-lapse resistivity models of Pumping 1 (part 2)

As in the previous phase, Profile 1 has almost no relevant changes. However, in this case a light plume (with values up to 5.5%) appears from the third time step on. This delayed plume might be the sign of the possible recall of warm water caused by the recent pumping action.

On the other side of the grid, in Profile 6, the plume is different than the previous one. In this case the plume present is not due to negative changes, but positive. This behaviour is due to the inversion setting used. In particular, the resistivity changes of Pumping 1 models are referred to the last acquisition of the Injection 1 (i.e. the time step 15). Then, looking at this model, it is evident that the negative resistivity plume is still present. Therefore, the reason of the positive changes in Profile 6 of Pumping 1 phase is that from the 19th time step the groundwater started cooling. Such cooling phase might be caused by the cold water recalled by

the stop of the pumping phase. However, from the time step 20 on, the plume becomes smaller and warm temperature come back. Finally, there is also a little negative spot on the top of the subsurface. For this spot, no clear explanations can be done. A hypothesis might be that this area is actually warmer than before and due to the low density of the hot water, this hot water volume tends to float over the cold one for buoyancy. However, this implies that the subsurface is completely saturated up to the ground surface and that for capillarity the hot water is able to "climb" up to the surface. Then, considering that during the 4 days of experiment the weather was quite rainy and the first layer is quite fine (loam formation), this hypothesis might be considered reliable.

As far as Profile 2, both negative and positive changes appear, with extreme values that can reach -8% and 7% respectively. Initially, there is just a negative resistivity plume, but from the second time step of this phase a positive plume appears. From that time step on, the negative plume becomes smaller, while the positive becomes bigger for then reduce its shape in the last time steps. The negative plume should be related to the heat released by the rock or by the warm water recalled by the pumping phase. Instead, no clear reasons have been found for the positive plume. However, it might be representing a subsurface area cooled by cold water still recalled by the pumping operation. In addition to these to plumes, there is also a negative change located in some time steps, at the bottom of the subsurface section. Of course, since the DOI index is above the cut-off value and the sensitivity is low, such change is not reliable and should not be related to the pumping phase. Finally, the same explanations done for Profile 6 can be applied to the negative spot located at the top of the subsurface (similar to the one encountered in Profile 6), close to the boreholes' axis.

Concerning Profile 5, the resistivity changes are pretty clear. The minimum value reaches -7.5% and the plume appears later than the one of Profile 2. As a matter of fact, the plume appears in time step 18, grows until it reaches its peak at time step 21 and then becomes smaller in the last time step. Comparing Profile 2 and 5 results of Pumping 1, the same differences found in the previous phase have been found. Therefore, the plume in Profile 2 has a shorter duration but lower peak values. On the other hand, in Profile 5 it lasts more but has a smaller shape with higher values.

Profile 4 presents good and plausible results. The plume is big and present from the fist time step to the third, with lowest value equal to -5.5%. Looking at the last model of Injection 1, it seems that temperatures increase further in the first three time steps due to a water recall

caused by the pumping operation. The light changes present from time step 20 on, are not considered relevant.

Finally, the last profile which needs to be discussed is Profile 3. Compared with the other profiles, it is surely the most problematic. In the three first time steps (i.e. time steps 17, 18 and 19) there are two big plumes, one with positive changes and the other with negative with extreme values that can reach 19% and -40% respectively. Then, from time step 20 on, they both disappear but they are replaced by two new big plumes similar to the previous ones but with inverted changes. So far, the reasons of such changes are not particularly clear, although they are related to the end of the pumping phase. Nevertheless, there might be an explanation. In the three first time steps, the subsurface is still affected by the pumping effects, where the central positive plume represents the colder pumped water, while the negative plume represent the hot water which is still gathered by the withdrawal and floats for different density at the NE side of the well. Then, in time step 20 the effects of the pumping phase stop and the subsurface try to reach the equilibrium. Indeed, the zone right below the well is warmed by the rock and the water that was on the NE side of the well. Instead, the two zones at the sides of the well are cooled by the cold water which was "almost pumped". It should be noted that the shape and also the magnitude of the changes might not be accurate. The former because the DOI cut-off value is high and the quality of the model below 8 m starts to becomes worse. The latter because sometimes the inversion procedure tends to enlarge and thicken high or low resistivity spots from one iteration to another. Despite that, this hypothesis might be better discussed and verified with the temperature conversion results.

4.2.1.6 2D Resistivity results of Injection 2

As usual, the results of all models concerning Injection 2 phase are shown in Figure 20, 21 and 22. First of all, comparing the two injections, it seems that in Injection 2 the negative changes are thicker than the first one. As shown before, even the CTD results have led to the same conclusion, so such results confirm what the direct measurements have already detected.

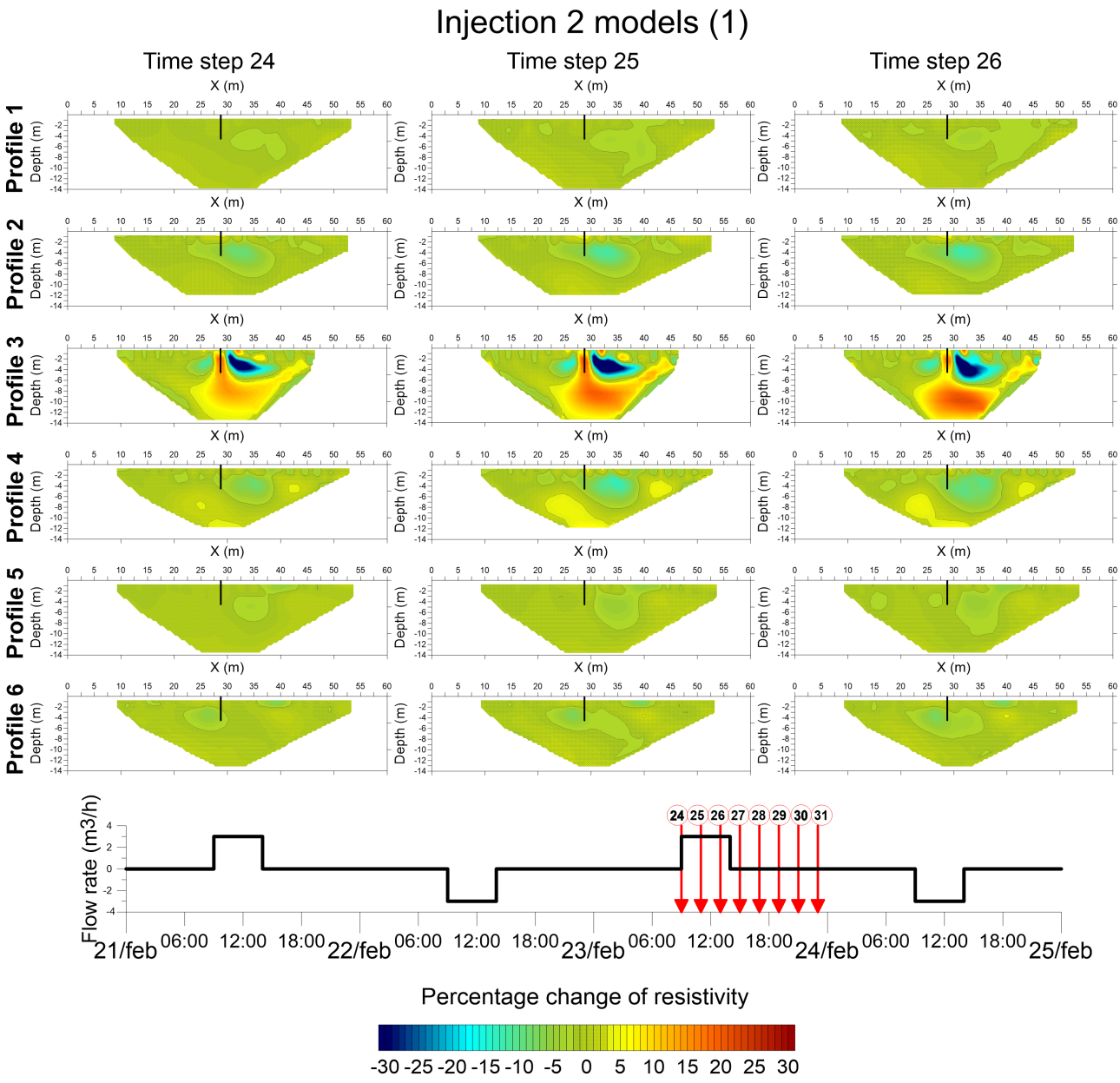

Figure 20. 2D Time-lapse resistivity models of Injection 2 (part 1)

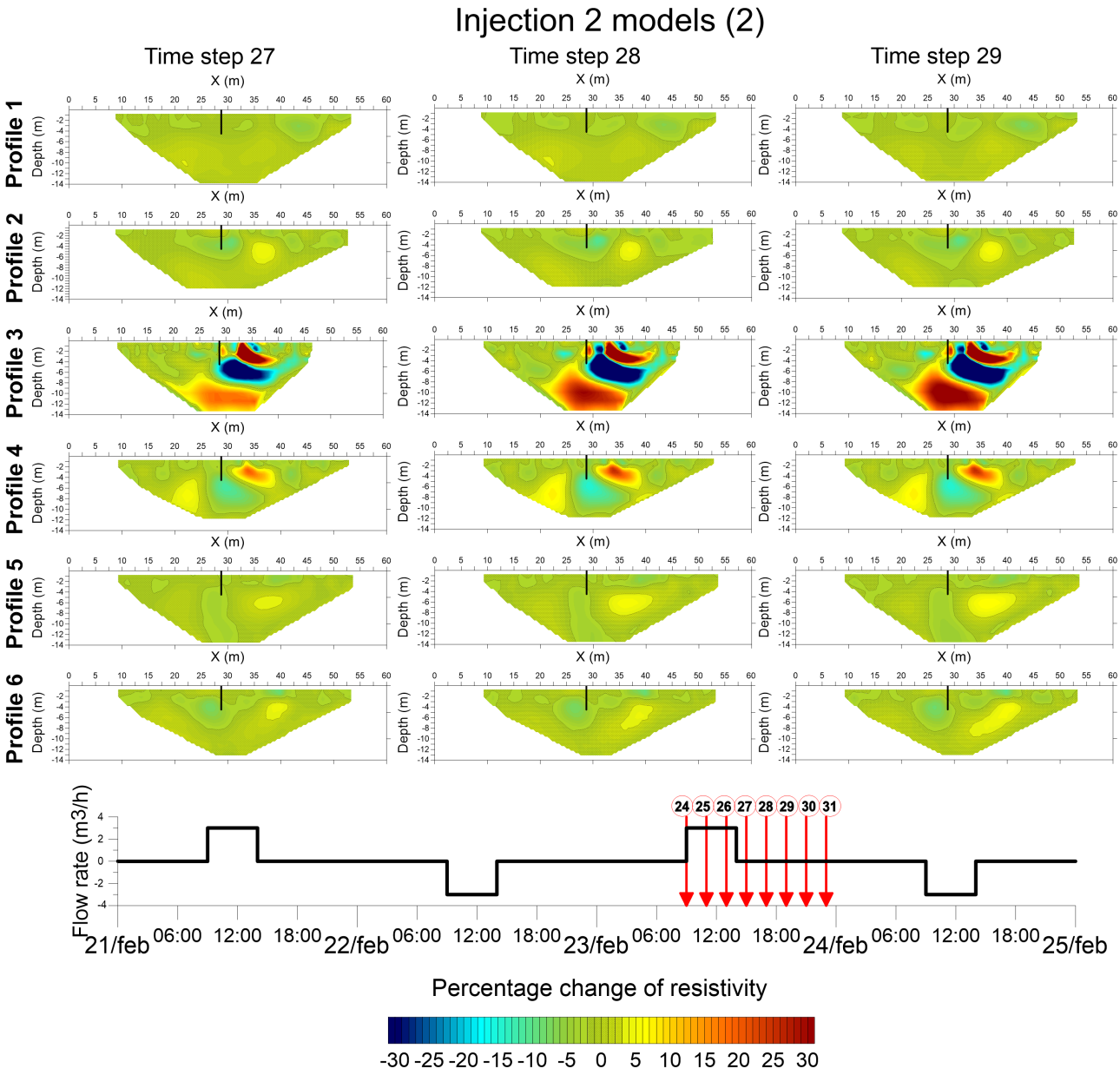

Figure 21. 2D Time-lapse resistivity models of Injection 2 (part 2)

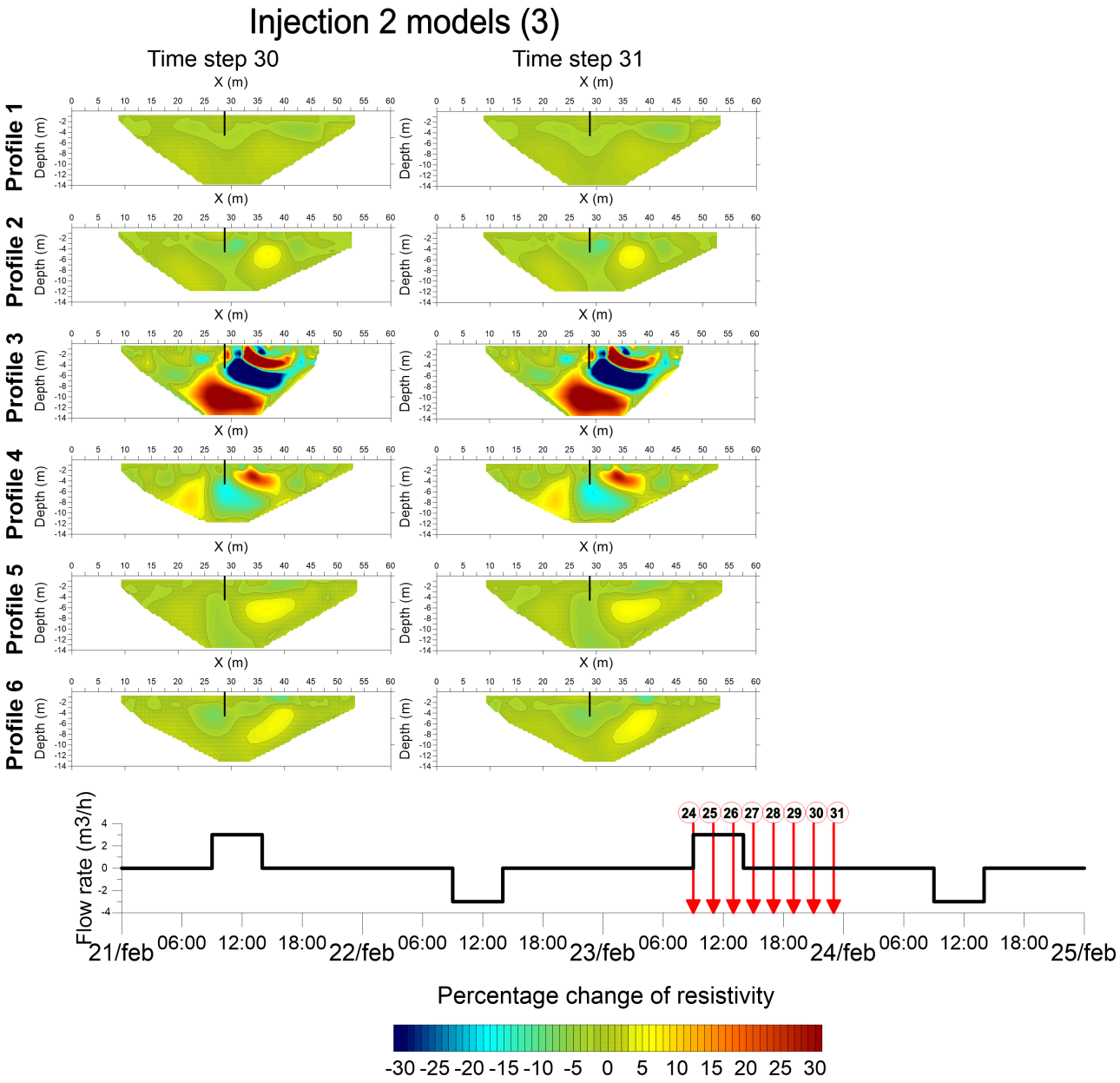

Figure 22. 2D Time-lapse resistivity models of Injection 2 (part 3)

Comparing all profiles results, Profile 1 is the one which has less resistivity changes than the others. Generally, in all time steps there is a plume with very light negative changes located in the vicinity of the borehole axis which might be related to the injection phase. There are actually other negative spots, but is not clear if they are caused or not to the injection phase.

Differently, Profile 6 presents a constant negative plume with values even lower than -8% in all time steps. This is surely related to the injection phase that influences this profile with delay. Apart from negative changes, at time step 27 seems to appear a positive plume on the NE side of the boreholes' axis. The reason why it appears is not clear.

In Profile 2, the negative plume is pretty clear in all time steps. It grows until time step 26, where the lowest value can reach -12.5%. Then, from time step 27 on the plume becomes smaller and the same positive spot of Profile 6 appears.

On the other side, Profile 5 still has a negative plume as expected, but it is unusually light. Its values can reach a minimum of -4.5%. In addition, not only in time step 27 the positive spot appears but also the shape of the negative plume starts distorting. However, the distorted shape of the plume should not be considered, since it is probably affected by the poor quality of the area below 8 m depth.

In the inner part of the grid, Profile 4 shows a big and well defined negative plume across all its time steps. In the first three time steps has negative changes that can reach -13.5%. After, in time step 27, a positive change appears on the NE side of the well. From that time step on, both the negative and the positive plumes become thicker, reaching extreme values of -17% and 28% respectively.

Finally, the most problematic profile even in this phase is Profile 3. From time step 24 to 26, there are two negative plumes at the sides of the well and one positive plume at the middle of the well with extreme values of -43% and 19% respectively. Since these time steps fall within the injection phase time interval, the explanation of such contrasting results can be derived from that. The two negative plumes are dislocated laterally to the well, and this means that the hot water injected superficially tends to widespread laterally. Instead, the central positive plume might be caused by the injection disequilibrium.

On the other hand, from time step 27 to the final one, the big negative plume changes position and a new positive spot appears. The first has minimum values lower than 40%, the second has unexpected values even higher than 80%. Apart from the change of the shape of the negative plume, the appearance of the thick and superficial positive spot cannot be justified by the end of the injection process. Finally, there is a constant increment of resistivity in the area below 8 m depth. As discussed before, this is clearly an artefact not reliable at all since the sensitivity and DOI is not acceptable. Furthermore, note that the time constrained inversion tends to produce models similar to each other and the deeper is the area the higher is the damping factor. Therefore, this confirms again what said, so probably the positive plume positioned below the well could actually have a different shape, maybe not deeper than 7-8 m.

To better understand the positive spot appeared in Profile 3 after the end of the injection, some controls have been carried out. They might be briefly listed and described as follow:

- Check the previous iterations of the models. The aim was to check if the spot has been exaggerated by the further iterations, but actually such spot was present also in the first iteration.
- Make sure that during the experiment nothing was poured in the ERT grid area. Indeed, it has been though that something with different conductivity like rainfall water or fuel from the boiler infiltrated in the subsurface creating such positive spot. However, the hypothesis of the fuel leak has been discarded straight away, since the volume of the spot is too large and no leakage has been found during the operations. The possibility of the rainfall is not clear as well. Indeed, in almost all days there were alternating rain events, and it is surprising that these effects are noticed just after the end of Injection 2.
- Check the sensitivity of the array used. In this case, 3 points have been selected from the big positive spot. Looking at their configuration array, for each point, it has been checked that the sensitivity of the configuration array in the location was not high and positive. If it was so, the acquisition would have exaggerated the positive resistivity change. However, it resulted that they had a low positive sensitivity.
- Check the measured resistance values. At the 3 points analysed before, 3 further point at different locations have been considered. In the 3 added points there is the deepest dipole-dipole acquired point, the deepest acquired point (which is a gradient acquired point) and a point which had always almost no percentage change in the models. The idea was to understand if the percentage changes of the models were caused by the inversion process or not. It resulted that the resistance variations are similar to the percentage changes and the inversion process is not responsible of the high resistivity spot.
- Check the standard deviation from repetition measurements of the resistance values. The same 6 point analysed before have been considered again. In this case, the standard deviation variations have been checked to understand if the acquired resistance values had unusual or high values. It came out that the 3 points related to the high resistivity spot had standard deviation values very low and close to 0%. Only the deepest point had alternating variations due to the alternation of reciprocal and normal acquisitions with values up to 2.5%. However, since it is the deepest point such high values are pretty obvious.
- Check the DOI index. Finally, the DOI index distribution has been checked for all the time steps of Profile 3 but no strange results came out.

As conclusion of the results obtained after these controls, the origin of the high resistivity spot is still not clear. As a matter of fact, it has not been caused by neither the acquisition, or the inversion or external origins. Therefore, it seems that something geologically happened in the subsurface that caused a sharp change of high resistivity (or low conductivity). Note that the problem of the high resistivity spot of Profile 3 might be extended to the other profiles. Indeed, even if with low magnitude, such high resistivity spot has always appeared in time step 27, such as 1h after the end of the Injection 2 process.

4.2.1.7 2D Resistivity results of Pumping 2

The results of the last monitored phase are shown in Figure 23 and 24. Above all, from a first comparison between the two pumping process, it comes out that the percentage changes are not particularly similar. This is however caused by the representation. Indeed, comparing the two background models used in the two phases (i.e. time step 15 for Pumping 1 and time step 31 for Pumping 2), it is pretty evident that they have very different resistivity values. Therefore, the different results between the two pumping phases are justified.

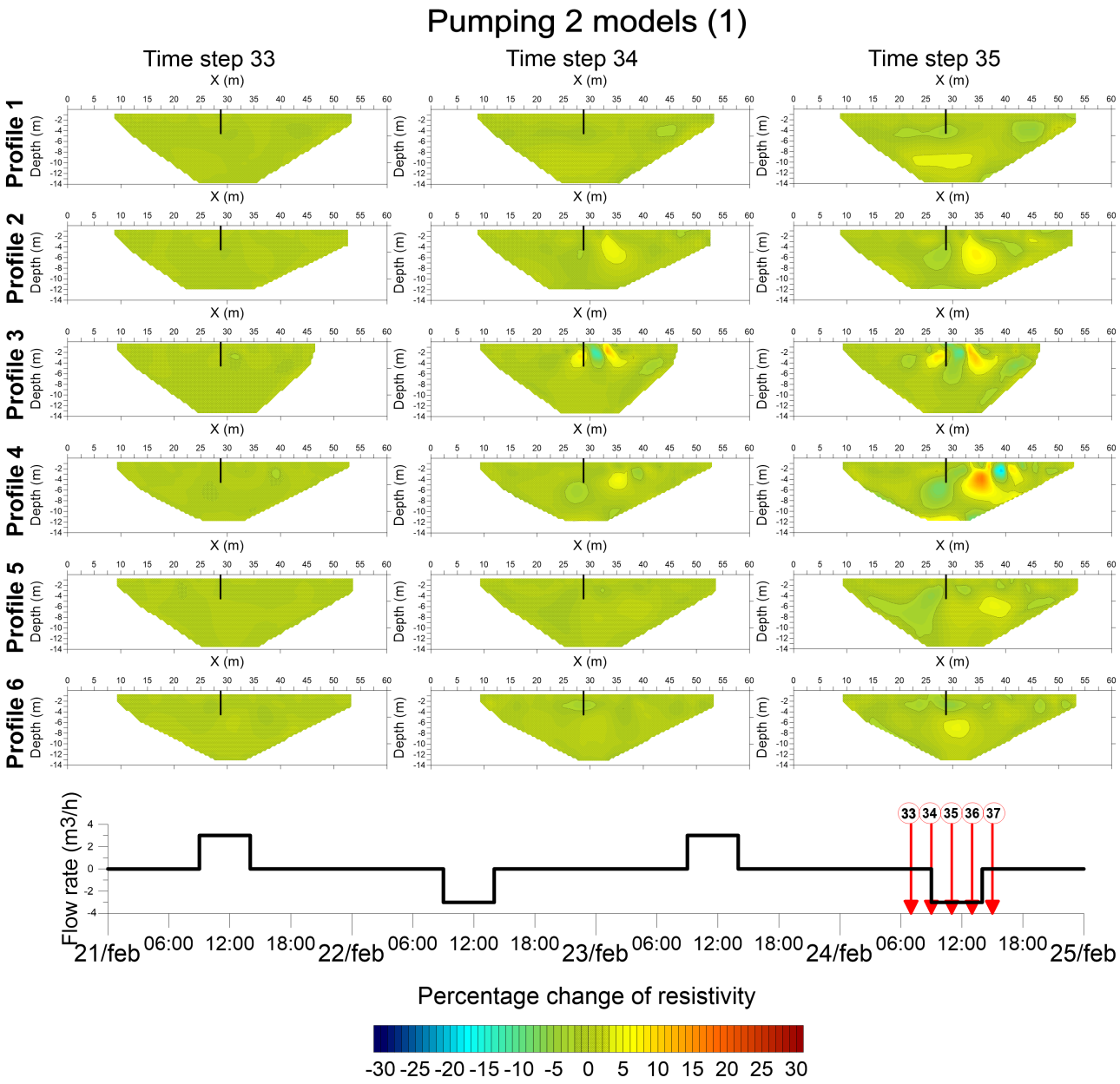

Figure 23. 2D Time-lapse resistivity models of Pumping 2 (part 1)

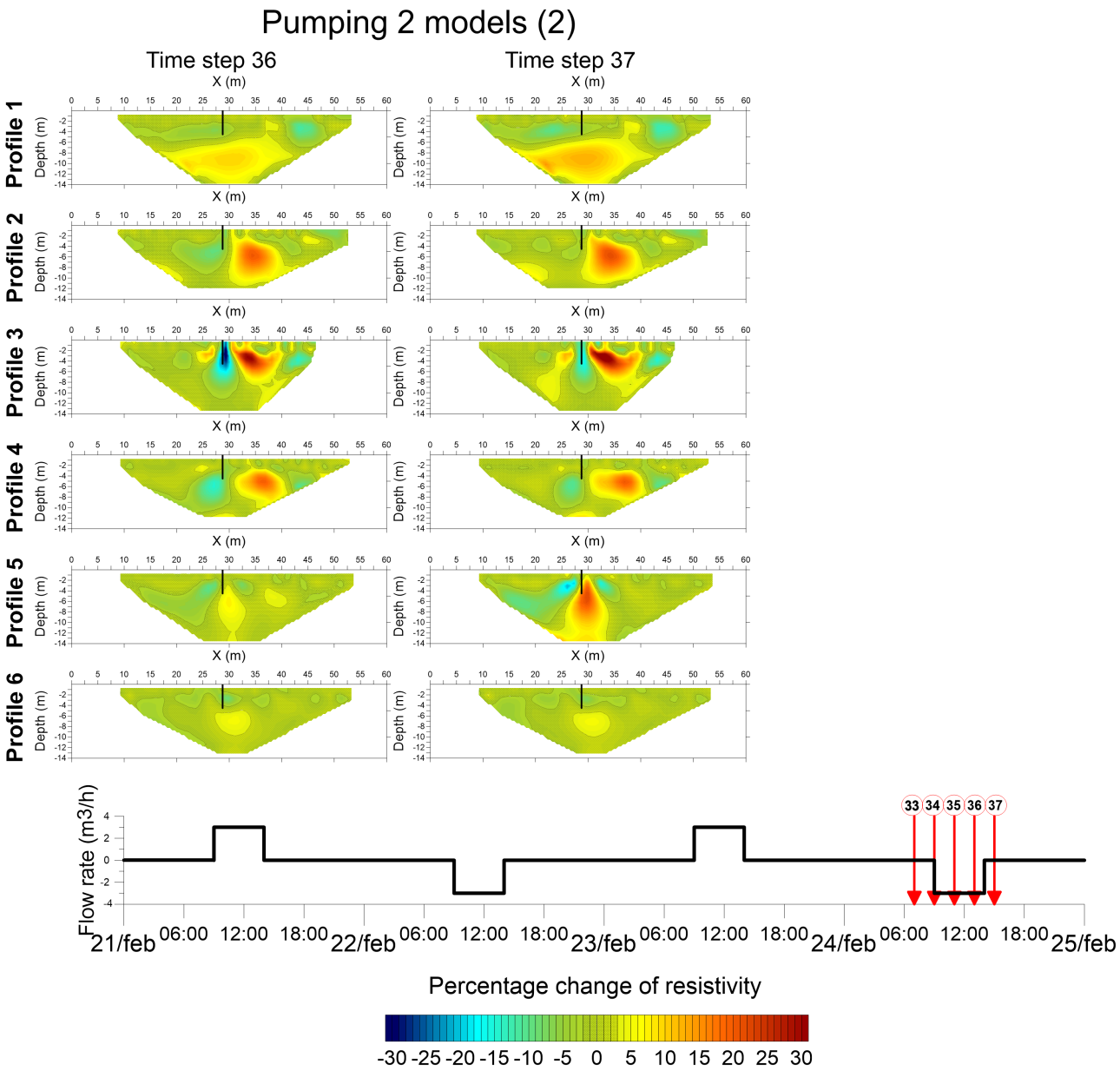

Figure 24. 2D Time-lapse resistivity models of Pumping 2 (part 2)

Starting with results of Profile 1, the resistivity changes in all time steps are very weak. The first time step has been taken 2h before the starting of the pumping phase, so it is expected that for all profiles no changes are present. In Profile 1, two resistivity changes start to appear in the third time step (i.e. time step 35), a negative spot and a positive one. From that time step on, they grow until reaching extreme values of -10% and 12% respectively. Note that the reliability of the positive plume is not as good as the negative plume for the classic reason mentioned in the previous discussions. However, these two plumes might be related to actual different temperatures of the water caused by the usual density effect.

On the other side, Profile 6 presents almost the same behaviour as Profile 1. Even in this case two plumes appear at time step 35, one negative and one positive. Differently from the first profile, they have lower changes with extreme values that reach -8% and 5% respectively.

As far as Profile 5 and 2 results, they are still similar to the close Profile 6. Again, negative and positive plumes appear at time step 35, and from that time on they grow. The only difference between these two profiles is that Profile 2 changes are thicker than Profile 5 ones and appear one time step before. But this difference is the same found also in the other phases.

Finally, the two inner profiles present similar results. Two main plumes, one negative close to the well and one positive at the NE side of the well, start to appear from the first moments of the pumping (i.e. time step 34). The highest and lowest resistivity changes are obviously present at the last time step before the end of the process, namely time step 36.

At this stage, since many changes have occurred, it is very difficult to motivate the results. However, it will be more clear in the temperature conversion paragraph where the temperature values will help to understand the monitoring results.

4.3 Temperature conversion

Once the resistivity models are obtained, the temperature conversion computation have been carried out. The aim of this conversion is to better use the resistivity results obtained from the ERT acquisition and inversion. Furthermore, in the previous paragraphs there have been found some difficulties to interpret the resistivity changes results. Instead, it will surely be easier to explain and understand the inverted resistivity results in terms of temperature values.

Therefore, in this paragraph the results previously shown will be transformed in terms of temperature values and better discussed. Of course, for the sake of simplicity, the already mentioned motivations will be just recalled, without going deep in the discussion.

4.3.1 Results and discussion

The temperature conversion procedure has been already described in the Paragraph 3.8. According to what explained before, the assumed initial temperature of the aquifer is 12.26°C for all profiles. In the representation of the temperature results, only positive temperature changes have been shown. Therefore, the temperature models will show just those temperatures with values higher than the initial value. Furthermore, in order to take into

account of the background error previously computed, the temperature increment linked to a negative resistivity change equal to -2% (background error) has been computed. Thus, the common scale used to represent the results goes from 13°C to 41°C. Note that the colour scale is not linear. Indeed, it is linear in the first 10°C (i.e. from 13°C to 23°C), with an interval of 1°C, while it is still linear but with an interval of 2°C from 23°C to 41°C. The reason why the colour scale is "dually" linear comes from the need to have a common scale for all the models. As it will be shown later, some of them have normally low temperatures, up to 23°C, while others have high temperatures, even higher than 41°C. Therefore, to highlight both ranges of temperatures this common way of representing the results has been found. Moreover, a white solid line will mark the limit between the two ranges, so that it will be easier to recognise whether is one range or the other. Finally, note that the same representation rules used in the 2D resistivity models for "PP" and "Pz15" wells are used.

4.3.1.1 Temperature conversion results of Injection 1

The temperature conversion results of Injection 1 are shown in Figure 25 and 26. In general, the first impression of the results is that temperatures are quite low and the injection phase has affected the aquifer temperatures just partially.

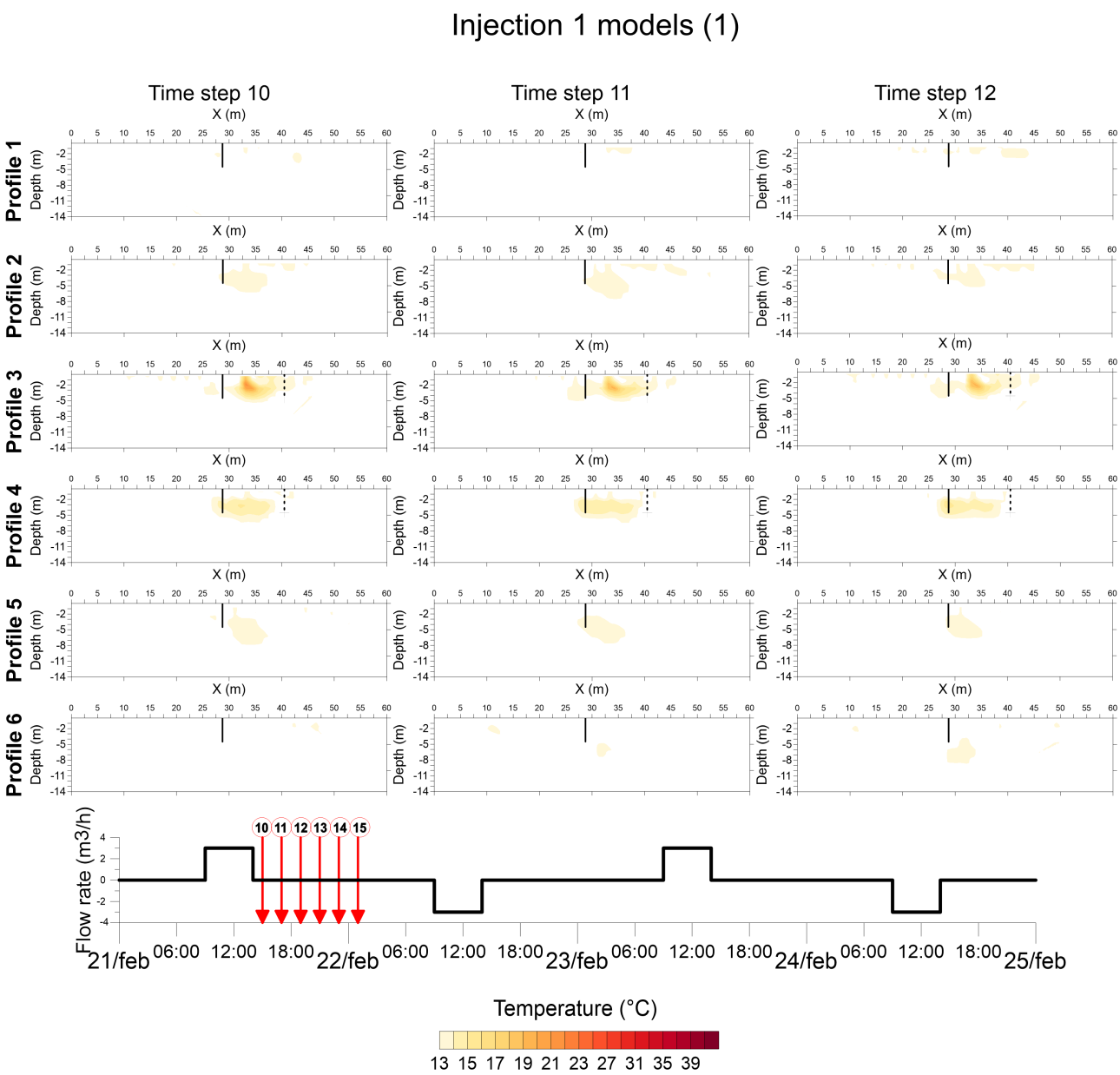

Figure 25. 2D Temperature conversion models of Injection 1 (part 1)

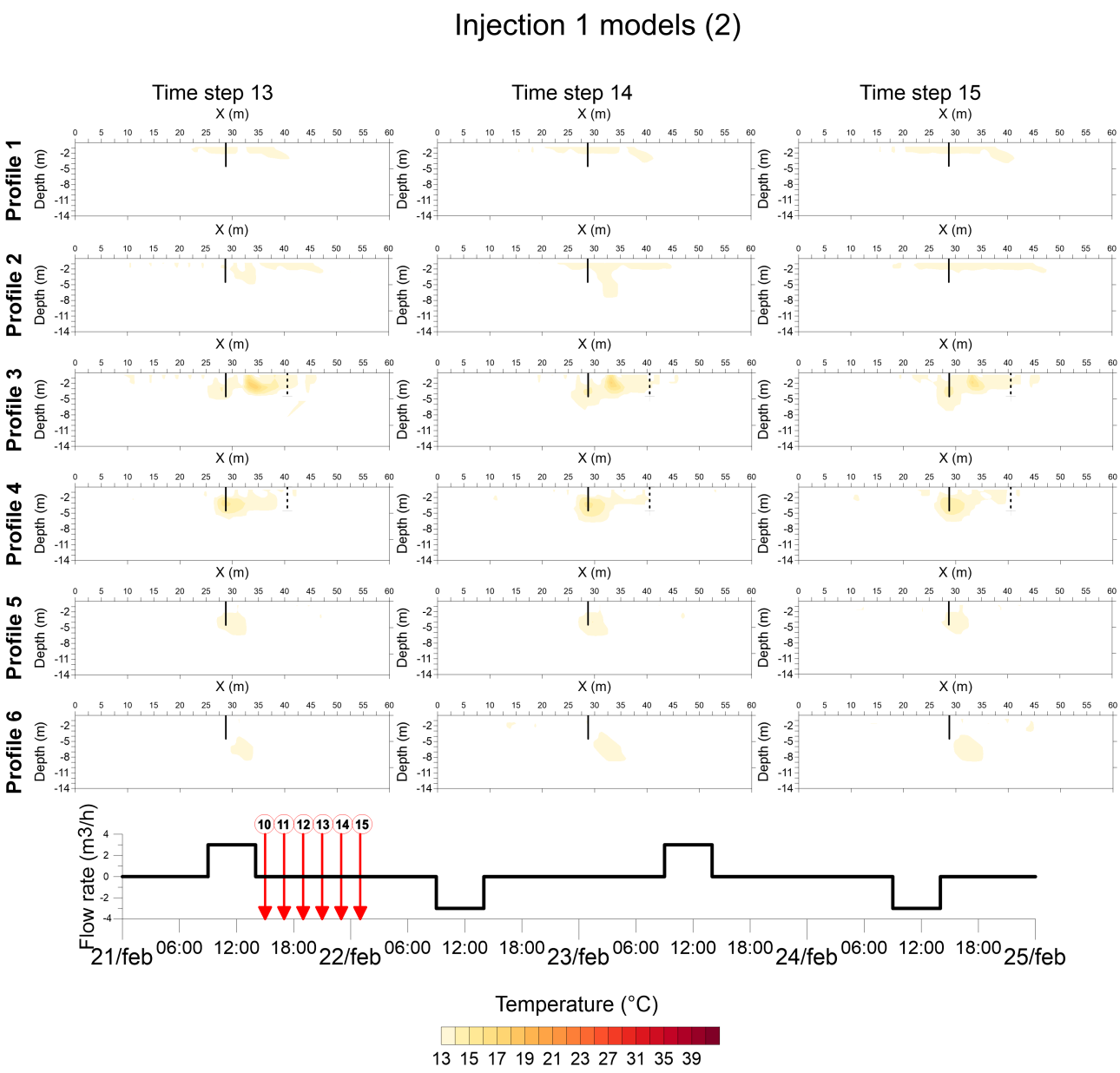

Figure 26. 2D Temperature conversion models of Injection 1 (part 2)

Profile 1 has almost no temperature changes. The highest temperatures cannot exceed 14°C and are located mostly at the surface. It is therefore very difficult to say that they are related to the injection process.

On the other hand, even though the temperature increment is low, Profile 6 has results that might be linked to the injection influence. Indeed, from the time step 11 a little spot with temperatures lower than 14°C appears in the boreholes' axis vicinity. The plume-shaped spot is a clear sign that such temperature increase is due to the Injection 1.

Profile 2 and 5 have similar temperature results. Differently from Profile 6, they have the plume from the first time step, still with values between 13°C and 14°C. The most important difference between Profile 2 and 5 results is the duration of the plume. As the results shown,

the plume in Profile 2 disappears in time step 12, while in Profile 6 it lasts until the last time step. However, this difference has been already mentioned previously in Paragraph 4.2.

Concerning Profile 4, its plume has been successfully monitored and represented in all time steps. It is generally constant over the time with values between 13°C and 16°C, but it starts to reduce its shape in the last three time steps.

Finally, in Profile 3, the plume is characterised by a pretty constant shape with the warmest temperatures located in the first time step. From that time step on, temperature starts to be cooled. The shape of the plume seems a bit dislocated and superficial, but it might be due to the water pumped from "PP". However, it should not be superficial (i.e. at least 1 m deep) and it is just the common effect of the resistivity models, where in the vicinity of the electrodes the resistivity is exaggerated with low or high values.

4.3.1.2 Temperature conversion results of Pumping 1

The obtained results of Pumping 1 phase are shown as usual in Figure 27 and 28. Globally, in these results temperatures are slightly higher than the previous case. However, this is due to the acquisitions considered. In Pumping 1 the time steps monitor all the phase plus few hours after, in Injection 1 they cover just the post-injection phase.

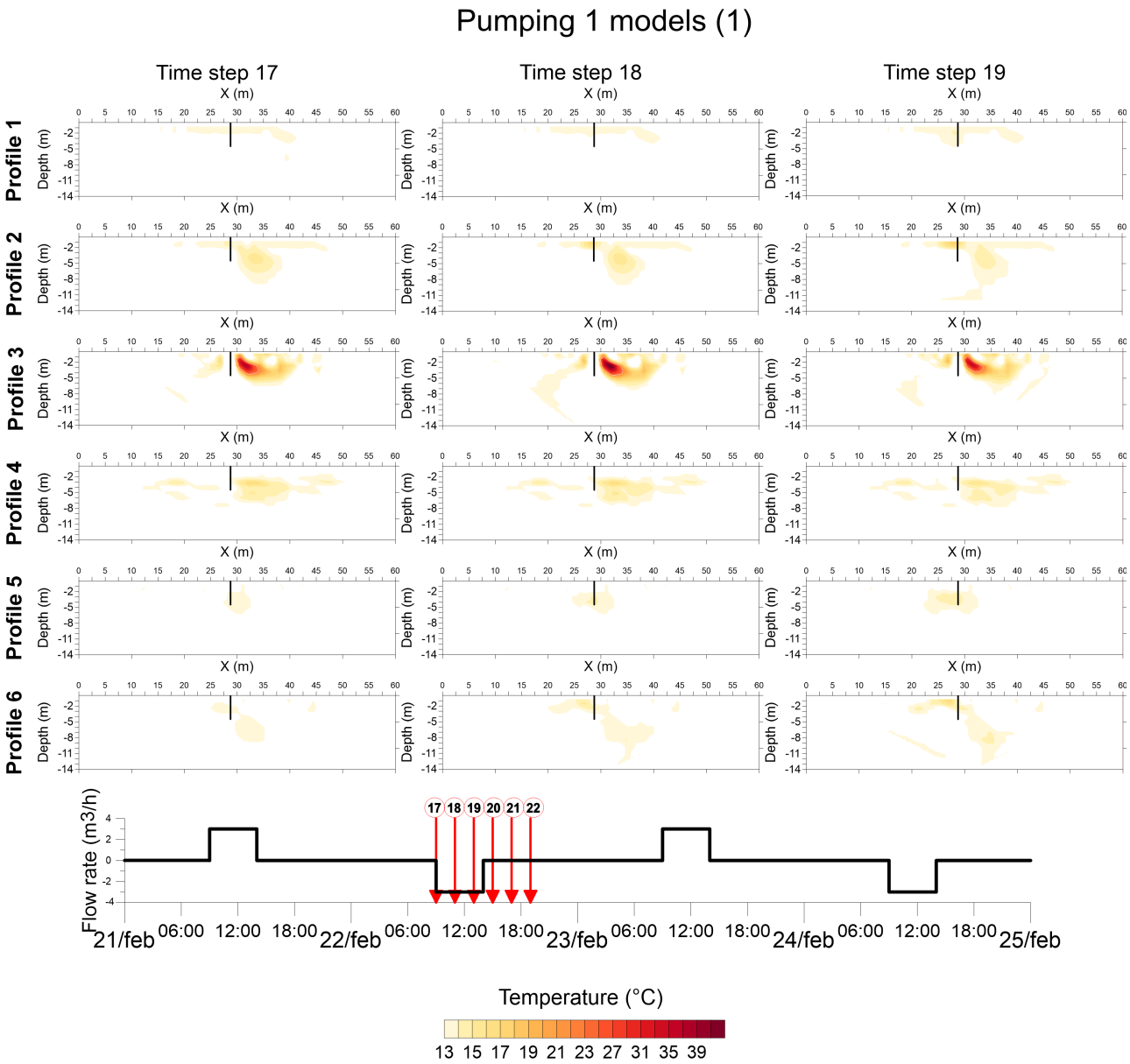

Figure 27. 2D Temperature conversion models of Pumping 1 (part 1)

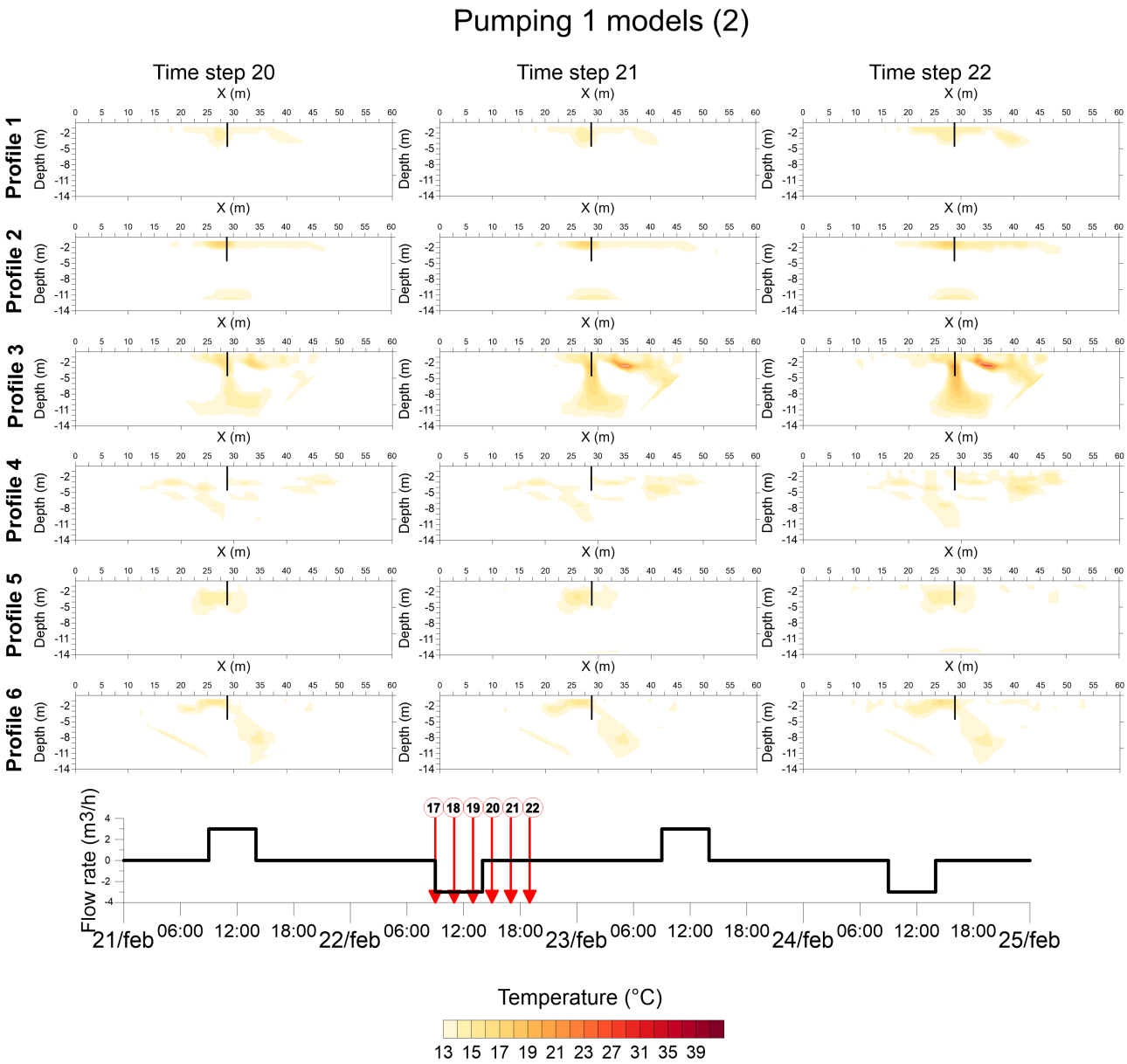

Figure 28. 2D Temperature conversion models of Pumping 1 (part 2)

Profile 1 does not seem to perfectly monitor the warm water recalled by the pumping operation. Anyway, a trace of the plume appears in time step 19 with temperatures that start to increase, reaching almost 15°C. Although the warmer area is superficial, it is close to the boreholes' axis and probably caused by the pumping water recall.

Profile 6 seems again to have better sensitivity to temperature variations. The plume is present since the first time step and reach maximum values of 14-15°C. Despite that, the shape of the plume is in most time steps distorted and too deep. Indeed, as already mentioned, the zones below 8 m have to be treated carefully due to the low image quality.

In Profile 2 temperature models, the hot water plume recalled is successfully monitored and shown in all the time steps related to the pumping operation (i.e. time steps 17-19). Although

the plume is slightly dislocated from the boreholes' axis, its temperatures seem realistic, with peak values slightly lower than 16°C. Once the pumping phase is stopped, i.e. at time step 20, the plume disappears.

As discussed before, Profile 5 models monitor successfully the plume in all the time steps. In this case, the plume is constant all over the time steps, with acceptable values close to the ones found in Profile 2, that range between 13°C and 16°C.

In the inner zone of the grid, Profile 4 has obtained similar results to Profile 2. Apart from those negligible little and light warm spots, the main warm plume has the same behaviour od the Plume found in Profile 2. With temperature values ranging from 13°C to 16°C, it lasts for the first three time steps and right after the end of the pumping operation it disappears.

Finally, as expected Profile 3 has the highest temperatures of the monitored phase. Looking at the models, it seems that the water pumped during the withdrawal is cold, while the hot water (17°C < T < 44°C) floats over the cold water "captured" by the well. When the pump is stopped, the captured area is warmed reaching temperatures up to 20°C.

Apart from the results of Profile 3, the temperatures of the other profiles seem coherent and realistic. Comparing the temperature values found in "Pz14" with Profile 4 and excluding the pumping phase, the values are coherent and both range between 13°C and 14°C.

On the other hand, Profile 3 results need to be discussed. First, the temperatures of the plume during the pumping phase seem quite high (T>40°C). Then, the post-pumping phase seems coherent with what observed in the direct measurements, where in the next 6h temperatures increase slowly. Despite that, comparing the converted temperature values with those taken from the CTD probes, it comes out that the converted values are slightly higher (i.e. 14-19°C vs 13-15°C).

4.3.1.3 Temperature conversion results of Injection 2

The temperature conversion results of the second phase are shown in the Figure 29, 30 and 31. For obvious reasons the temperatures are in general higher than the first injection monitored. Then, differently from the previous results, the heat plume is often not clear and quite spread. However, this is probably due to the two former operation which have strongly influenced the temperature distribution of the subsurface.

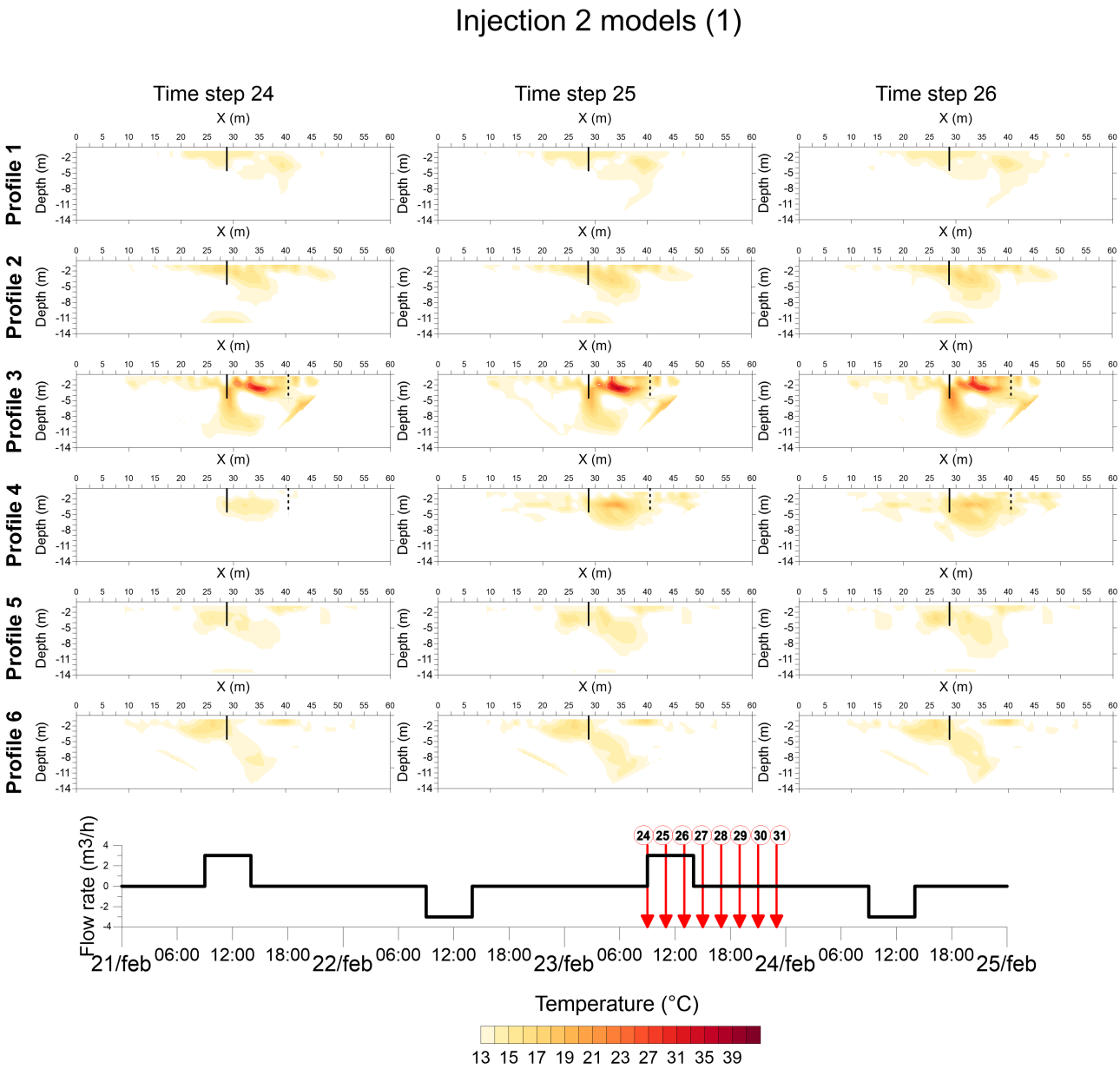

Figure 29. 2D Temperature conversion models of Injection 2 (part 1)

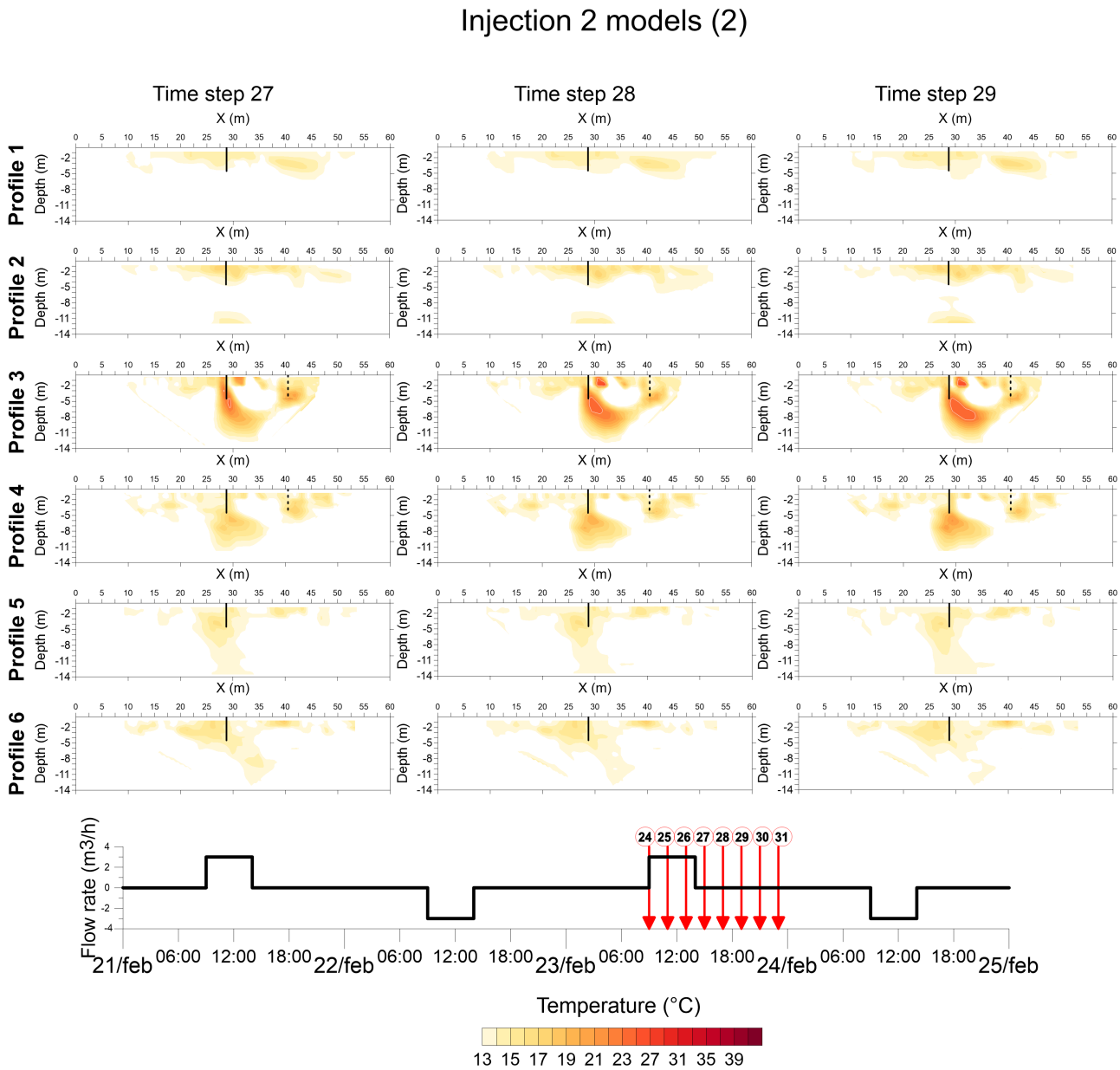

Figure 30. 2D Temperature conversion models of Injection 2 (part 2)

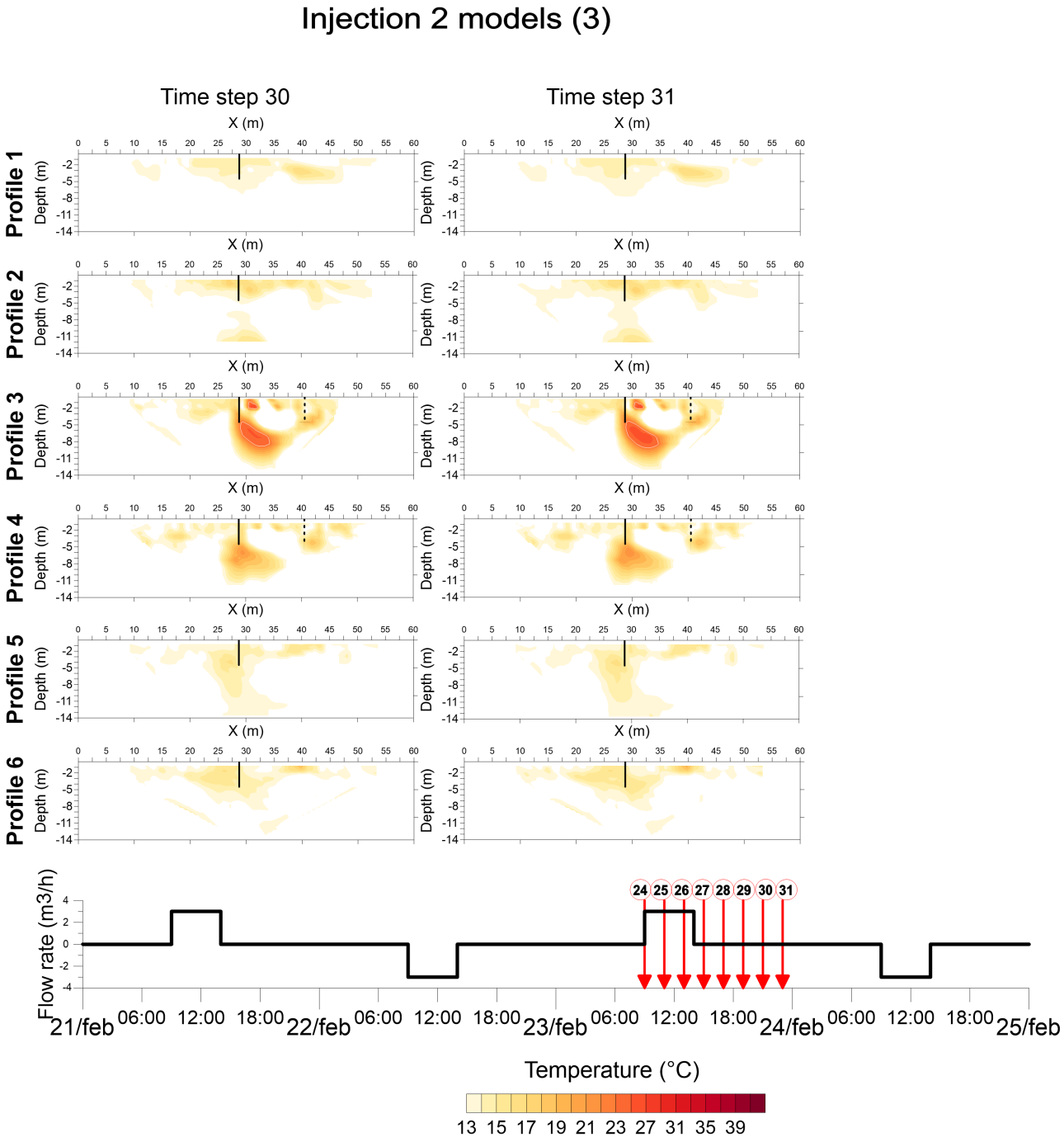

Figure 31. 2D Temperature conversion models of Injection 2 (part 3)

At the sides of the ERT grid, Profile 1 and 6 show similar results. As mentioned before, the plume is not clear in both profiles, but the warmer temperatures, which range between 13°C and 15°C, are still present in the vicinity of the boreholes' axis. As usual, in Profile 6 the warm temperatures last more than Profile 1, where normally temperatures drop after the end of the injection (i.e. time step 27).

Profile 2 and 5 have similar results to Profile 1 and 6. Similarly to Profile 6, in Profile 5 the plume is not clear but warmer temperatures ranging between 13°C and 17°C are close to the

boreholes' axis and constant all over the time step series. Profile 2 instead has a plume with the same range of temperature values that disappears once the injection is stopped.

As denoted in Pumping 1 results, even in this case Profile 4 results seem somehow similar to the ones found in Profile 2. The shape and the range of the temperature values are quite similar between each other. Despite that, after the end of the Injection 2 in Profile 4 the plume does not disappear but it just changes its shape. After, from time step 28 to 31, the plume increase slowly its temperatures reaching a peak of 22°C.

Finally, Profile 3 has always the most challenging results. Two plume of warm temperatures are present, one below the injection well and the other on its NE side. Their maximum temperatures are 19°C and 37°C respectively. As usual after the end of the injection, the hot temperature distribution changes, settling mostly in the vicinity of the well. Then, in the 4 last time steps the temperatures continue to grow slowly, reaching 25°C as a peak value.

To conclude, the results of this monitored phase are pretty acceptable. Apart from Profile 3, all profiles have successfully identified the temperature variations induced by the injection phase. Again, South-Eastern profiles (i.e. profiles 1, 2, 3) have been confirmed to be more sensitive and reactive to injection operations. On the other hand, North-Western profiles are less reactive, with lower temperature variations. As mentioned before, this behaviour could be caused by some heterogeneities present across the site (i.e. effective porosity higher in the South-Eastern zone of the grid). Instead, the hypothesis that this behaviour is due to the flow direction might be discarded, since all the profiles are parallel to the groundwater flow direction (NE).

Differently from the other results, Profile 3 ones are debatable. Considering the time steps taken during the injection (i.e. time steps 24-26), the main hot water plume seems to be shifted towards NE and superficial. The maximum temperatures are in general acceptable (33°C), since they are enough lower than the maximum temperature recorded in "Pz16" (42°C) and higher then the maximum in "Pz17" (22°C). On the other hand, the shifted position of the plume might be related to the cold water withdrawal from the well "PP". As mentioned before, the hot water injected in "Pz15" is at the same time withdrawn from "PP" with the same flow rate. Therefore, for obvious reasons the injection and the withdrawal force somehow the "floating" injected hot water to be captured by "PP" well. Apart from the position of the plume, such hypothesis can actually be confirmed by the higher temperatures injected in the second injection. As a matter fact, direct measurements have shown that the second injection has a peak 4°C higher then the first, but the fuel boiler gives a fixed and maximum temperature

variation of +30°C. In addition to that, looking at the temperature conversion results of profile 3, the temperature close to "PP" is indeed up to 3°C higher than the normal temperature, confirming what stated.

Conversely, the time steps 27-31 have more challenging discussions. Apart from the hot plume which seems to have acceptable results (peak temperature 25°C), the blanked area on its NE side is still not acceptable. Note that such blanked area corresponds to the high resistivity spot found in Paragraph 4.2. Those high resistivity changes (>100%) have caused a strong drop of temperatures, reaching values even lower than 1°C. Unfortunately, such low temperatures are not physically possible and no clear explanations have been found.

4.3.1.4 Temperature conversion results of Pumping 2

The last temperature conversion results are shown in Figure 32 and 33. Globally, these results are the the continuation of the previous injection phase. Indeed, temperatures keep on growing in the inner profiles of the grid while start to decrease at the sides.

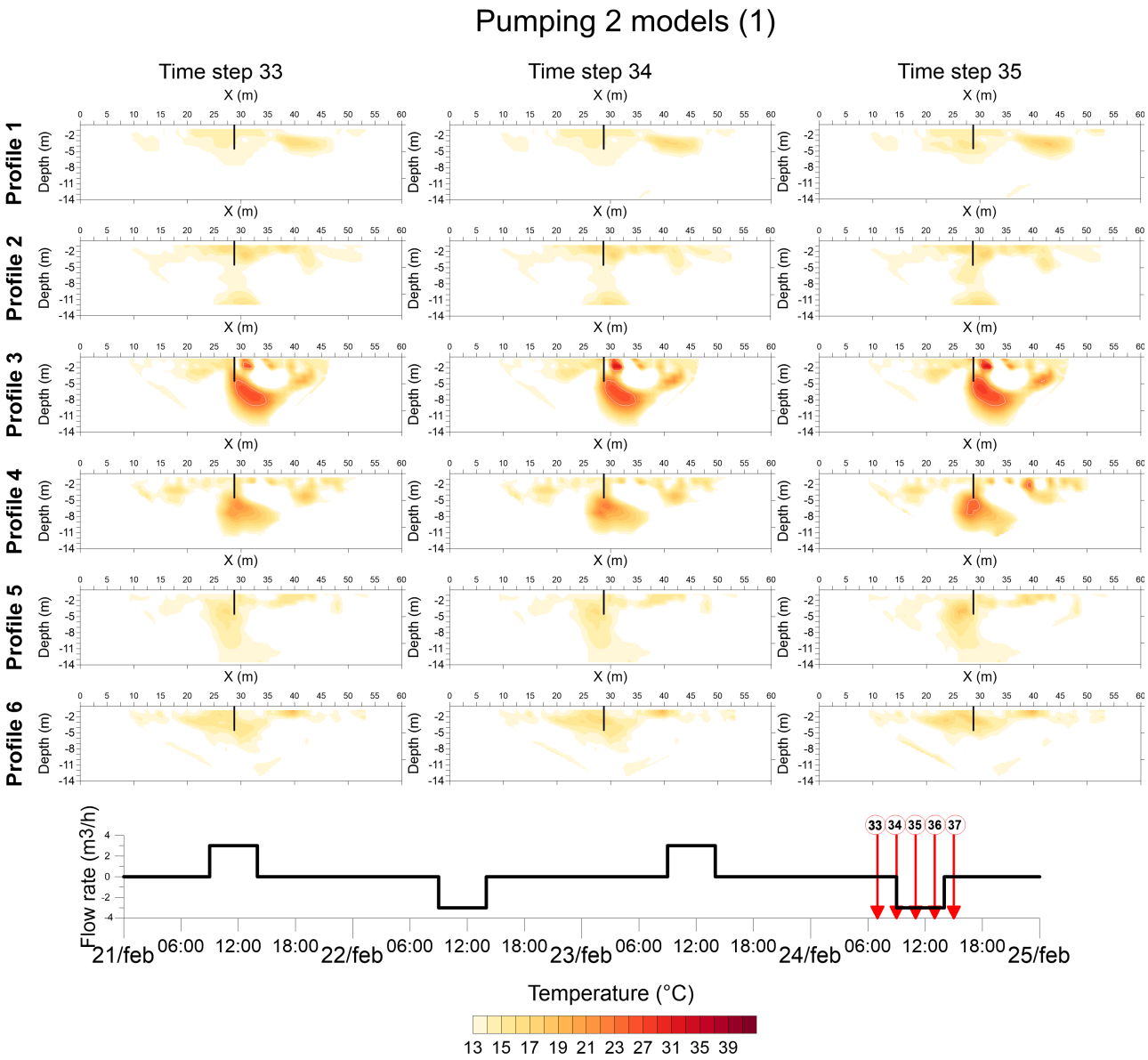

Figure 32. 2D Temperature conversion models of Pumping 2 (part 1)

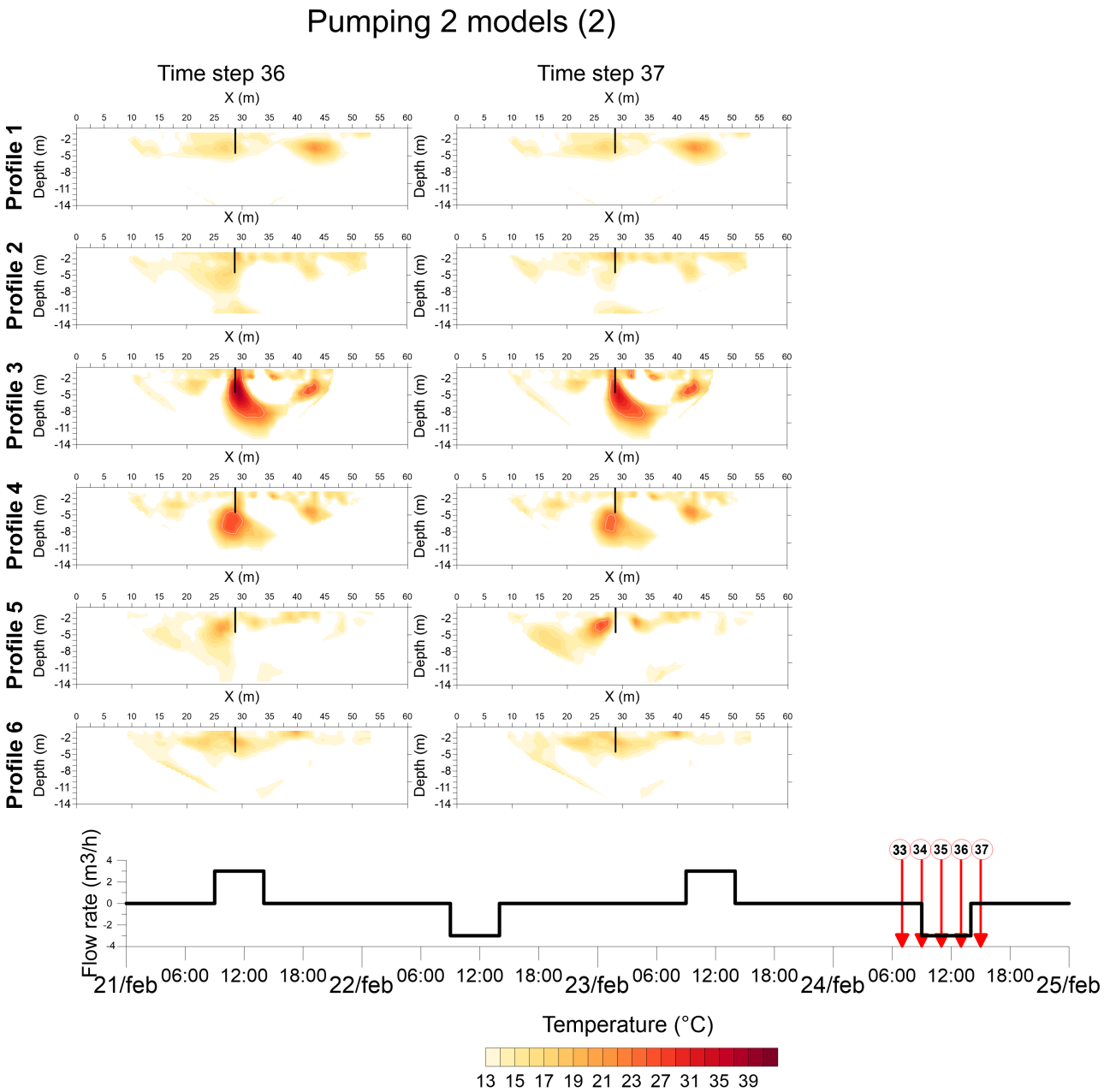

Figure 33. 2D Temperature conversion models of Pumping 2 (part 2)

At the extremes, Profile 1 and 6 have in general weak temperature variations, reaching peak values of 18°C. The influence of Pumping 2 is slightly detected in both profiles after 2h the beginning of the operation (i.e. time step 35). From that moment, the temperature distribution changes slightly its shape, probably due to the pumping influence.

Profile 2 and 5 results show also a behaviour similar to what seen in profiles 1 and 6. As a matter of fact, even in this case the temperature distributions are constant in the two first time steps. Next, two hours later the pumping influence is recorded with bigger plume and higher temperatures (17°C in Profile 2 and 26°C in Profile 5).

Finally, in the inner profiles the monitored results are slightly different. In both Profile 3 and 4, temperatures continue to grow slowly in the two first time steps. Instead, from time step 35 on, the increasing temperatures are boosted by the pumping phase, reaching the peak in time step 36 (40°C and 26°C respectively). These results are in general quite acceptable with the temperature ranges found in the direct measures. Despite that, in both profiles the blanked area between 30 m and 40 m has unusual low temperatures, even lower than 1°C. Again, no further explanations have been found, since such area is the same as the one found in Injection 2.

To conclude the discussion of the 2D time-lapse temperature models, we might consider in general all the phases reliable. The temperature values are not exactly correspondent to those found from the direct measurements. As a matter of fact, a direct comparison between the two different results is shown in Figures A9 and A10 in Annex. In both graphs the results of the temperature conversion of one profile are compared to the breakthrough curves of the two closest piezometers. Moreover, the temperature converted values used in the curve are mean values from inverted blocks in the vicinity of the coordinates x = 28.75 m, depth = 5 m. As the graphs show, the temperatures and the trend are not perfectly similar. However, they can be considered acceptable since many assumptions have been used. Then, the direct measurements itself are punctual measurements and it is difficult to blindly trust them.

Finally, overrate the importance of this comparison would lead to misinterpreting the results, that is why just the range of temperature is sufficient to consider reliable such temperature conversion results.

4.4 3D time-lapse inversion

4.4.1 Results and discussion

As mentioned before in Chapter 3, some technical problems have been found at this stage. Both the technical problems and the obtained 2D results have led to perform just the inversion of Injection 1 phase.

For the 3D analysis it has been followed what done with the 2D results. Therefore, to assess the images quality the sensitivity results have been used (Figure A11 in Annex). The idea was actually to use a 3D equivalent of the DOI index (i.e. the Volume Of Investigation index, VOI), but unfortunately RES3DINV has no implemented function for it.

4.4.1.1 3D Background resistivity model

In addition to the sensitivity, also the background model (Figure 34) has been inverted and compared with the 2D results. Of course the 3D results might be less precise than the 2D ones. Therefore, the analysis has been limited to the comparison and discussion between the two type of results. Represented with the same scale, 3D results are perfectly similar and in agreement with 2D ones. As expected, 3D background model seems less precise, with resistivity values more smeared respect the 2D ones. Despite that, the resistivity values range is coincident for all profiles and the only differences remain in the highest resistivity values that seem lowered or smeared from the 2D results.

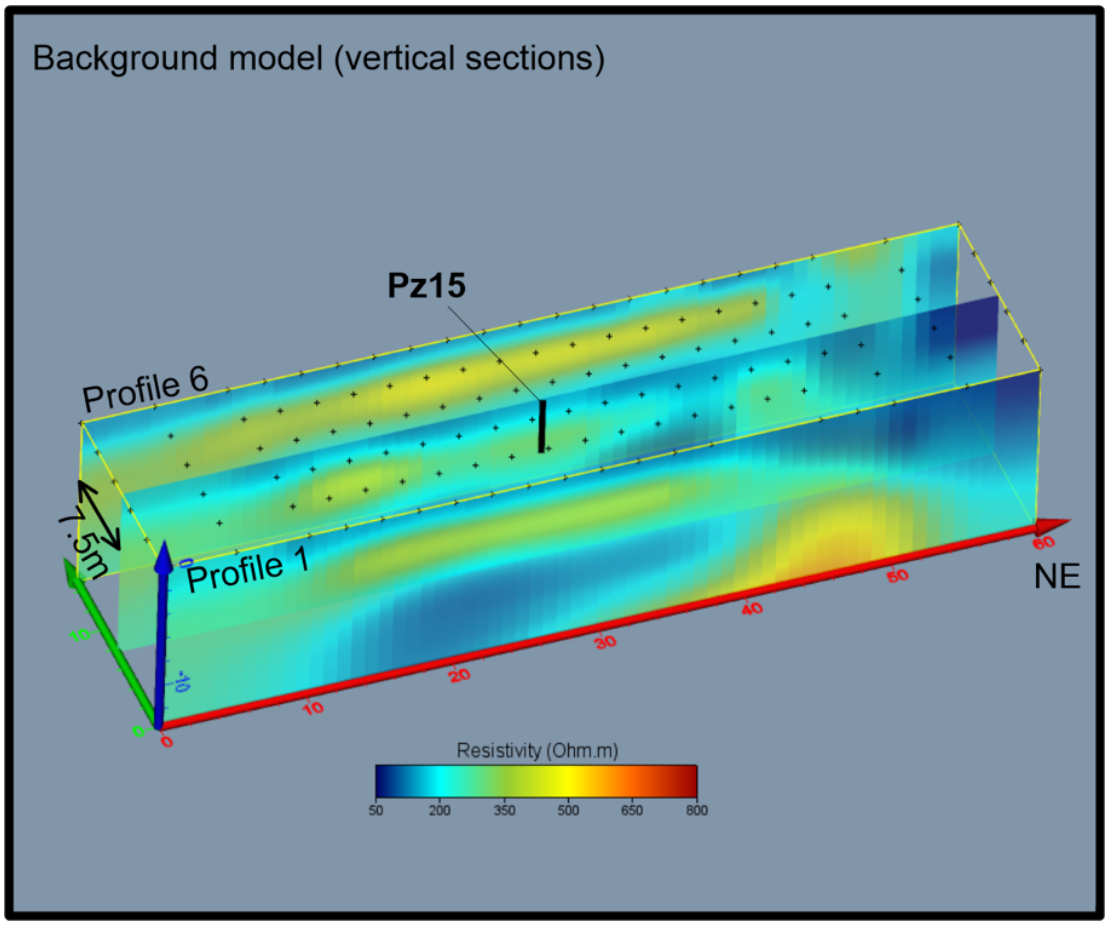

Figure 34. 3D Background resistivity model (vertical sections are 3 XZ planes with equation Y=0, Y=7.5, Y=15)

Once compared and confirmed the expected analogies between the 2D profiles and the 3D vertical sections, the 3D background model can be considered reliable. As result, the horizontal (XY plane) resistivity distribution might be described and commented. Let us analyse two sections, one at 4 m depth (Figure 35) and the other at 7 m depth (Figure 35).

Differently from the first two meters, the resistivity distribution at 4 m shows an important information. As a matter of fact, it seems to have lower resistivity values in the area covered by Profile 1, 2 and 3. Furthermore, the distribution at 7 m depth confirm what found at 4 m depth. To conclude, the low resistivity present in the SE area in both the horizontal sections confirms somehow what denoted previously from the 2D results. Hence, the SE area is affected by geological heterogeneities probably related to the effective porosity of the subsurface. For this reason, such area is more sensitive to injection and pumping operations, but not able to "hold" the warm water.

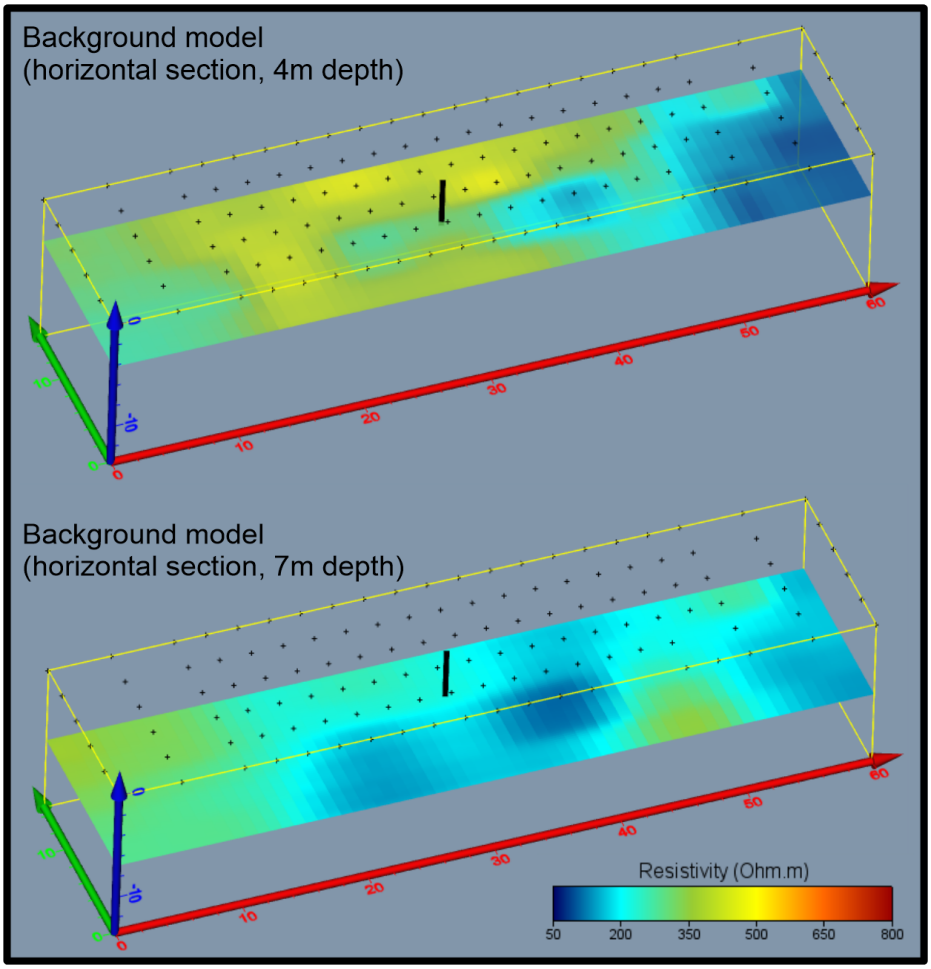

Figure 35. 3D Background resistivity model (horizontal sections are 2 XY planes with equations Z=4 and Z=7)

4.4.1.2 3D Resistivity results of Injection 1

To represent the 3D models in terms of resistivity percentage changes, the same procedure and consideration made in Paragraph 4.2.1.4 have been made. For simplicity, the description is skipped and referred to the cited paragraph. The 3D models of Injection 1 are shown in Figure 36, still using the same scale used in the 2D results.

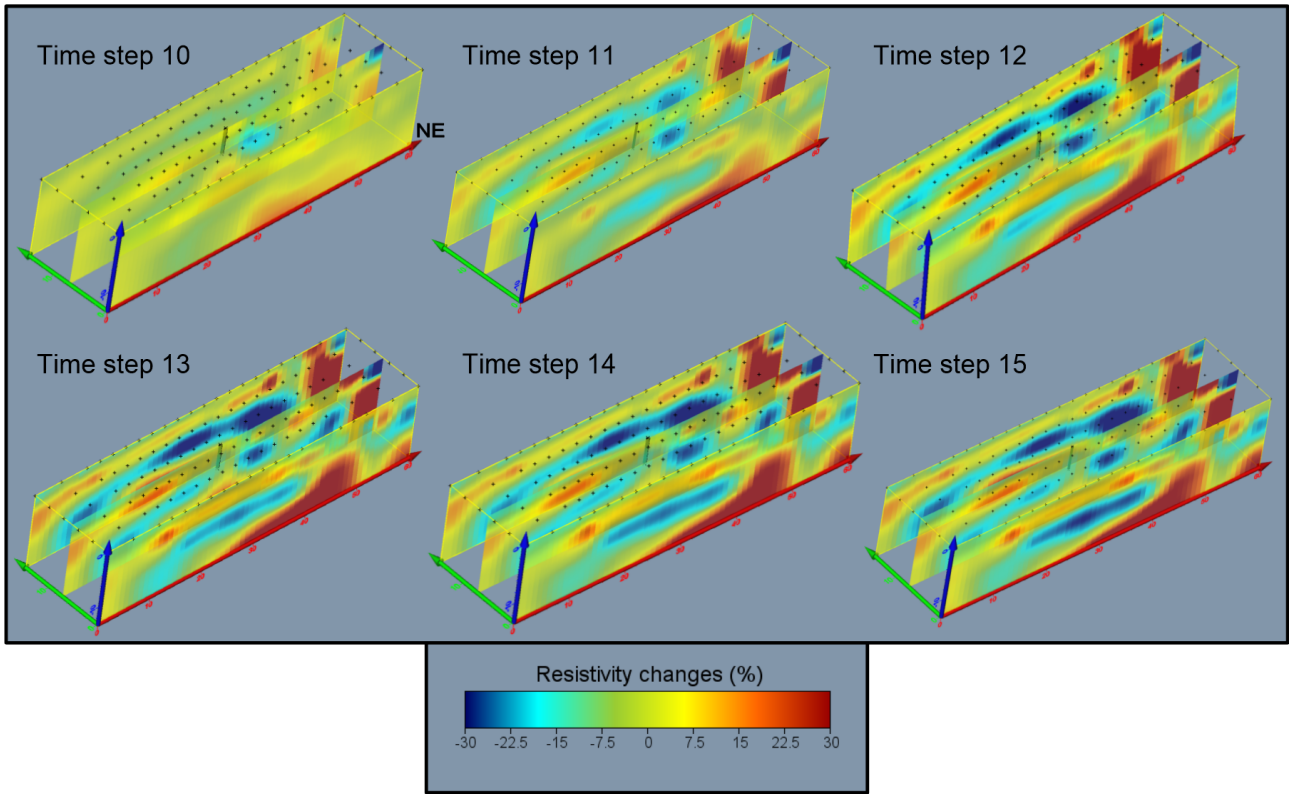

Figure 36. 3D Time-lapse resistivity models of Injection 1

Analysing the results, the resistivity percentage values seem rather higher and exaggerated. As a matter of fact, plume values reach values even lower than -30%. Some high resistivity changes are also recorded at 4 m depth, in the transition layer (i.e. sandy loam and gravel). Furthermore, the more you go on with the time steps, the more exaggerated will be the changes. In spite of these disappointing results, the plume has been successfully monitored along all the time steps and its shape recall the one found in 2D results. Then, the most reliable model seems to be the first one (time step 10), having changes not as marked as in the following time steps.

As far as the unexpected results obtained, there actually might be an explanation on these exaggerated resistivity changes. First, it should be highlight the fact that the time-lapse inversion algorithm used is not the same as the one used in the 2D inversion. As mentioned before, the inversion algorithm used is the independent one, which means that no time constraints are applied between the 3D models. Then, the 3D inversion algorithm is similar to the 2D one, but it mainly allows the resistivity to change across the three spatial dimensions. This means instead, that the 3D model has more degrees of freedom to fit the dataset. Last, the 3D dataset is almost a 2D dataset with some added 3D measurements, since the measures taken not in parallel are just the 2.5% of the total. These three characteristics of the 3D

acquisition and inversion might somehow represent the limitations that have caused such exaggerated resistivity changes in the models.

With these relatively bad results, temperature conversion or inversion of the remaining phases are surely not convenient. However, an interesting analysis of the 3D results might be carried out. Considering just the resistivity changes model of time step 10, a partial volume of the warm water injected could be estimated. Let us assume also the effective porosity equal to 4% (Wildemeersch et al. 2014) and the maximum percentage change fixed at -10%, since higher values will gather artefacts. The volume of soil with values below -10% can be computed thanks to a implemented function (called "Isosurface") present in Voxler 4® (Figure A12 in Annex). As result, the water volume with temperature higher than 16.6°C corresponds to 7.72 m^3, which is exactly 51% of the total.

5 Conclusions and perspectives

As described and discussed so far, the subject of the present Master Thesis was a cyclic aquifer thermal storage experiment monitored with 4D ERT survey. Apart from the general goal, three specific objectives have been fixed and discussed.

First, the ability of the ERT survey to spot temperature variations. As shown and discussed in the previous Chapter, the 4D ERT survey has globally demonstrated to obtain good results. In particular, comparing the 2D time-lapse temperature models with the temperature ranges obtained from the direct measurements, the resistivity changes converted in temperature values are comparable with the direct temperature values. The results confirmed also the accuracy of the temperature conversion method, already used in recent studies with smaller sites (Hermans et al. 2012; Hermans et al. 2015; Giordano et al. 2017; Giordano, Comina, and Mandrone 2016).

The second objective was focused on the ability of the 4D ERT survey to spot spatial-temporal variations of the plume. Despite the possible problems related to assumptions, to the site extension and to the large monitoring time interval, both 2D resistivity and temperature models have been able to monitor the plume variations across the time and the space. The plume has been detected even in the farthest profiles where no subsurface changes were expected, such as Profile 1 and 6. Furthermore, the subsurface changes obtained are also physically reasonable and in agreement with the stage of the phases.

At the end of the experiment, according to the results the subsurface resulted obviously warmer than before. Both the hot water injections have caused temperature variations in all profiles, mostly in the vicinity of the injection well “Pz15” and the withdrawal well “PP”. Instead, pumping phases have often caused a further increment of the temperatures in the inner profiles (i.e. Profiles 3 and 4), while due to their influence they caused cooling of the subsurface temperatures in extreme profiles. These results have been confirmed just partially by the 3D time-lapse resistivity models.

Moreover, the used image appraisal tools have somehow fixed the quality of these results, making the interpretation reliable.

Besides the achievements, some models of Profile 3 have obtained unclear results. In particular, in Chapter 4 the presence of a high resistivity spot after Injection 2 is still unexplainable. Many analyses have been done, but no plausible explanations have been found.

Also the 3D results have not shown good results. The independent inversion used as well as the 3D dataset poor of 3D information have produced controversial results.

Finally, the third objective was to understand if the survey was able to spot heterogeneities in the studied site. Initially, the symmetric configuration of the piezometers has allowed to compare CTD results of two couples of piezometers. Although the CTD monitoring network have been used just to furnish temperature ranges, it also allowed to compare different temperature breakthrough curves that in homogeneous conditions are supposed to be similar. Since they resulted different, a first remote hypothesis on concerning the heterogeneity of the site was considered.

Instead, the second clue has been noticed during the interpretation of 2D time-lapse resistivity and temperature models. As a matter of fact, in all models an asymmetric behaviour of the plume has been detected. The profiles situated in the South-Eastern area (i.e. Profile 1, 2 and 3) have turned out to be more sensitive to injection or pumping phases. On the other hand, Profile 4, 5 and 6 have shown a constant behaviour to retain the warm, reacting in a less sensitive way to the injections or withdrawals performed.

Successively, a final proof has been added. In fact, the 3D background model confirmed the heterogeneity hypothesis previously stated. The model clearly shown a heterogeneous resistivity distribution across the XY plane which is probably linked to the effective porosity.

Although some controversial results have been obtained, the present Thesis has globally accomplished the aimed objectives. However, in order to improve the results obtained, some future perspectives might be discussed. At this stage, the 3D inversion and acquisition might be improved. A more complete 3D dataset will help to gain accuracy in the 3D time-lapse model. As Loke, Dahlin, and Rucker (2014) have demonstrated in their study, 3D independent time-lapse inversion is very sensible to noise. With dataset as the one used in this Thesis, a time-constrained inversion is needed to achieve better results. Furthermore, once got a good time-lapse model, the temperature conversion can be extended to the 3D models and then used to monitor the volume injected, as proposed at the end of Chapter 4.

Another interesting perspective might be to reproduce an aquifer thermal energy storage experiment with a longer monitoring time frame which lasts at least one month. It would be interesting to understand how a 4D ERT survey would detect the effects of many cycles and what degree of quality would reach.

Finally, the last perspective aims to provide a complete monitoring tool for ATES systems. The idea consists to build up a permanent ERT monitoring station in an aquifer exploited by an ATES system. In this way, the permanent station will automatically acquire dataset, monitoring the subsurface changes caused by the ATES. Similar systems already exist and they have been tested. An example is the Automated time-Lapse Electric Resistivity (ALERT) system (BGS, n.d.) which monitors remotely an ongoing landslide with an in situ permanent ERT grid.

6 References

Alkilani, Mahmud M., K. Sopian, M. A. Alghoul, M. Sohif, and M. H. Ruslan. 2011. 'Review of Solar Air Collectors with Thermal Storage Units'. *Renewable and Sustainable Energy Reviews* 15 (3): 1476–90. doi:10.1016/j.rser.2010.10.019.

Andersson, Olof. 2007. 'Aquifer Thermal Energy Storage (ATES)'. In *Thermal Energy Storage for Sustainable Energy Consumption*, 155–76. NATO Science Series. Springer, Dordrecht. doi:10.1007/978-1-4020-5290-3_8.

Arato, A., C. Comina, N. Giordano, and G. Mandrone. 2015. 'Monitoring of a Borehole Thermal Energy Storage System Using 2D and 3D Resistivity Surveys in an Highly Urbanized Area'. In . doi:10.3997/2214-4609.201413726.

Archie, G. E. 1942. 'The Electrical Resistivity Log as an Aid in Determining Some Reservoir Characteristics'. *Transactions of the AIME* 146 (1): 54–62. doi:10.2118/942054-G.

Arning, E., M. Kölling, H. D. Schulz, B. Panteleit, and J. Reichling. 2006. 'Einfluss oberflächennaher Wärmegewinnung auf geochemische Prozesse im Grundwasserleiter'. *Grundwasser* 11 (1): 27–39. doi:10.1007/s00767-006-0116-0.

Aster, Richard C., Brian Borchers, and Clifford H. Thurber. 2013a. 'Chapter Nine - Nonlinear Regression'. In *Parameter Estimation and Inverse Problems (Second Edition)*, 217–38. Boston: Academic Press. doi:10.1016/B978-0-12-385048-5.00009-4.

———. 2013b. 'Chapter One - Introduction'. In *Parameter Estimation and Inverse Problems (Second Edition)*, 1–23. Boston: Academic Press. doi:10.1016/B978-0-12-385048-5.00001-X.

BGS. n.d. 'Automated Time-Lapse Electrical Resistivity (ALERT)'. *British Geological Survey, Natural Environmental Research Council*. http://www.bgs.ac.uk/research/tomography/ALERT.html.

Brielmann, Heike, Christian Griebler, Susanne I. Schmidt, Rainer Michel, and Tillmann Lueders. 2009. 'Effects of Thermal Energy Discharge on Shallow Groundwater Ecosystems'. *FEMS Microbiology Ecology* 68 (3): 273–86. doi:10.1111/j.1574-6941.2009.00674.x.

Brielmann, Heike, Tillmann Lueders, Kathrin Schreglmann, Francesco Ferraro, Maria Avramov, Verena Hammerl, Philipp Blum, Peter Bayer, and Christian Griebler. 2011. 'Oberflächennahe Geothermie und ihre potenziellen Auswirkungen auf Grundwasserökosysteme'. *Grundwasser* 16 (2): 77. doi:10.1007/s00767-011-0166-9.

Brouyère, Serge. 2001. 'Etude et modélisation du transport et du piégeage des solutés en milieu souterrain variablement saturé. Evaluation des paramètres hydrodispersifs par la réalisation et l'interprétation d'essais de traçage in situ'. Université de Liège, Sart Tilman, Belgique. http://orbi.ulg.ac.be/handle/2268/40804.

Cassiani, Giorgio, Andrew Binley, and Ty P. A. Ferré. 2006. 'UNSATURATED ZONE PROCESSES'. In *Applied Hydrogeophysics*, 75–116. NATO Science Series. Springer, Dordrecht. doi:10.1007/978-1-4020-4912-5_4.

Caterina, David, Jean Beaujean, Tanguy Robert, and Frédéric Nguyen. 2013. 'A Comparison Study of Image Appraisal Tools for Electrical Resistivity Tomography'. *Near Surface Geophysics*. doi:10.3997/1873-0604.2013022.

Cho, I., and J. Yeom. 2007. 'Crossline Resistivity Tomography for the Delineation of Anomalous Seepage Pathways in an Embankment Dam'. *GEOPHYSICS* 72 (2): G31–38. doi:10.1190/1.2435200.

'Climate Action'. 2015. Text. *European Commission - European Commission*. July 23. https://ec.europa.eu/info/strategy/climate-action_en.

Dahlin, Torleif, and Bing Zhou. 2004. 'A Numerical Comparison of 2D Resistivity Imaging with 10 Electrode Arrays'. *Geophysical Prospecting* 52 (5): 379–98. doi:10.1111/j.1365-2478.2004.00423.x.

Edwards, L. 1977. 'A Modified Pseudosection for Resistivity and Ip'. *GEOPHYSICS* 42 (5): 1020–36. doi:10.1190/1.1440762.

Evliya, Hunay. 2007. 'Energy Storage for Sustainable Future —A Solution to Global Warming'. In *Thermal Energy Storage for Sustainable Energy Consumption*, 87–99. NATO Science Series. Springer, Dordrecht. doi:10.1007/978-1-4020-5290-3_5.

Farquharson, Colin G., and Douglas W. Oldenburg. 1998. 'Non-Linear Inversion Using General Measures of Data Misfit and Model Structure'. *Geophysical Journal International* 134 (1): 213–27. doi:10.1046/j.1365-246x.1998.00555.x.

Fiandaca, G., and P. L. Cosentino. 2008. 'The New "Maximum Yield Grid" (MYG) Array in Full 3D Resistivity Tomography'. In . doi:10.3997/2214-4609.20146313.

Fisch, M. N, M Guigas, and J. O Dalenbäck. 1998. 'A Review of Large-Scale Solar Heating Systems in Europe'. *Solar Energy* 63 (6): 355–66. doi:10.1016/S0038-092X(98)00103-0.

Giordano, N., A. Arato, C. Comina, and G. Mandrone. 2017. 'Time-Lapse Electrical Resistivity Imaging of the Thermally Affected Zone of a Borehole Thermal Energy Storage System near Torino (Northern Italy)'. *Journal of Applied Geophysics* 140 (May): 123–34. doi:10.1016/j.jappgeo.2017.03.015.

Giordano, N., C. Comina, and G. Mandrone. 2016. 'Laboratory Scale Geophysical Measurements Aimed at Monitoring the Thermal Affected Zone in Underground Thermal Energy Storage (UTES) Applications'. *Geothermics* 61 (May): 121–34. doi:10.1016/j.geothermics.2016.01.011.

Hadorn, J.-C. 2008. 'Advanced Storage Concepts for Active Solar Energy'. In . http://www.solarthermalworld.org/sites/gstec/files/Hadorn_storage.pdf.

Hayley, Kevin, L. R. Bentley, M. Gharibi, and M. Nightingale. 2007. 'Low Temperature Dependence of Electrical Resistivity: Implications for near Surface Geophysical Monitoring'. *Geophysical Research Letters* 34 (18): L18402. doi:10.1029/2007GL031124.

Hermans, T., A. Vandenbohede, L. Lebbe, and F. Nguyen. 2012. 'A Shallow Geothermal Experiment in a Sandy Aquifer Monitored Using Electric Resistivity Tomography'. *GEOPHYSICS* 77 (1): B11–21. doi:10.1190/geo2011-0199.1.

Hermans, Thomas. 2014. ‘Integration of near-Surface Geophysical, Geological and Hydrogeological Data with Multiple-Point Geostatistics in Alluvial Aquifers’. Liège: Université de Liège, Liège, Belgique. http://orbi.ulg.ac.be/handle/2268/163547.

Hermans, Thomas, Frédéric Nguyen, Tanguy Robert, and Andre Revil. 2014. ‘Geophysical Methods for Monitoring Temperature Changes in Shallow Low Enthalpy Geothermal Systems’. *Energies* 7 (8): 5083–5118. doi:10.3390/en7085083.

Hermans, Thomas, Samuel Wildemeersch, Pierre Jamin, Philippe Orban, Serge Brouyère, Alain Dassargues, and Frédéric Nguyen. 2015. ‘Quantitative Temperature Monitoring of a Heat Tracing Experiment Using Cross-Borehole ERT’. *Geothermics* 53 (January): 14–26. doi:10.1016/j.geothermics.2014.03.013.

Jesußek, Anna, Sibylle Grandel, and Andreas Dahmke. 2013. ‘Impacts of Subsurface Heat Storage on Aquifer Hydrogeochemistry’. *Environmental Earth Sciences* 69 (6): 1999–2012. doi:10.1007/s12665-012-2037-9.

Kearey, Philip, Michael Brooks, and Ian Hill. 2002. *An Introduction to Geophysical Exploration*. Wiley.

Klepikova, Maria, Samuel Wildemeersch, Thomas Hermans, Pierre Jamin, Philippe Orban, Frédéric Nguyen, Serge Brouyère, and Alain Dassargues. 2016. ‘Heat Tracer Test in an Alluvial Aquifer: Field Experiment and Inverse Modelling’. *Journal of Hydrology* 540 (September): 812–23. doi:10.1016/j.jhydrol.2016.06.066.

LaBrecque, D., and X. Yang. 2001. ‘Difference Inversion of ERT Data: A Fast Inversion Method for 3-D In Situ Monitoring’. *Journal of Environmental and Engineering Geophysics* 6 (2): 83–89. doi:10.4133/JEEG6.2.83.

Lee, Kun Sang. 2013. ‘Aquifer Thermal Energy Storage’. In *Underground Thermal Energy Storage*, 59–93. Green Energy and Technology. Springer, London. doi:10.1007/978-1-4471-4273-7_4.

Loke, M. H. 2001. ‘Constrained Time-Lapse Resistivity Imaging Inversion’. In . http://earthdoc.eage.org/publication/publicationdetails/?publication=44778.

———. 2016a. ‘Tutorial : 2-D and 3-D Electrical Imaging Surveys’. GEOTOMOSOFT SOLUTIONS GEOTOMO SOFTWARE PTY LTD. http://www.geotomosoft.com/downloads.php.

———. 2016b. ‘RES2DINVx64 Ver. 4.06 with Multi-Core and 64-Bit Support, Rapid 2-D Resistivity & IP Inversion Using the Least-Squares Method’. GEOTOMOSOFT SOLUTIONS GEOTOMO SOFTWARE PTY LTD.

———. 2017. ‘RES3DINVx64 Ver. 3.12 Basic and Professional Versions with Multicore and 64-Bit Support, Rapid 3-D Resistivity & IP Inversion Using the Least-Squares Method’. GEOTOMOSOFT SOLUTIONS GEOTOMO SOFTWARE PTY LTD.

Loke, M. H., and R. D. Barker. 1995. ‘Least-Squares Deconvolution of Apparent Resistivity Pseudosections’. *Geophysics* 60 (6): 1682–90. doi:10.1190/1.1443900.

———. 1996. ‘Practical Techniques for 3D Resistivity Surveys and Data inversion1’. *Geophysical Prospecting* 44 (3): 499–523. doi:10.1111/j.1365-2478.1996.tb00162.x.

Loke, M. H., J. E. Chambers, D. F. Rucker, O. Kuras, and P. B. Wilkinson. 2013. 'Recent Developments in the Direct-Current Geoelectrical Imaging Method'. *Journal of Applied Geophysics* 95 (August): 135–56. doi:10.1016/j.jappgeo.2013.02.017.

Loke, M. H., T. Dahlin, and D. F. Rucker. 2014. 'Smoothness-Constrained Time-Lapse Inversion of Data from 3D Resistivity Surveys'. *Near Surface Geophysics* 12 (1): 5–24. doi:10.3997/1873-0604.2013025.

McGillivray, P. R., and D. W. Oldenburg. 1990. 'Methods for Calculating Fréchet Derivatives and Sensitivities for the Non-Linear Inverse Problem: A Comparative Study1'. *Geophysical Prospecting* 38 (5): 499–524. doi:10.1111/j.1365-2478.1990.tb01859.x.

Nguyen, Frédéric. 2016. 'Inversion in Applied Geophysics. Lectures' Notes'. Unpublished.

Oldenburg, D., and Y. Li. 1999. 'Estimating Depth of Investigation in Dc Resistivity and IP Surveys'. *GEOPHYSICS* 64 (2): 403–16. doi:10.1190/1.1444545.

Perrone, A., V. Lapenna, and S. Piscitelli. 2014. 'Electrical Resistivity Tomography Technique for Landslide Investigation: A Review'. *Earth-Science Reviews* 135 (August): 65–82. doi:10.1016/j.earscirev.2014.04.002.

Raymond, Jasmin, René Therrien, Louis Gosselin, and René Lefebvre. 2011. 'A Review of Thermal Response Test Analysis Using Pumping Test Concepts'. *Ground Water* 49 (6): 932–45. doi:10.1111/j.1745-6584.2010.00791.x.

Roy, A., and A. Apparao. 1971. 'Depth of Investigation in Direct Current Methods'. *GEOPHYSICS* 36 (5): 943–59. doi:10.1190/1.1440226.

Schmidt, T., D. Mangold, and H. Müller-Steinhagen,. 2003. 'Seasonal Thermal Energy Storage in Germany'. In . Göteborg, Schweden. http://www.solites.de/download/literatur/03-03.pdf.

Schmidt, T., and H. Müller-Steinhagen,. 2004. 'The Central Solar Heating Plant with Aquifer Thermal Energy Store in Rostock- Results after Four Years of Operation'. In . Freiburg, Germany. http://www.solites.de/download/literatur/04-05.pdf.

Van Hoorde, Maurits, Thomas Hermans, Gaël Dumont, and Frédéric Nguyen. 2017. '3D Electrical Resistivity Tomography of Karstified Formations Using Cross-Line Measurements'. *Engineering Geology* 220 (March): 123–32. doi:10.1016/j.enggeo.2017.01.028.

Vanhoudt, D., J. Desmedt, J. Van Bael, N. Robeyn, and H. Hoes. 2011. 'An Aquifer Thermal Storage System in a Belgian Hospital: Long-Term Experimental Evaluation of Energy and Cost Savings'. *Energy and Buildings* 43 (12): 3657–65. doi:10.1016/j.enbuild.2011.09.040.

Wildemeersch, Samuel, Pierre Jamin, Philippe Orban, Thomas Hermans, Maria Klepikova, Frédéric Nguyen, Serge Brouyère, and Alain Dassargues. 2014. 'Coupling Heat and Chemical Tracer Experiments for Estimating Heat Transfer Parameters in Shallow Alluvial Aquifers'. *Journal of Contaminant Hydrology*, Selected papers from The 8th International Association of Hydrological Sciences (IAHS) Groundwater Quality Conference 2013 (GQ13) - Managing groundwater quality to support competing human and ecological needs, 169 (November): 90–99. doi:10.1016/j.jconhyd.2014.08.001.

Xu, J., R. Z. Wang, and Y. Li. 2014. 'A Review of Available Technologies for Seasonal Thermal Energy Storage'. *Solar Energy* 103 (May): 610–38. doi:10.1016/j.solener.2013.06.006.

7 Annex

7.1 CTD monitoring annexes

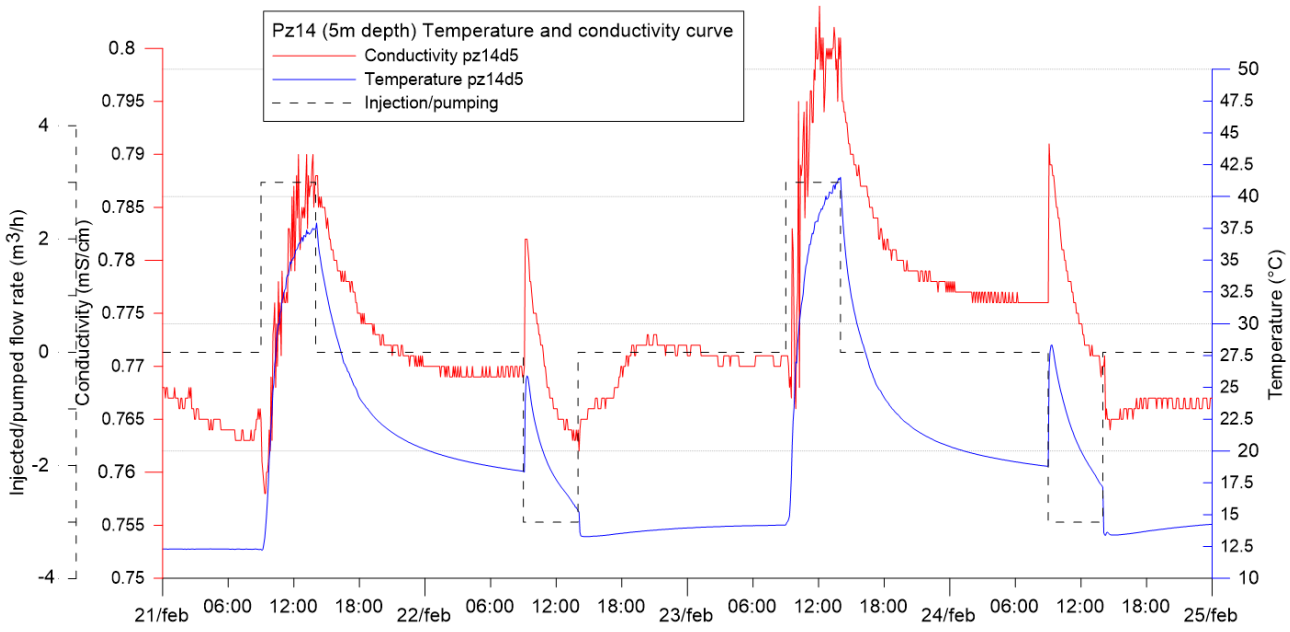

Figure A 1. Temperature and conductivity curves of Pz14 (5m depth).

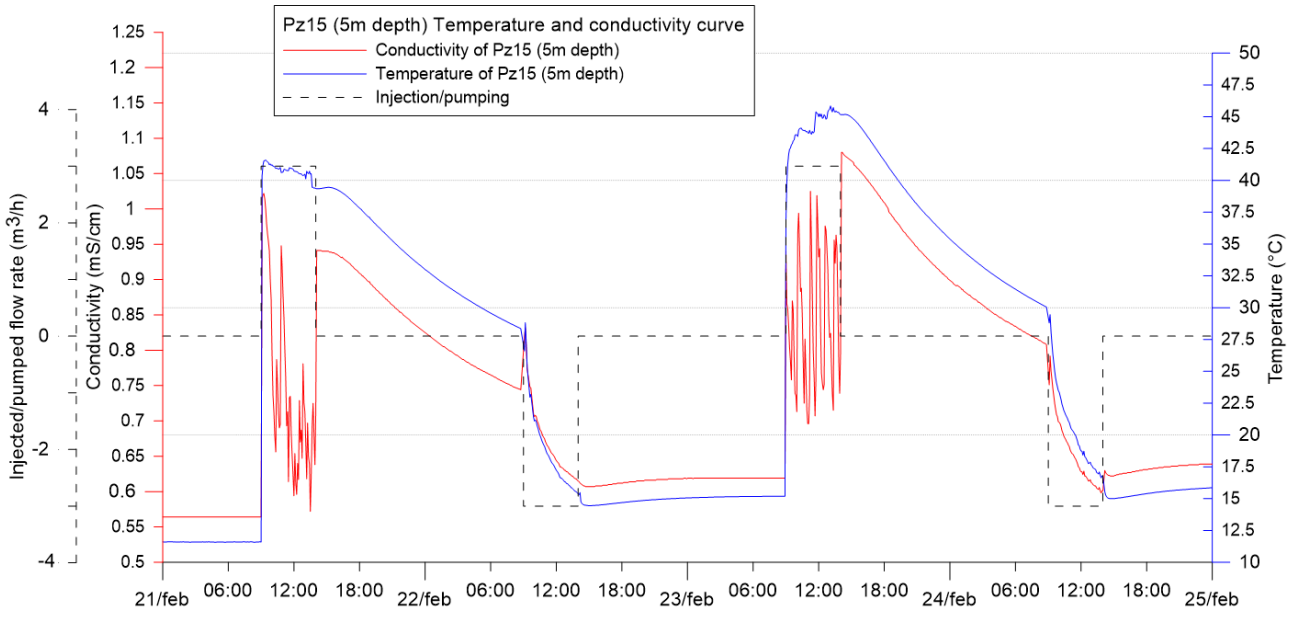

Figure A 2. Temperature and conductivity curves of Pz15 (5m depth)

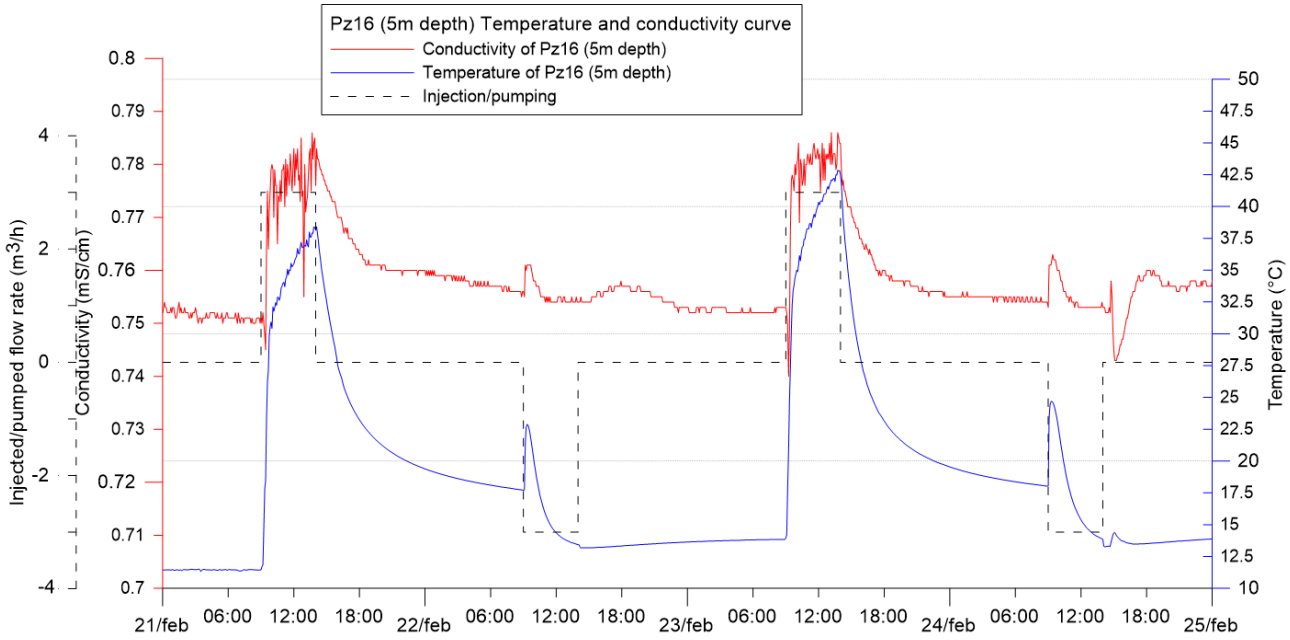

Figure A 3. Temperature and conductivity curves of Pz16 (5m depth)

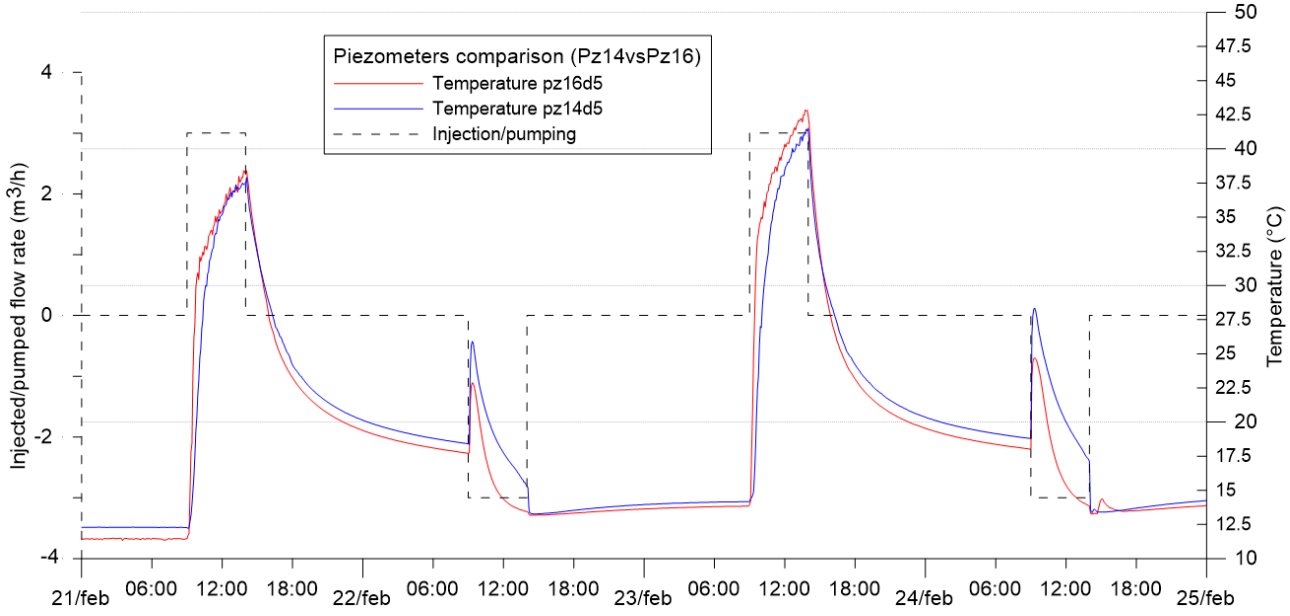

Figure A 4. Comparison of Pz14 and Pz16 temperature curves (5m depth)

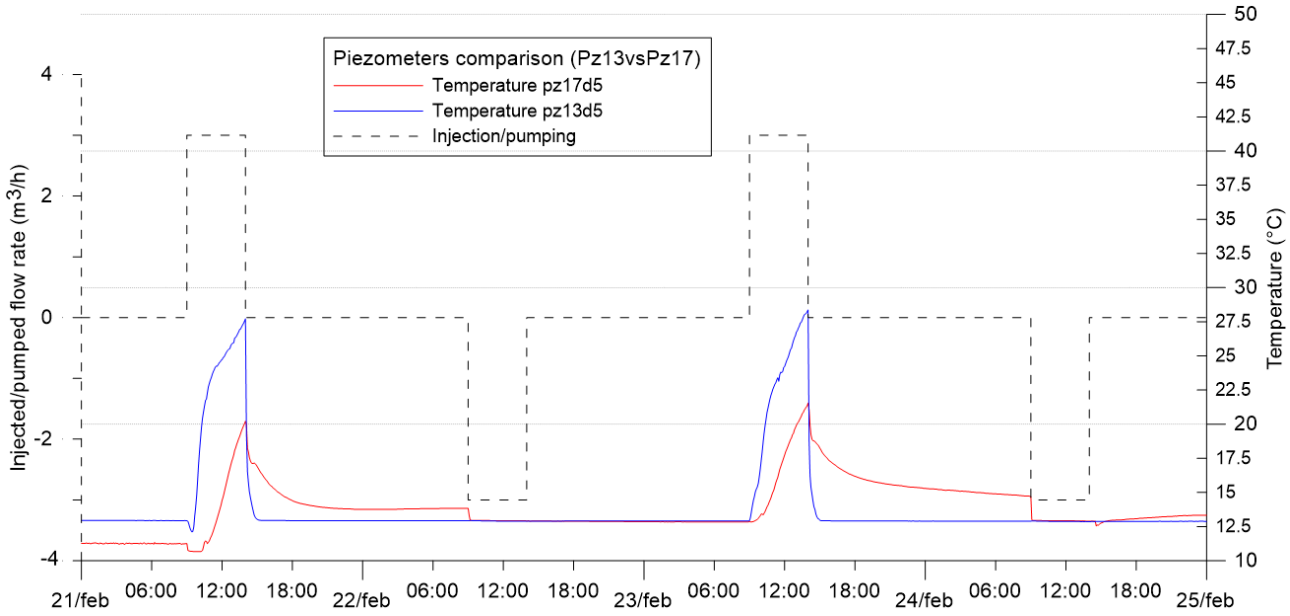

Figure A 5. Comparison of Pz13 and Pz17 temperature curves (5m depth)

7.2 2D resistivity models annexes

	Background		Injection 1		Pumping 1		Injection 2		Pumping 2	
	Iteration	RMS (%)	Iteration	RMS (%)	Iteration	RMS (%)	Iteration	RMS (%)	Iteration	RMS (%)
Profile 1	2	2.9	2	2.9	2	3.0	2	3.0	2	2.8
Profile 2	3	2.1	2	2.4	2	2.5	2	2.4	2	2.3
Profile 3	2	3.3	2	3.6	4	3.1	2	3.5	2	3.0
Profile 4	2	3.2	4	2.4	3	2.8	3	2.8	3	2.9
Profile 5	3	2.6	4	2.3	2	3.3	3	2.6	2	3.3
Profile 6	3	2.5	3	2.5	3	2.5	3	2.4	3	2.4

Table A 1. Iteration and RMS errors of 2D time-lapse resistivity models.

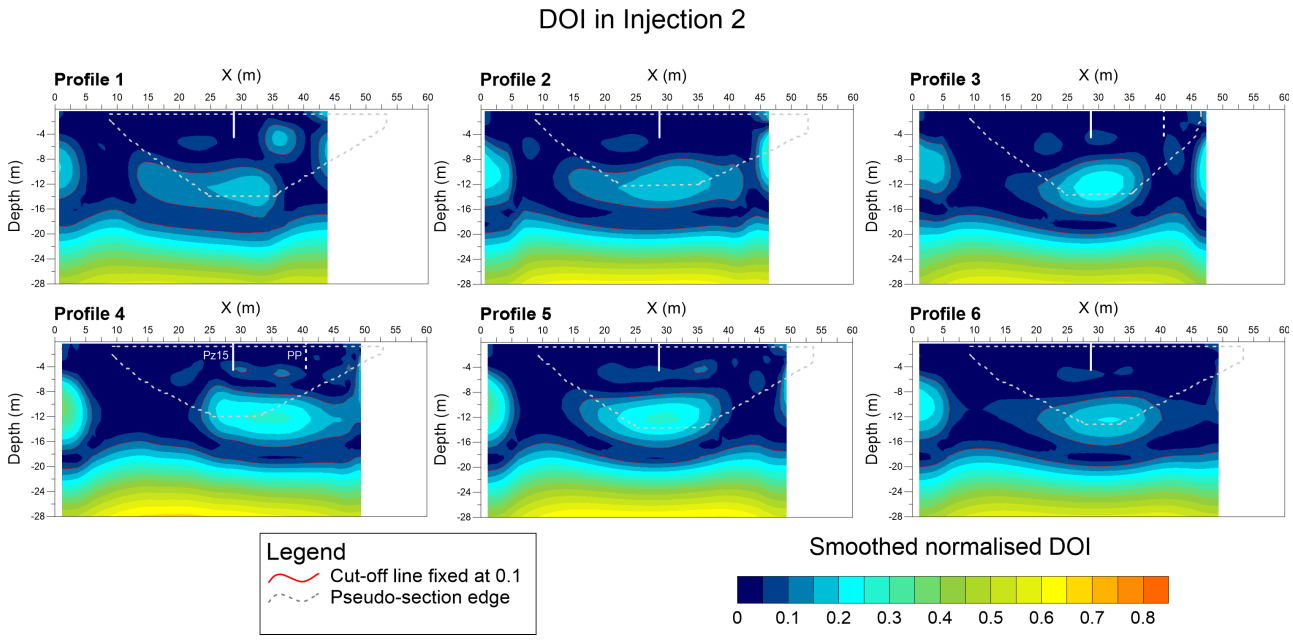

Figure A 6. DOI index distribution in Injection 2 models.

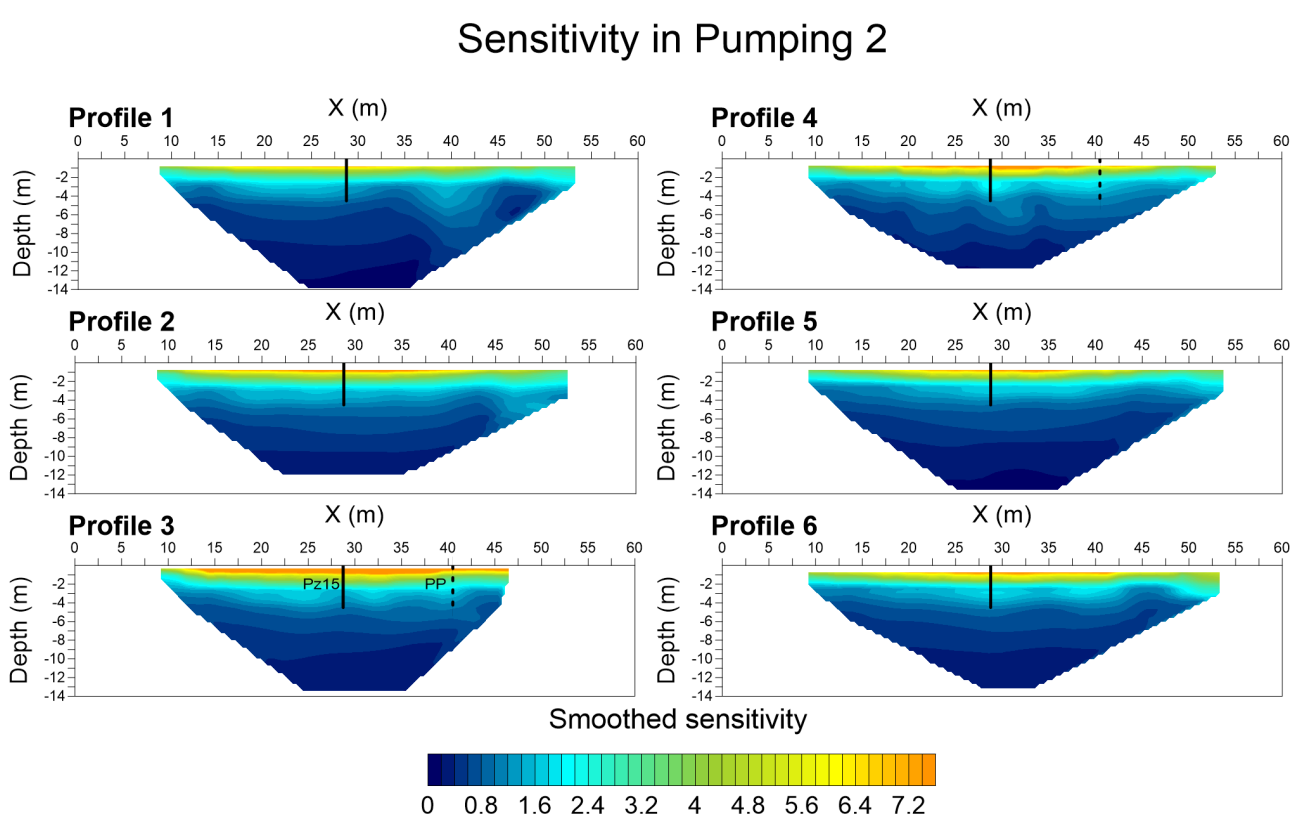

Figure A 7. Sensitivity distribution in Pumping 2 models.

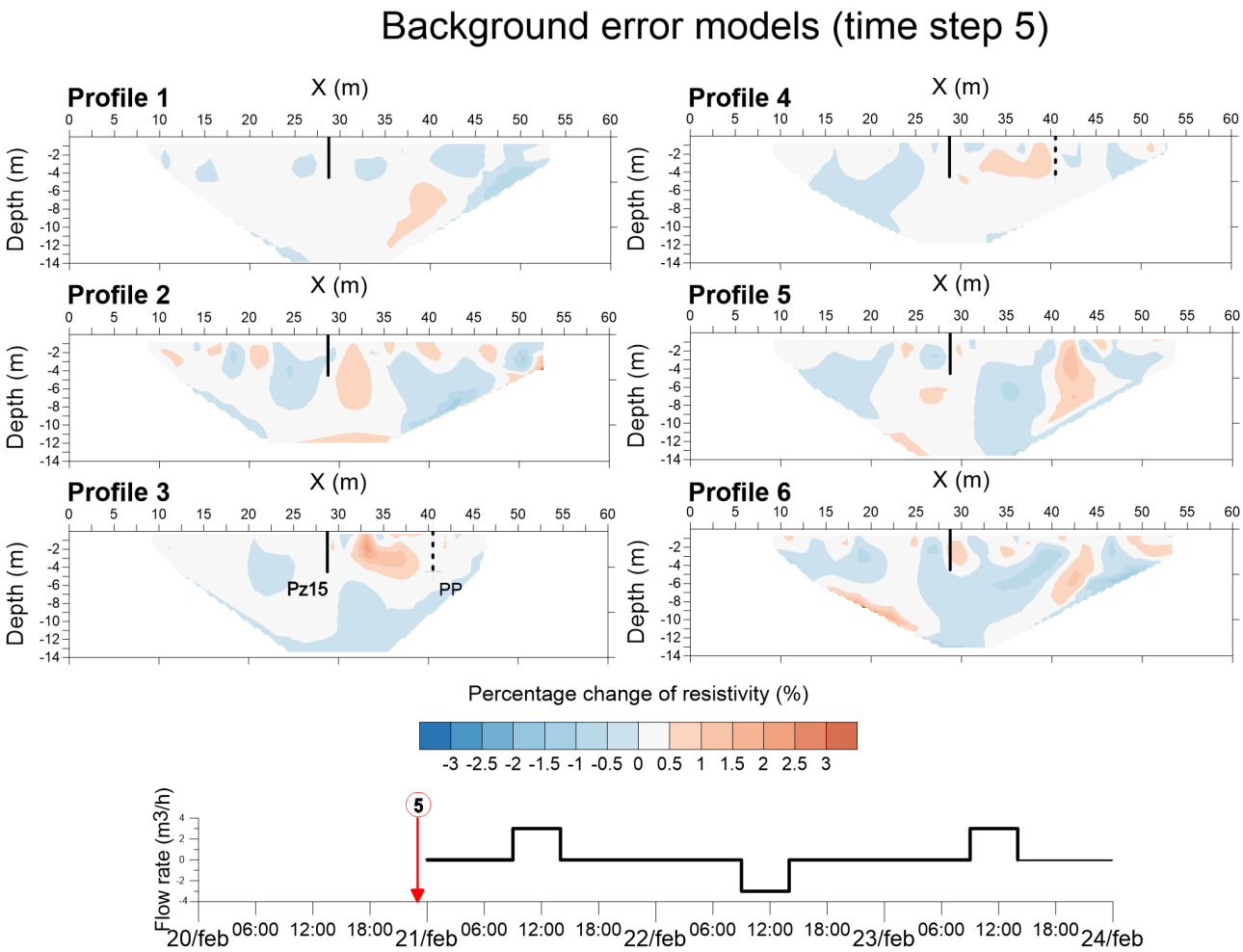

Figure A 8. Background error models.

7.3 Temperature conversion annexes

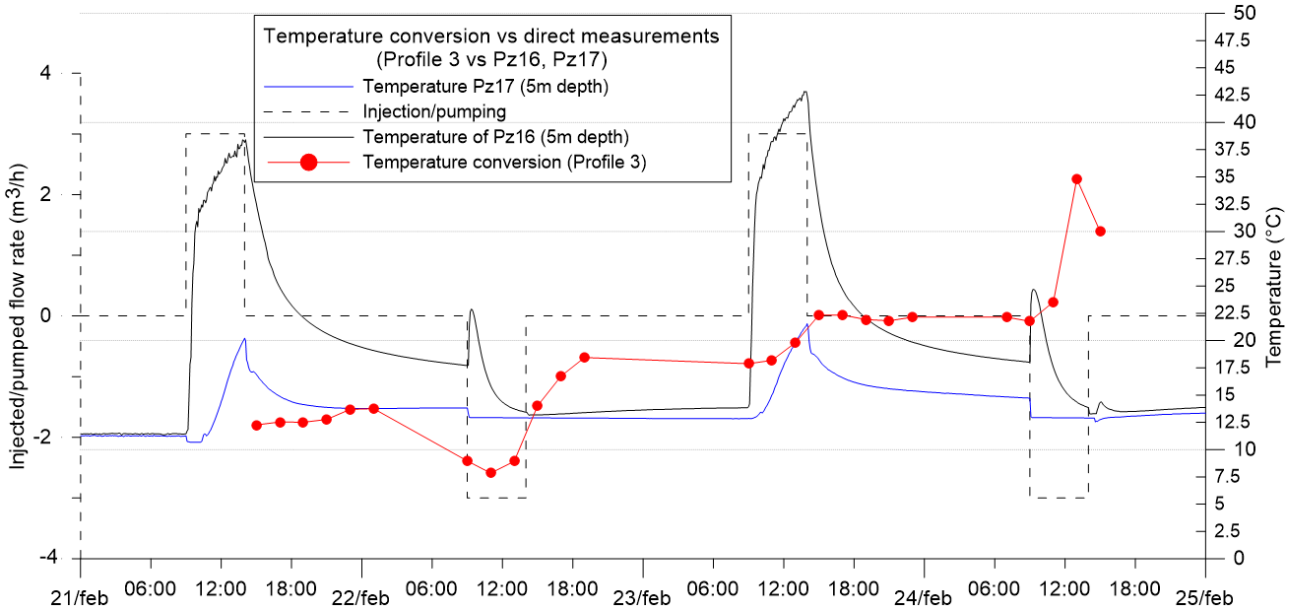

Figure A 9. Comparison between direct measured temperature values and derived temperature values from ERT results (Profile 3 vs Pz16, Pz17).

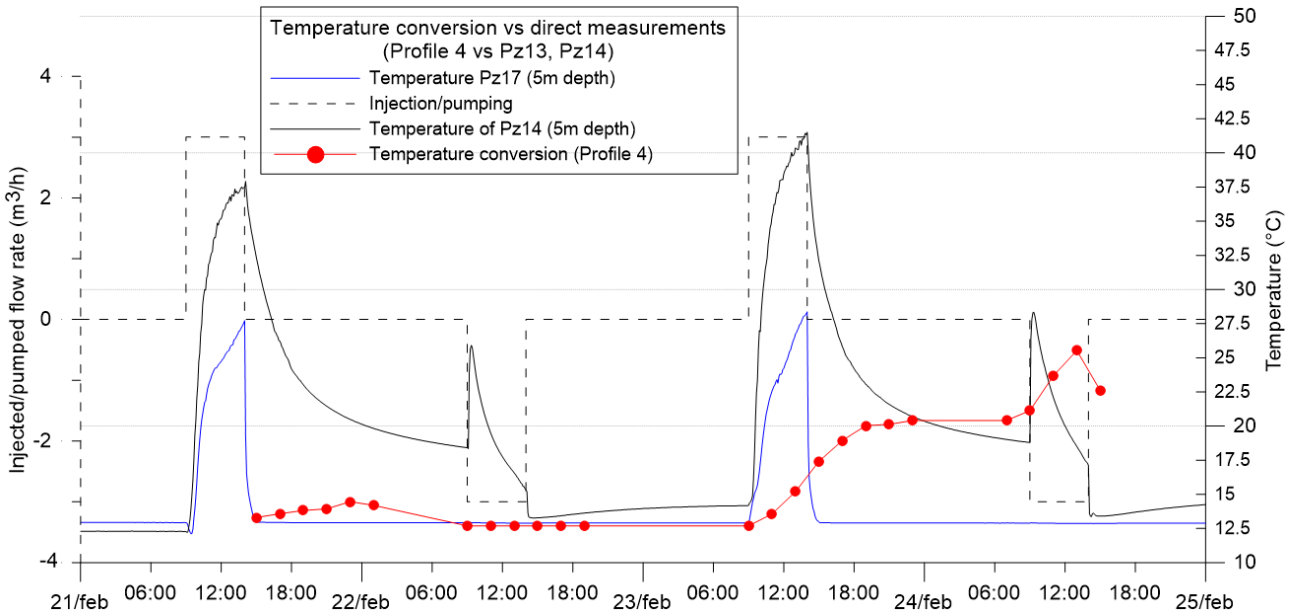

Figure A 10. Comparison between direct measured temperature values and derived temperature values from ERT results (Profile 4 vs Pz13, Pz14)

7.4 3D resistivity models annexes

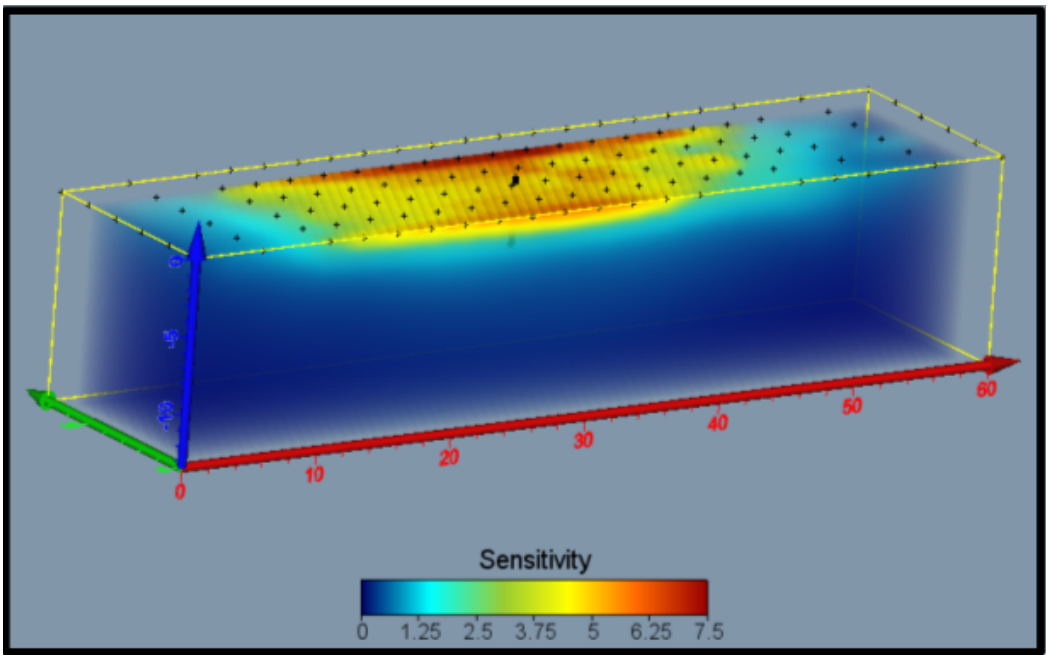

Figure A 11. 3D sensitivity model of Injection 1.

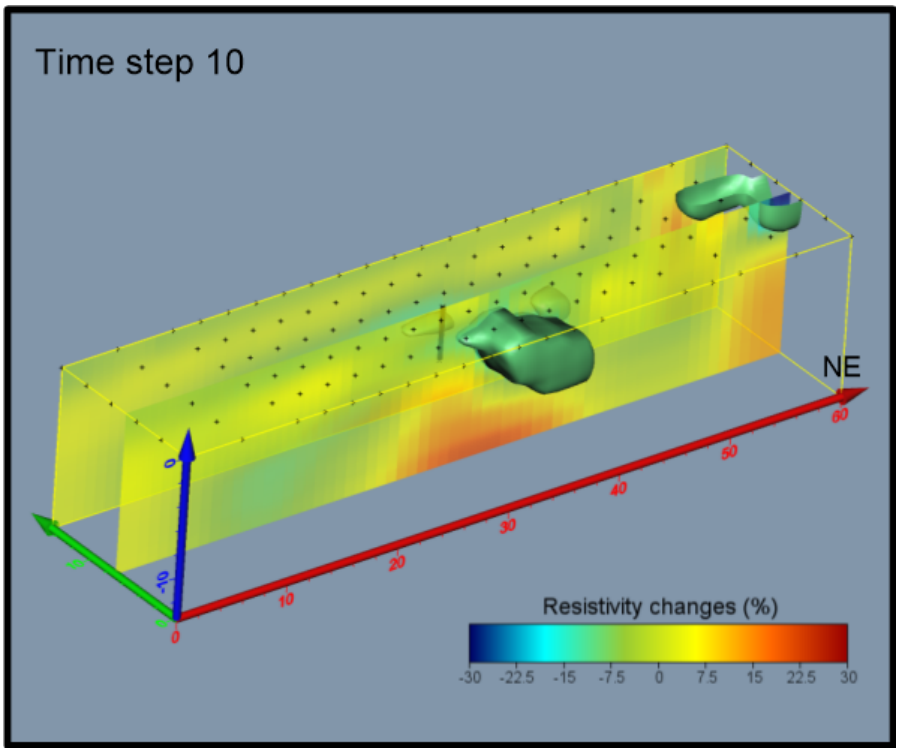

Figure A 12. Computation of volume by means of Isosurface function.